RICE UNIVERSITY

Surface Enhanced Vibrational Spectroscopy and Electrical Characterization on Nanojunctions

by

Yajing Li

A THESIS SUBMITTED
IN PARTIAL FULFILLMENT OF THE
REQUIREMENTS FOR THE DEGREE

Doctor of Philosophy

APPROVED, THESIS COMMITTEE

Douglas Natelson, Chair
Professor of Physics and Astronomy at
Rice University

Peter Nordlander
Wiess Chair, Professor of Physics and
Astronomy & Electrical and Computer
Engineering,

Christy Landes
Professor of Chemistry & Electrical and
Computer Engineering

HOUSTON, TEXAS
June 2016

ABSTRACT

Surface Enhanced Vibrational Spectroscopy and Electrical Characterization on Nanojunctions

by

[Yajing Li]

Molecular junctions are excellent systems for studying electronic and vibrational properties at the single molecule level. Molecular junctions bring together a wide variety of disciplines including quantum physics, nanofabrication and chemistry. Applications include single electron transistors and other novel electronic components.

Each molecule possesses its own unique vibrational and electronic energy levels. These unique quantum states provide a fingerprint for identifying the molecule. Furthermore, the quantum states of a molecule can be coupled to nearby photons, atoms, molecules, surfaces and bulk materials yielding a new set of modified energy levels. Studying these highly sensitive and complex interactions requires advanced experimental techniques such as fabricating nanojunctions with sub 10 nm gap sizes.

Small gap sizes are not alone enough to guarantee insight into molecular properties. The junctions must be able to magnify and focus photons of hundreds of nanometers in wavelength down into sub 10 nm scales. The corresponding enhancement of the local electromagnetic field is the essential ingredient to probing molecular quantum states. The best way to provide such strong enhancement of electromagnetic fields into sub wavelength regimes is through plasmonics.

This thesis discusses the fabrication of plasmonic molecular junctions. These molecular junctions will be shown to demonstrate large electromagnetic fields sufficient for Surface Enhanced Raman Spectroscopy (SERS). These molecular junctions are also used to study simultaneous electronic transport through the molecule. This concurrent study of transport and optical vibrational spectroscopy opens an unprecedented realm into the study of quantum interactions of molecules, electrons, phonons and photons.

Specific molecules which will be studied include C_{60}, PCBM and BPE. We demonstrate large, reversible, voltage-driven shifts of vibrational mode energies of C_{60} and PCBM molecules in gold junctions. C_{60} mode energies are found to vary approximately quadratically with bias, but in a manner inconsistent with a simple vibrational Stark effect. PCBM mode energies showed a combination of linear and quadratic shifts in vibrational energies with voltage.

In addition to facilitating SERS, metallic nanogap junctions also demonstrate the ability to enable Surface Enhance Infrared Absorption (SEIRA) spectroscopy. We demonstrated our nanogap stuctures have the sufficient high field enhancement of detecting the local dielectric composition of nm thick. This can open up opportunities of investigation of heat generation in metallic nanostructures and the surrounding dielectric environment.

Throughout this thesis, experimental work will be shown to be in outstanding agreement with theoretical studies based on density functional theory(DFT) and finite difference time domain (FDTD) method.

Acknowledgments

The research presented in this dissertation over the past six years would not be possible without the help and support of many people. First, I'd like to thank my doctoral advisor, Dr. Douglas Natelson. Doug is a very enthusiastic physicist. He can deliver scientific concepts and knowledge in a very vivid way. He writes a very popular and entertaining blog called 'nanoscale views'. As a PhD advisor, Doug always makes time for his students and cares deeply about our success. I have benefited a lot from our numerous discussions on all kinds of topics. He makes me a better speaker and writer. I feel blessed to conduct my thesis research under his guidance. So, thank you, Doug.

Second, I want to thank my parents. They've been supportive of me throughout my life. They always believe I have the ability to overcome any obstacle I confront. I feel their pride and happiness when I tell them about my publications, awards or conference presentations. In their eyes, I'm always the child they want to give everything to. This wouldn't be possible without you, my parents, thank you.

Next, I'd like to thank all of the Natelson group members, past and present. Professor Jiang Wei who was a postdoc when I joined the group, has always been patient with my entry level questions and helped me develop the necessary experimental skills. Dr. Dan Ward, during our short time together, did his best to transfer his knowledge to me and continued to respond to my questions even after he moved to Wisconsin. Dr. Joey Herzog and Dr. Kenny Evans have been an absolute pleasure to work with in the optics sub-group.

Dr. Pavlo Zolotavin, who is very sharp and knowledgeable, made a major contribution to the upgrade of the laser system. He provided a lot of valuable suggestions and perspectives for my research. The rest of the group members, Dr. Ruoyu Chen, Dr. Heng Ji, Panpan, Xifan, Loah, Mathieu and Charlotte, thank you for being excellent coworkers and friends.

I'd also like to thank Prof. Halas and her students Liangliang and Ben for their generosity of sharing their FTIR microscope for my SEIRA research.

Finally, I'd like to thank my boyfriend, Vik. Rice graduate school in physics brought us together. He made the past 6 years at Rice University full of sweet memories. He's supportive of my decision to move forward to my post-doc research even that means long distance relationship for a while. There is more than just saying thank you, Vik. You're always my best friend and the best part of my life.

Contents

List of Figures

List of Equations

Nomenclature

AC	Alternating current
AFM	Atomic Force Microscope
BPE	trans-1,2-bis-(4-pyridyl) ethylene
CL	Cathodoluminescence
DAC	Digital-to-analog converter
DC	Direct current
DFT	Density functional theory
FDTD	Finite Difference Time Domain
FTIR	Fourier transform infrared spectroscopy
HOMO	Highest occupied molecular orbital
IETS	Inelastic electron tunneling spectroscopy

LSPR	Localized Surface Plasmon Resonance
LUMO	Lowest unoccupied molecular orbital
MBA	Mercaptobenzoic acid
MCT	Mercury cadmium telluride
PCBM	Phenyl-C61-butyric acid methyl ester
SEIRA	Surface enhanced Infrared absorption
SERS	Surface enhanced Raman spectroscopy
SEM	Scanning electron microscope
SPP	Surface Plasmon Polariton
STM	Scanning Tunneling Microscope

Chapter 1

Introduction

1.1 [Preface]

This thesis will cover the surface enhanced Raman (SERS) and surface enhanced Infrared absorption (SEIRA) spectroscopy combined with electrical characterization performed using metal nanogap junctions. Molecular junctions in the past have been great systems to study the conduction mechanism at the single molecule level[1,2]. Nanogap structures with nanometer interelectrode spacing have been proven to be excellent SERS substrates[3]. The combination of the optical and electrical measurement opens opportunities of probing the vibrational and electronic properties of a single molecule at the metal interface.

The feasibility of conducting both SERS and transport measurements on the molecular junction has been demonstrated in previous work in the Natelson research group[4,5]. The primary topics of this thesis are divided into two parts: 1.) To investigate how the mechanical (vibrational) properties of single molecules evolve in various electrostatic environments. 2.) To develop nanogap structures into SEIRA substrates and enhance our knowledge of the plasmonic properties of the nanogap structures in the infrared regime.

This thesis consists of six chapters. Chapter One gives an overview of the necessary background knowledge to understand the physics underlying the experimental results in the following chapters. Chapter Two introduces the fabrication techniques of the nanogap structure, explains the measurement schemes, and shows several fundamental properties of the nanogap structures. Chapter Three reports vibrational mode softening in C_{60} molecules that scales quadratically in the external DC bias, V, applied across a junction. Chapter Four discusses the Stark shift of vibrational modes in the C_{60} derivative PCBM with applied DC bias. Finally, Chapter Five focuses on using nanogap structures as SEIRA substrates and as probes of the local dielectric environment. Chapter six summarizes the previous chapters and discusses the perspectives on future research directions.

1.2 Vibrational spectroscopy

1.2.1. Raman spectroscopy

Raman spectroscopy is a very useful method to provide information about a molecule's composition, vibrations and rotations . It was discovered by C. V. Raman and K. S. Krishnan in liquids in 1928[6] and independently by Grigory Landsberg and Leonid Mandelstam in crystals[7]. An example Raman spectra of a film of C_{60} on a suprasil substrate[8] is shown in Figure 1-1. The Raman spectroscopy measures the energy difference between an incident photon and the photon scattered off the molecules of interests. The majority of the light scattering collisions are elastic (Raleigh scattering), resulting in no difference between the energy of the incident photon and scattered photon. Only a small portion of the incident photons go through the inelastic process, in which the incident photon exchanges some amount of energy with the molecules. The transferred energy is reflected in the energy difference between the incident photon and the scattered photon, and is typically equal to a vibrational energy splitting of the molecule.

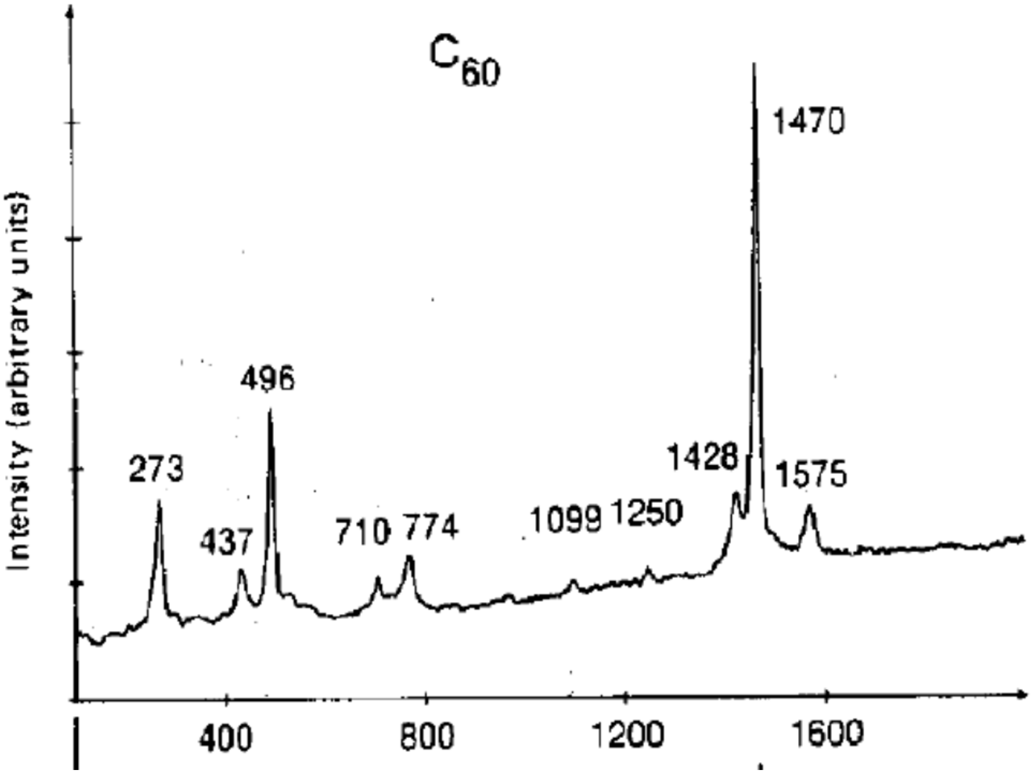

Figure 1-1 Raman spectrum of C_{60} on suprasil substrate, reprinted from reference [8]. X axis represents wavenumbers in cm^{-1}.

Non-resonant Raman scattering occurs when an incident photon excites an electron in the molecule from the ground state to a virtual excited state. The electron then relaxes back to the ground state but the molecule returns to a different vibrational state. The difference between the initial and final vibrational states of the molecule reflects which process happened, Raleigh or Raman. As shown in Figure 1-2, if there is no difference between the initial and final vibrational state, the scattered photon has the same energy as the incident photon; this is Raleigh scattering, the green line shown in Figure 1-2. If the molecule undergoes the Raman process and returns to a final vibrational state different from the initial state, an energy difference between the incident and scattered photon is expected. Raman scattering can be further classified into Stokes scattering and anti-Stokes scattering. In Stokes scattering, the incident photon loses energy to the molecule to create a local vibrational mode or phonon, resulting in the scattered photon having less energy than the incident one. The converse is true when the molecule undergo anti-Stokes scattering, such that the scattered photon has acquired energy from an already populated vibrational mode.

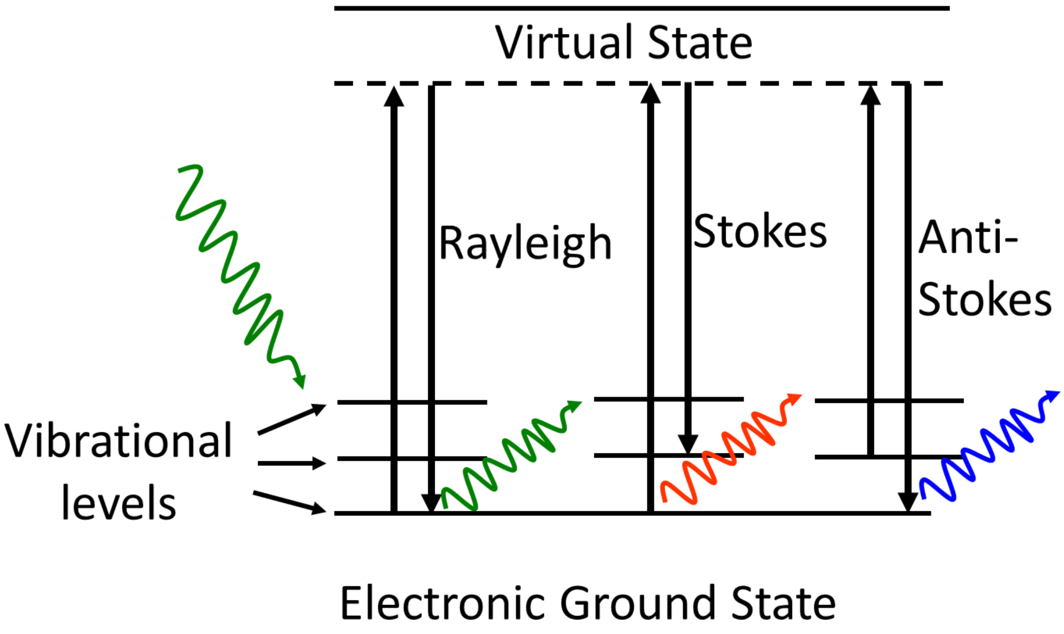

Figure 1-2 Rayleigh versus Raman scattering process.

The mathematical origin of Raman scattering can be expressed as follows. The incident electric field ***E*** induces an electric dipole moment in the molecule.

Equation 1-1

$$\boldsymbol{\mu}(\omega_{in}t) = \boldsymbol{\alpha}(\omega_{vib}t) \cdot \boldsymbol{E}(\omega_{in}t).$$

Here $\boldsymbol{\alpha}(\omega_{vib})$ is the polarizability tensor, representing how an external electric field along some direction polarizes the molecule and produces an electric dipole moment, which may be oriented in a different direction than ***E***. For Raman scattering to a particular mode to occur, the polarizability tensor depends on atomic positions, and those positions have to vary with time for the particular mode. Raman spectroscopy is a linear spectroscopy, and the scattered intensity scales linearly with the incident radiation intensity.

1.2.2. Infrared absorption spectroscopy

Infrared absorption spectroscopy is an analytical method of measuring the interaction of the infrared light and the chemical species of interest. It can be used to determine the functional groups of the molecules by measuring the vibrational frequencies of the molecules.[9,10]

Instead of creating (virtual) electronic transitions like in the Raman scattering process, infrared light excites the vibrations or rotations of the molecule directly through the interaction of the electric field and the arrangement of charge in the molecule. In the presence of the infrared light, the molecules absorb energy from the incident photons, resulting in an increased amplitude of vibrations or rotations. The absorbed energy in the spectrum characterizes the molecular structure.

Infrared absorption couples to the time-varying dipole moment of the molecule caused by re-arranging the electronic distribution due to atomic motion in the molecules during the light matter interaction[11]. When the frequency of the incoming infrared beam coincides with that of the molecule's vibrational modes or a collection of the modes, absorption takes place. By scanning the wavelength range in the monochromator and measuring the transmitted or reflected light, how much energy is absorbed by the molecule at each frequency can be determined.

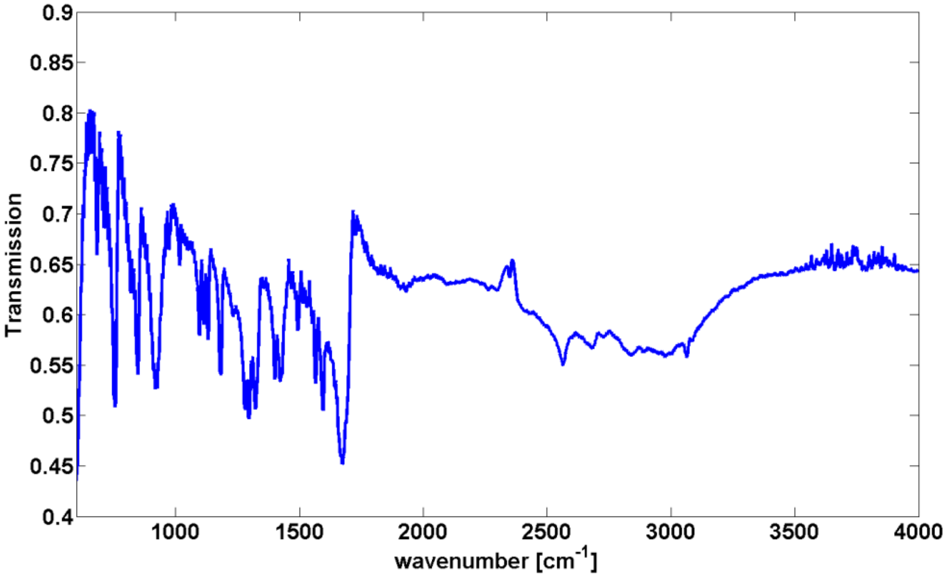

Figure 1-3 IR spectrum of bulk Mercaptobenzoic Acid(MBA) on intrinsic silicon substrate at room temperature using FTIR in transmission mode.

1.3 Plasmonics

Plasmons are the collective oscillations of free electrons with respect to the positive background charge in a noble metal. These oscillations can be excited in the presence of a time-varying external electromagnetic field. This external force is typically supplied by photons or by impinging electrons. The response of the plasma oscillations resembles that of a damped driven harmonic oscillator. The external field supplies the driving force while the restoring force is provided by the Coulomb potential of the induced surface charges.

Damping can result from both the emission of radiation and the scattering of carriers by disorder and phonons[12–14]. In the damped driven harmonic oscillator model, the absorbed power of the system reaches a maximum at a specific frequency known as the resonance frequency. For plasmons, these resonance frequencies cause strong induced electromagnetic fields at the surface of the metallic system. Thus the utility of plasmons lies in their ability to magnify and focus incoming electromagnetic energy into small volumes. The resonance frequency of a plasmonic system is strongly dependent on size[15–17], shape[17–19], chemical composition[20,21] and embedding dielectric environment[22,23]. However, for a noble metal of macroscopic size, the bulk plasmon frequency is defined as follows[24]:

Equation 1-2

$$\boldsymbol{\omega_b = \sqrt{\frac{ne^2}{m\varepsilon_0}}}$$

where *n*, *e*, and *m* represent the density, charge, and effective mass of the free electrons. ε_0 is the background dielectric constant of the material. Bulk plasmon frequencies for various metals are well documented and typically lie in the ultraviolet regime of the electromagnetic spectrum. However, additional plasmon resonances, known as surface plasmons, are also observed. Surface plasmons come in two categories: localized surface plasmon resonances (LSPR) and surface plasmon polaritons (SPP). SPP propagate in the plane of the metal surface and decay evanescently in the direction perpendicular to the surface, thus localizing the electric field to the interface between the metal and surrounding dielectric layer. The concept of skin depth is defined as the decay length of the electromagnetic field within the conductor for a plane wave incident on a half-space of a conducting medium. The skin depth is on the same order as the penetration of the field into metallic structures supporting plasmon oscillations, though the true field confinement can be affected by metal geometry and plasmon response. The decay length is very sensitive to inhomogeneities on the surface and thus SPP are an excellent way to probe surface properties of materials. Figure 1-4 illustrates a SPP.

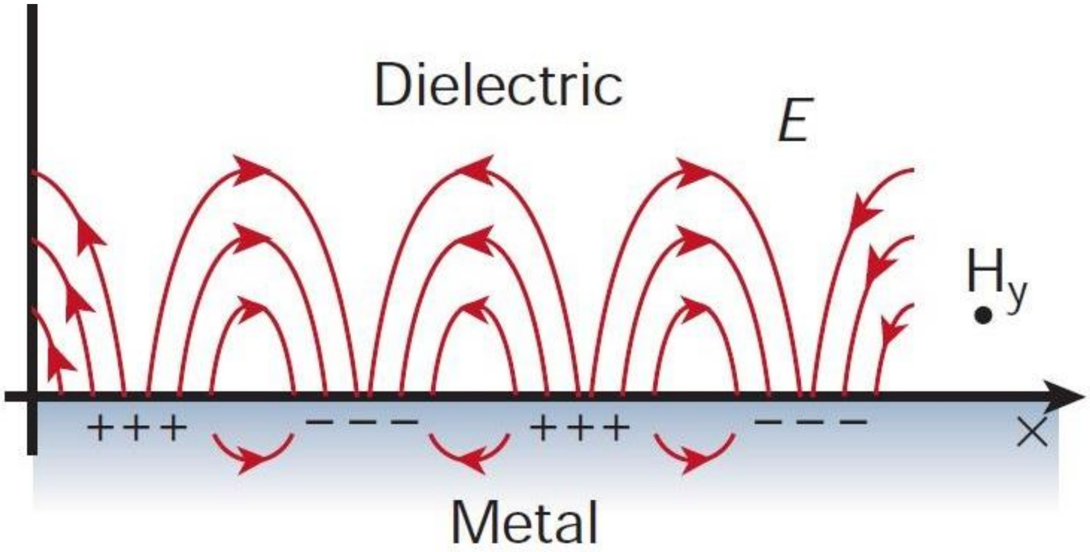

Figure 1-4 Illustration of a surface plasmon polariton (SPP) reprinted from reference [25]. Free electrons oscillate at the surface of the metal, leaving areas of positive charge in their absence. These moving charges create electromagnetic fields in the vicinity of the surface.

SPP have well defined momentum and dispersion relations. However, propagation lengths for SPP are quite poor (typically on the scale of micrometers). This is due to losses in the metal. As the SPP propagates, the oscillating electrons and holes that make up the SPP can scatter off disorder and through phonon scattering, losing their spatial and temporal coherence, and dissipating heat in the phonons of the metal.. The electron-hole pairs eventually lose energy to phonon scattering. The end result is that heat is generated in the metal and the SPP decays as it propagates.

LSPR exist in confined in nanoscale systems such as nanospheres, nanorods and other subwavelength metallic systems. LSPR do not propagate in space – as standing waves, they have zero net momentum, and structures that support LSPR can be thought of as nanoscale antennas. These LSPR resonances can be dipolar or multipolar in nature, and like all confined wave modes occur at discrete frequencies. The basic principle of a dipolar LSPR is depicted in Figure 1-5.

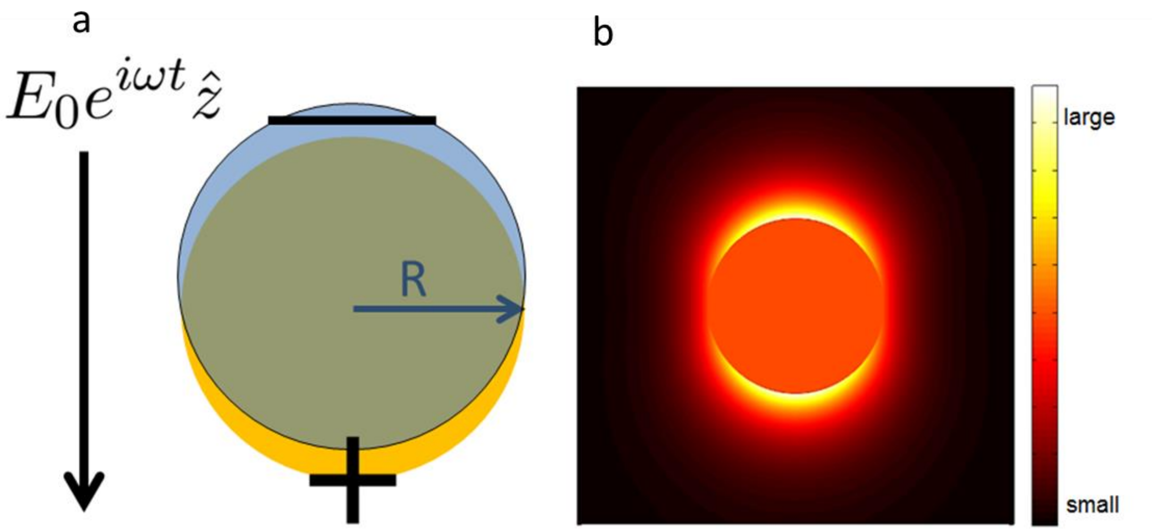

Figure 1-5 a) Illustration of a localized surface plasmon resonance (LSPR). An oscillating electric field displaces the electron cloud (blue) with respect to the positive background ions of a metallic nanoparticle. b) Spatial distribution of the induced electric field around the nanoparticle.

An incoming oscillating electromagnetic field polarized in a given direction will displace the free electron cloud with respect to the immobile positive background ions. Since the field oscillates, the electron cloud oscillates along the axis of the polarization.

These plasmons are short lived quasi-particles, typically decaying in a matter of femtoseconds. However, as long as the driving force persists, the oscillation continues indefinitely. The oscillating cloud of electrons creates surface charges. These surface charges create induced local electric fields, as depicted in Figure 1-5b. Note the dipolar nature of the induced fields. In particular, the fields are strongest near the surface of the nanoparticle and can yield electric fields 10x stronger than E_0.

As mentioned before, SPP and LSPR are strongly sensitive to the shape of the object, the chemical composition, the proximity to other plasmonic systems, and the embedded dielectric environment. According to classical Mie theory, For example, the dipolar LSPR of a plasmonic nanosphere (in vacuum)[26] occurs at ${}^{\omega_b}/_{\sqrt{3}}$. However, if the nanosphere has a background dielectric, ε_j, (due to the polarization of the background ionic charge), or is embedded in a material of background dielectric ε_m, then the dipolar LSPR resonance frequency will shift to longer wavelength (lower energy). Additionally, as the nanoparticle grows larger and becomes comparable to the wavelength of the external light the resonance frequency again redshifts. Also if the nanosphere is brought to within a few radii of another nanosphere, the resulting dipolar LSPR is shifted to lower energy due to a hybridization effect, as one must consider the collective plasmon response of the coupled system. Such a system is called a dimer. A conceptual mapping of the surface charges around a dimer is shown in Figure 1-6.

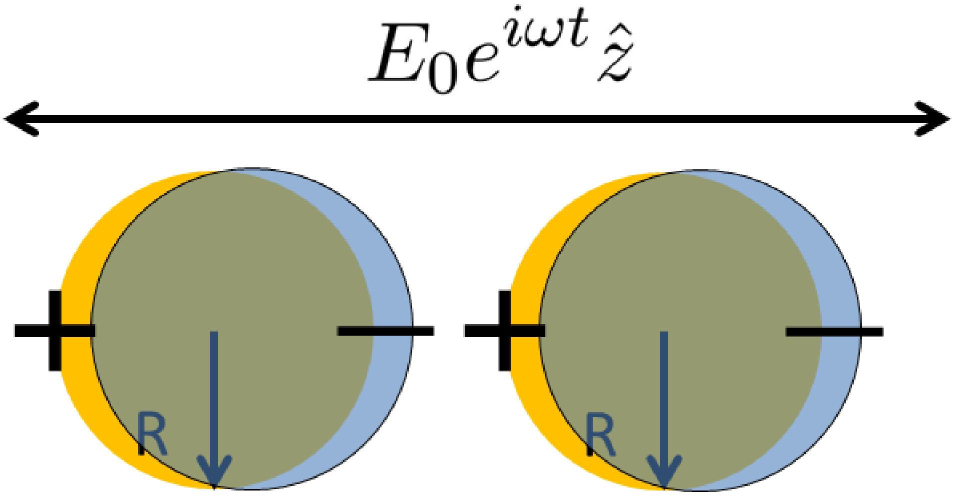

Figure 1-6 Surface charges in a plasmonic dimer. As the external field oscillates, so do the electronic clouds on each nanoparticle. Due to the attractive Coulomb interaction between nanoparticles, the resulting dipolar resonance frequency decreases.

Figure 1-6 shows that two nanoparticles brought to within close proximity will strongly interact through the Coulomb force. The resulting oscillations of the plasmons on each nanoparticle will be in phase resulting in a 'bonding dipolar plasmon'. The surface charges residing in the gap between the nanoparticles are of opposite sign, thus creating a strong induced electric field in the gap. Junctions between plasmonic systems can yield local electric fields of ~ 100E_0 when properly excited. Note that this enhancement effect only occurs at or near the resonance frequency of the bonding dipolar plasmon. The actual field strength will depend strongly on the distance between the metals and the curvature of the metals. Later in this thesis, a gold bow tie junction is utilized to create strong electromagnetic fields in the gap. Molecules are then placed in this gap and exhibit novel vibrational and electronic resonances of their own.

1.4 Single molecule SERS

One of the main applications of plasmonics is to facilitate vibrational spectroscopy and possibly create single molecule sensors. The locally enhanced electric field at the plasmonic surface increases the signal of optical spectroscopies, a phenomenon known as “surface enhancement”. The first observation of a surface-enhanced Raman scattering (SERS) signal was obtained from pyridine adsorbed on a silver electrode in 1974[27]. However the origin of the enhanced Raman signal was not identified until 1977 by Jeanmaire *et al*.[28] Earlier studies focused on the absorbance on rough metal surfaces. The enhancement of the Raman signal can reach 10^5 to 10^6.

In general, two mechanisms are believed to contribute to the surface enhancement: electromagnetic and chemical enhancement. The electromagnetic enhancement is attributed to the plasmon resonance and determined by the metal dielectric function and the geometry of the substrate.

A simple derivation of the electromagnetic enhancement is shown as follows:

Let $E_0(\omega)$ denote the electric field of the incident radiation where ω is the frequency of the incident light. The total incident field at the metal surface E_s is related to the incident field by: $E_s = g E_0$, where g is the enhancement factor and depends through the plasmon response of the structure on the incident frequency ω. The Raman radiated electric field E_r is enhanced in a similar way, $E_r = g' E_s$, where g depends on the radiated light frequency. This can be thought of as either a classical antenna effect, or as a local (plasmonic) enhancement of the photon density of states at the emitted frequency The SERS emission scales as $|E(\omega)|^2|E(\omega')|^2$, where E is the local electric field of the light, ω is the incident frequency, and ω' is the Raman-scattered frequency. In general, the plasmon resonances responsible for field enhancement can be quite broad, so that $g' \sim g$, $E_r \approx g^2 E_0$. Raman shifts can be large, though, so this is not always true. The Raman intensity is proportional to $|E|^2$, so the plasmonic contribution to the SERS intensity is proportional to $|g|^4$. The plasmons enhance the native Raman signals by increasing the local field in the vicinity of the molecules and by enhancing the coupling of Raman-scattered photons to the far field.

The chemical enhancement is the general term used to describe additional enhancement of Raman scattering due to binding between the molecule and the metal surface; it is difficult to quantify and is sample dependent. The chemical enhancement is generally believed to arise from the chemisorption from the adsorbate on the metal surfaces, which results in molecule-metal charge-transfer[29–31]. The chemical enhancement occurs when the molecule sits on the metal surface and its electronic band overlaps with the Fermi surface of the metal surfaces. This wave function mixing between the molecule and the metal surface allows the electron from the metal surface to occupy the LUMO of the molecule. For a given excitation frequency, this can move the molecule closer to resonant Raman scattering than the molecule-in-vacuum situation, providing a much larger cross section of the molecules. The chemical enhancement contributes to the SERS intensity by a factor of 10 to 100 [31]. It's important to note that the chemical enhancement can affect the polarizability tensor and the vibrational modes of the molecule, leading to SERS modes that would differ from the vibrational modes in the bulk enhancement can affect the polarizability and the vibrational modes from SERS would differ from the vibrational modes in the bulk.

The plasmonic enhancement empowers the SERS with the capability of progressing from the bulk to sensitivities at the single molecule level.[32,33] Compared with single molecule fluorescence, single molecule SERS has the advantages of decreased sample bleaching[34] and rich vibrational fingerprints. The first reported single molecule SERS observations were made of random aggregates on colloidal silver nanoparticles[32,33].

Determining rigorously that SERS spectra are originating from single molecules is difficult. The isotopologue approach is one approach that has been used to confirm the evidence of single molecule nature[35–37]. It is possible to distinguish two molecules with different isotopic vibrational energies even when measured at low concentration. Another way to identify single molecules is to study the line width of the vibrational modes from the SERS spectrum. [38]

When the number of molecules under observations becomes small, two characteristic features are frequently observed: *Blinking* and *spectral diffusion*. These phenomena are believed to be the evidence of a small ensemble of molecules.

“Blinking” appears as sudden changes of different vibrational mode intensities in the Raman spectrum as a function of time. The term “blinking” originates from random switching between ON (bright) and OFF (dark) fluorescent states of quantum dots under continuous optical excitation. This phenomena was partially understood to related with attributed to Auger ionization[39,40]. In the case of Raman, the intensity fluctuations occur randomly in time and can have multiple microscopics origins such as thermal fluctuations of molecular positon and orientation[41–44], changes in excitation intensities[45,46], and changes in the local molecular environment[41,42,47]. One possible explanation is some rearrangement of the molecules on the surface such as diffusion[36,48] and orientation changes. Other possible origins include subtle changes of the excited state lifetime, energy and geometry of the molecule. In principle the fluctuating SERS spectrum reveals the unique molecular geometry, the instantaneous vibrational state, and also the environmental interactions with the molecule. These spectral stochastic changes imply the few or single-molecule sensitivity, as it is unlikely that a large ensemble of molecules would simultaneously fluctuate in this way.

Spectral diffusion is another commonly seen characteristic on the single- or few-molecule SERS spectra. Spectral diffusion is seen as shifts of the energy of the vibrational modes as a function of time. It is possible that similar factors such as orientation and structural variation can cause both spectral diffusion and blinking, Spectral diffusion can indicate the changes of the energies of the vibrational modes resulting from changes in the electrostatic environment like the presence of a charged or polar contaminant or external fields[49,50].

In the sense that they originate from the interactions of the adsorbed molecule and the metal surface, the spectral blinking and diffusion are all attributed to the chemical enhancement and are seen over all the different types of molecules studied in this thesis.

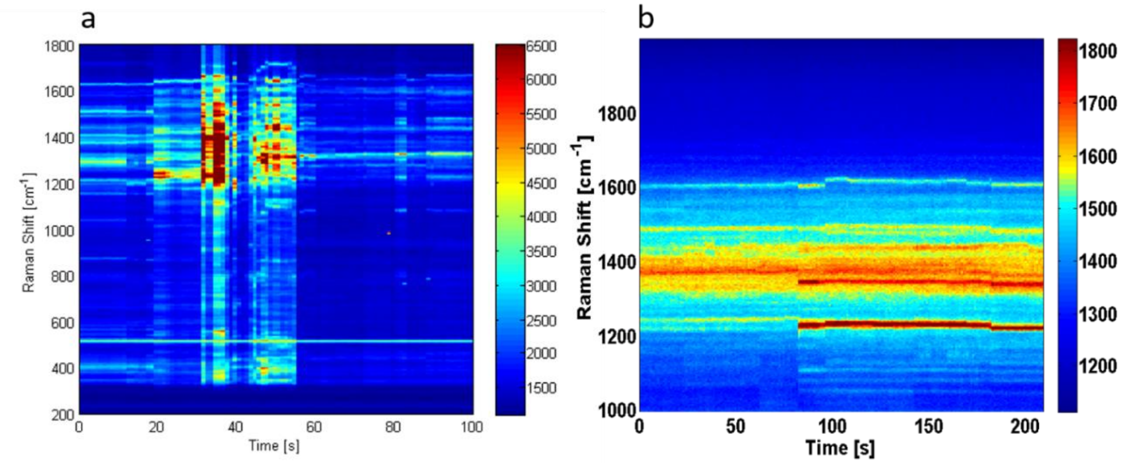

Figure 1-7 Raman spectra as function of time. Raman spectra of (a) BPE and (b) p-MA assembled nanojunction. Spectra were aquired in vacuum at 80K. The color bar represents the intensity of the Raman spectrum. The blinkings occur as the sudden change of the color. The spectra diffusions appear as discontinuities in the straight lines with respect to time.

1.5 Molecular junction

Molecular junctions consist of two metal electrodes whose closest distance ranges from the Angstrom to the nanometer scale. A molecule is placed in the junction and bridges the two electrodes, as shown in Figure 1-8. The concept of constructing a functional molecular device using single molecules as active elements was first proposed by Aviram and Ratner in 1974[51] and the field of the molecular electronics has drawn significant interest ever since. The molecular junctions possess the ideal geometry for studying the electrical properties of the single molecules.

Fabricating single molecule junctions is very challenging. Traditional electron beam lithography cannot reach the resolution of the molecular scale. There are many ways to achieve the molecular scale resolution to make the molecular junctions. The widely used methods are break junctions including electromigration and mechanical break junction[52–61] and tip junctions such as STM style[62–71] or AFM style junctions.

Mechanical junctions require a lithographically defined narrow metallic wire suspended over an etched insulating (polyimide or oxide) layer on top of a flexible substrate. Bending the substrate will elongate the wire until it breaks somewhere along the wire and forms the two electrodes with close spacing. Figure 1-9a is an example of the mechanical break junction.

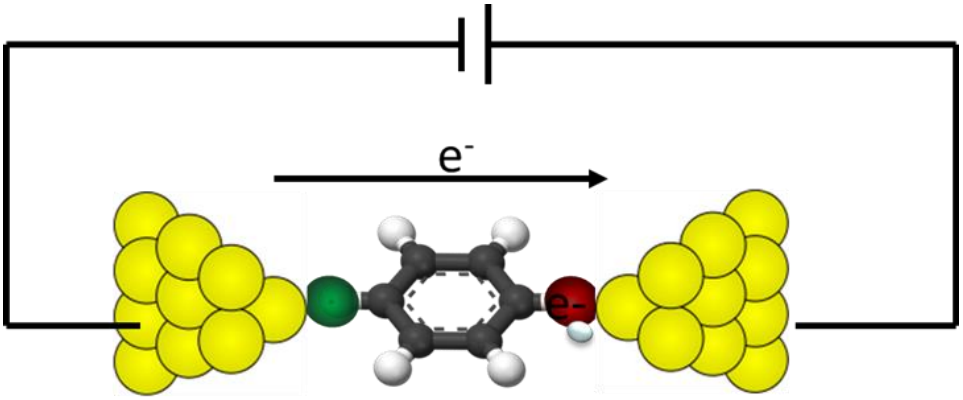

Figure 1-8 Illustration of the molecular junction. Two electrodes are biased and a target molecule bridges the gap to complete the circuit.

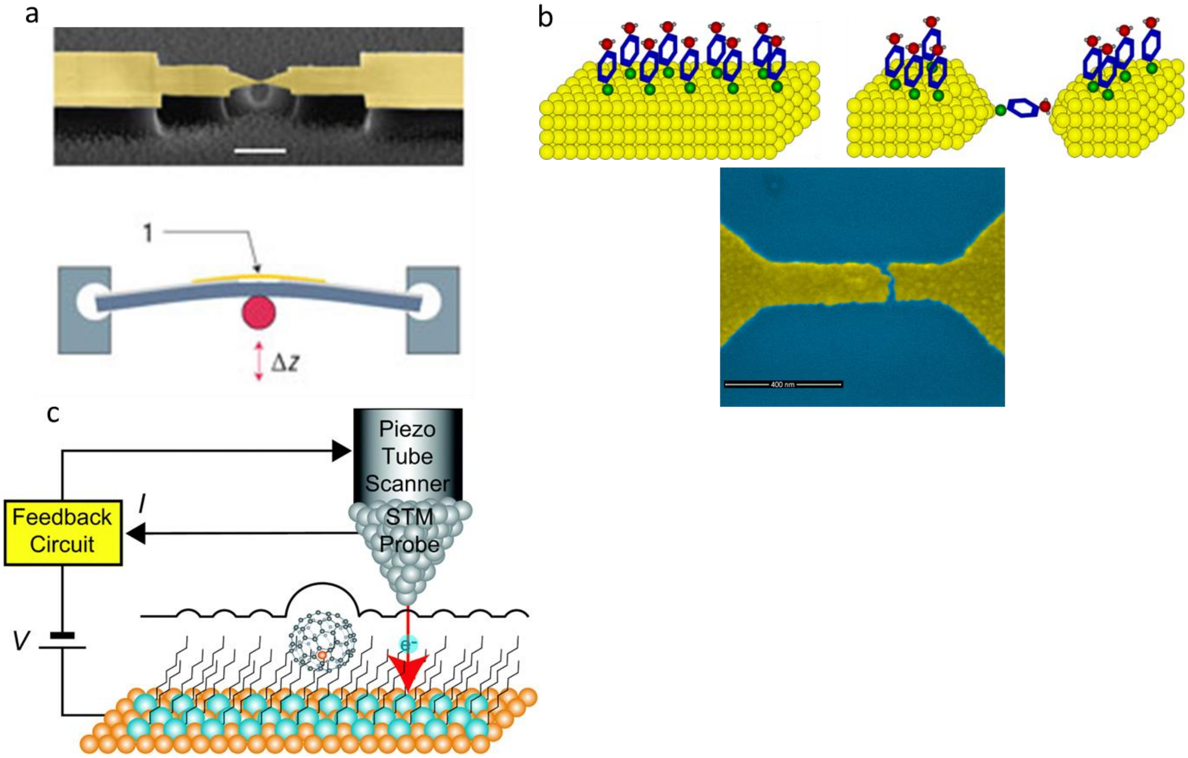

Figure 1-9 Illustration of different types of molecular junctions. (a) Illustration of a mechanical break junction. Reproduced from reference [72]. (b) Electromigration process (top) and SEM image (bottom) of electromigrated junction. (c) Schematic view of the STM style molecular junction. Reproduced from reference [62].

The method adapted in this thesis is the electromigrated junction. This was first developed by Park *et al*. in 1999.[73] A controllable voltage is applied across a narrow metal constriction usually predefined by electron beam lithography. The momentum transfer from the charge carriers, the electrons, to the ions enhances the ion motions and causes some atoms move out of place relative to their neighbors. This process is more rapid if the local current density is large, such that a constriction can be driven to neck down to form a nanoscale interelectrode gap. There are two ways to incorporate the molecules into the gap. If the constriction is covered by a monolayer of target molecules, there is some chance that the molecule will just fall into the gap and bridge the two sides of the electrodes. Another approach is to spin coat the molecules from solutions or sublime a monolayer of the molecules onto the whole surface. However, several concerns about the electromigrated junctions must be accounted for when using these structures to study molecules at the metal interfaces. The electromigration may cause a local temperature rise which might damage the molecule or trigger some chemical reactions between the molecule and metal. The electromigration may also leave some metal debris in the junction and act as an “artificial molecule” and mask the intrinsic nature of the target molecules. The advantage of the electromigrated junctions is the freedom of integrating a third electrode as the back (top) gate to further tune the energy levels of the molecules in the junction relative to the metal electrodes.

The tunneling conductance in a bare junction occurs in a roughly molecular volume and can be described in the following equation:

Equation 1-3

$$\mathrm{G} = \mathrm{G}_0 e^{-\beta(d-d_0)}$$

Here d is the internuclear spacing between two closest atoms in the two electrodes, β is the attenuation factor, and G_0 is the conductance quantum, defined as $G_0 = \frac{2e^2}{h} = 7.748 \times 10^{-5}\ S$, which appears when measuring quantum point conductance. Because of the exponential dependence of the wavefunction overlap on the spatial separation, the conductance is dominated by the point in the nanojunction where atoms of the separate electrodes are the closest. When the molecule is placed in the nanojunction, the conductance is dominated by the molecule itself.

When molecular junctions are voltage-biased, multiple processes involving the interaction between electrons and phonons, electron and electrons, and energy dissipation may happen[1,2,72,74,75]. A typical way to characterize the electrical properties of the single molecule junction is to measure the *I*-*V* curve. The measurements can be generalized by a two terminal (source and drain) or three terminal (source drain and gate) measurements in Figure 1-10. In the two terminal case, the molecule is sandwiched between two electrodes which serve as the source and the drain.

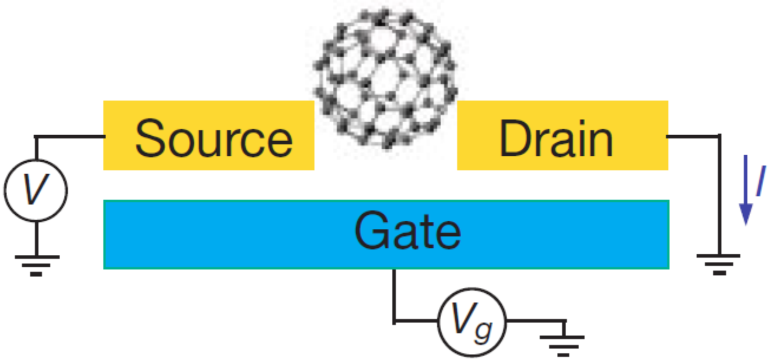

Figure 1-10 Three terminal electrical measurement scheme of a single molecule junction. Reprinted from ref[76]

There are multiple transport mechanisms that can take place in the molecular junction including tunneling and hopping[77]. The tunneling is the dominant mechanism in small molecules. The characteristic of the tunneling can be divided into two categories: resonant and nonresonant, as shown in Figure 1-11. In the energy diagram of the tunneling event, two electronic energy levels of the molecules are of interest: the lowest unoccupied molecular level (LUMO) and highest occupied molecular level (HOMO). The alignment of the HOMO and LUMO relative to the metal Fermi level is determined self-consistently by metal-molecule charge transfer, including lifetime broadening of the molecular levels and the screening environment provided by the metal. When unbiased, the Fermi levels of the two electrodes are the same. When an external voltage is applied to the two electrodes, the Fermi energy level of the source and drain will be shifted and also the coupling between the molecule and source and drain will change the energy alignment of the molecule relative to the Fermi energy of the source and drain. When the a voltage difference is applied to the source and drain , tunneling can take place via LUMO or HOMO; which one dominates depends on the energetic alignment[78]. If the tunneling happens via the LUMO, electrons flow from the source and tunnel through the molecule which can function as an effective tunnel barrier[79] in the nonresonant case and off to the drain. A third terminal, a *gate* electrode can in principle capacitively shift the LUMO(HOMO) of the molecule relative to the source and drain Fermi levels, depending on the relative strength of the capacitive coupling and the coupling of the molecule to the electrodes.

The physics behind the tunneling event at the molecular junction can be characterized by the I-V curve. Figure 1-11 illustrates some possible mechanisms of the tunneling. In the nonresonant scenario, as shown in Figure 1-11a,b, the LUMO is above the Fermi level of the source and drain, the electron either travels through the LUMO ballistically (Figure 1-11a) through a second-order "cotunneling" process, or has some energy exchange with the molecule during tunneling (Figure 1-11b) ("inelastic cotunneling"). Elastic tunneling current is the ever-present source of the background. In the resonant case, the LUMO is very close to the Fermi level of the unbiased electrodes, and the transmission as a function of bias is peaked as the bias brings the molecular level into the energy window between the source and drain. The result is a pronounced step in the I-V curve and a corresponding peak in the differential conductance, $\mathrm{d}I/\mathrm{d}V$.

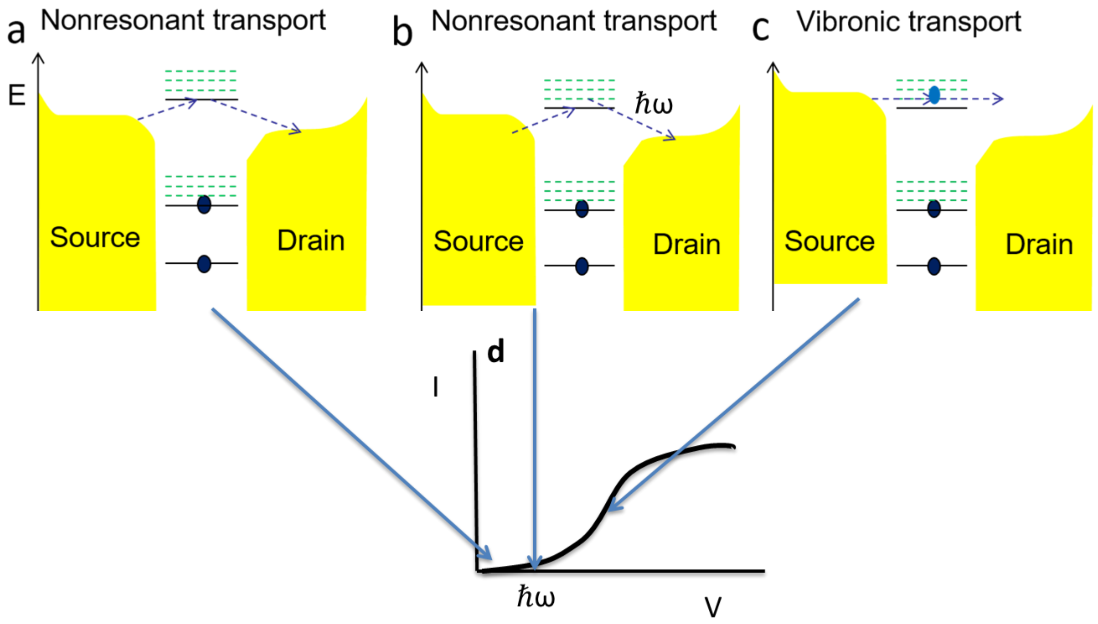

Figure 1-11 Illustration of different tunneling mechanisms and corresponding I-V curves. (a) Ballistic tunneling. (b) Nonresonant tunneling with a phonon excited during the tunneling process. An additional channel contributes to the current which happen at bias over ħω (ω is the phonon frequency), as indicated in (d) I-V curve. (c) Vibronic tunneling. The LUMO of the molecule is close to the Fermi level of the source leading to rapid current increase as shown in (d)

The derivative curves of the I-V characteristics can reveal spectroscopic information about the vibrational features. In fact examining the DC bias dependence of the second derivative of I-V curve, d^2I/dV^2, is the primary means of performing one type of vibrational spectroscopy: inelastic electron tunneling spectroscopy (IETS). An IET spectrum is a plot of d^2I/dV^2 versus V. By differentiating the I-V curve, the changes of the I-V curve can be revealed more clearly. When the bias is sufficiently large that the inelastic process in

Figure 1-11b is allowed, the inelastic channel can then contribute in addition to the elastic cotunneling process. This leads to a kink in the *I*-*V* curve at the vibrational energy threshold as the local phonon is excited. This change in *I*-*V* slope corresponds to a step-like change in the differential conductance curve, as shown in Figure 1-12a, and then a corresponding peak in d^2I/dV^2. In reality, the I-V curve is more complex than the processes illustrated in Figure 1-11. Figure 1-12b gives an example of I-V curve and its derivative curves of a single molecule junction. The effective tunnel barrier shape is affected by the adsorbate layer, and image charge effects round the edges of the barrier as a function of the bias[80–82]. The simple square barrier model is inaccurate[81], and the barrier potential itself is a function of the applied voltage. Thus, the real I–V curve observed over finite voltages is nonlinear and can be asymmetric about zero bias.[83–85], as is shown in Figure 1-12b.

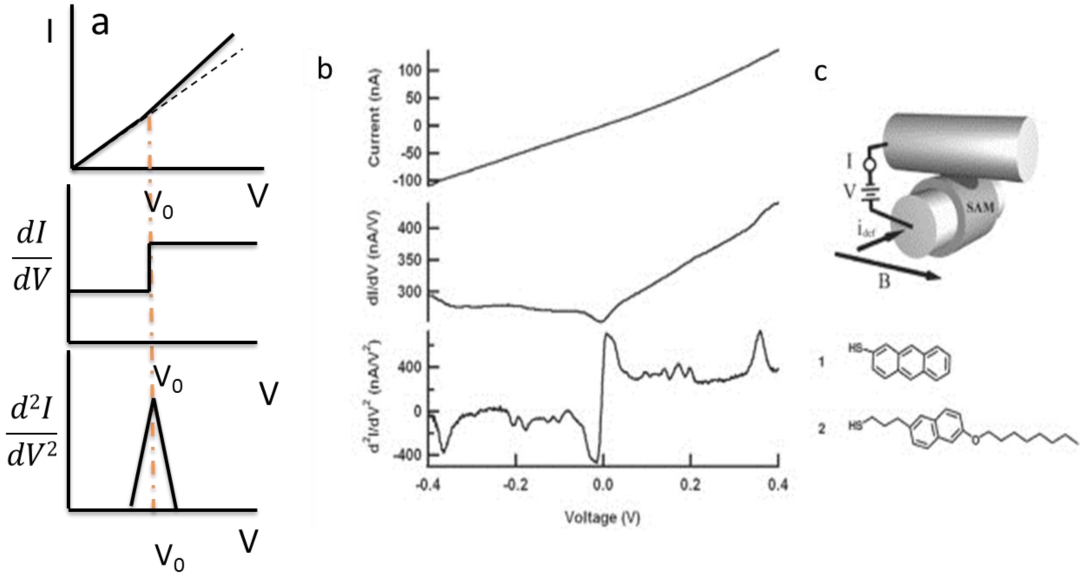

Figure 1-12 Inelastic tunneling spectroscopy. (a) Illustration of the ideal IETS curve. (b) Example of an IETS curve of an actual single molecule junction. Reproduced from reference [83].

1.6 Summary

This chapter covered the basic background knowledge of the optical vibrational spectroscopy: Raman and Infrared absorption spectroscopy. Those are very useful analytical techniques to reveal the chemical information.

In the molecular junctions section, we overviewed the concept of molecule junctions, the fabrication techniques as well as the electrical characteristics. The second derivative of I-V curve is one type of vibrational spectroscopy and reveals the vibrational properties of the molecule in the junction.

The plasmonic effect on the metallic nanostructures, with the ability of providing high electromagnetic field enhancement at subwavelength scale, enables the optical vibrational spectroscopy at single molecule level and acts as an *amplifier* for the optical and electrical characterization of the molecular junction particular in this research.

The background knowledge overviewed in this chapter is essential to understand the physics underlying the experimental results in the following chapters.

Chapter 2

SERS in nanojunctions

This chapter will be focused on the fabrication process of the molecular junctions as SERS substrate, and summarizing experimental studies of several fundamental properties of the nanogap structures.

2.1 Sample fabrication and measurement

2.1.1. Sample fabrication

The SERS substrate studied in this thesis are nanogap structures fabricated through two methods: electromigrated nanogaps and self-aligned nanogap structures.

The electromigration on nanowire is one method pioneered by Park *et* al[73], to produce nanometer-sized gap between two metallic electrodes. The conductance of the molecular junction produced by electromigration is dominated by molecular volume and have been used for numerous electrical measurements[86–93].

Electromigration is initiated by large current passing through the metallic nanowire. Two effects contribute to electromigration: Momentum transfer and electric field. The momentum transfer originates from conduction electrons, which move in response to the applied bias. These electrons scatter off of defects in the periodicity of the metallic lattice, such as vacancies, surfaces, and grain boundaries, and transfer momentum to the ions, leading to ionic diffusion. Once a void is created in the nanowire, this will cause the current density to increase in the vicinity, enhancing the rate of momentum transfer and facilitating growth of more voids. That usually occurs at the grain boundary or lattice defects. The non-thermal nature of the momentum transfer process allows the electromigration to happen even at initially cryogenic temperatures like 4K. The electric field also exerts forces on any charged defects in the metallic nanowire. Since the momentum transfer passes energy to the vibrations of the atoms, the local temperature will rise inevitably, which further accelerates the electromigration process through thermal enhancement of ionic diffusion rates.

To get a controllable electromigration, we use a circuit with feed-back loop to produce the nanojunction with desired conductance. For the measurements in this thesis, the electrical signal was applied and measured using the DAC controlled by the computer. First a bias is applied across the gold nanowire. The bias is ramped up to a preset value V_0 and the resistance of the nanowire is monitored to check for an increase beyond that for pure heating, which would indicate the onset of migration. The current is measured as function of the applied bias as well as the change of the current. The value of the bias is set to zero once a sudden drop of current passes a set threshold. This process is repeated by adjusting the starting value of the bias V_0 until the conductance reach the predetermined value. Migration is concluded when the conductance is less than the conductance quantum $G_0=2e^2/h$. Most of the electromigration used for the experiments in this thesis was done at liquid nitrogen temperature around 80 K, some were done at 4K with higher V_0. Nanogap junctions prepared in this way have a yield of getting a device with measurable Raman signals of around 30%.

Another approach to generate nanogap junctions is a self-aligned technique[94] involving two steps of lithography. In the first step one metal object was patterned on the silicon wafer via e-beam lithography. After development, metal layers of 1 nm titanium, 20 nm gold and 11 nm chromium were evaporated onto the substrate, followed by liftoff of the remaining resist. The chromium layer oxidizes in air and forms a few-nm chromium oxide layer that acts as a shadow mask for the subsequent steps. In the second step of lithography the other half of the object was patterned overlapping the one fabricated in the first step. The same set of metal layers was again deposited. Following liftoff, the substrate was then placed in a chromium etchant to remove the overlapping materials as well as the chromium layer, leaving gaps formed between two adjacent rods. This method can massively produce nanogap structures with gap sizes below 10nm.

All samples presented in this thesis were fabricated in the same fashion unless noted otherwise. Electromigrated samples were fabricated on n-type Si with 200 nm of thermal oxide. Nanowires approximately 120 nm wide were defined by e-beam lithography and e-beam evaporation of 0.7 nm Ti and 13 nm of Au. The nanowires are approximately 1μm long and connected to larger electrical leads prepared by shadow mask. After evaporation of the metal, liftoff was performed in acetone and the nanowires cleaned of organic residue by exposure to O_2 plasma for 1 minute before assembled with molecules.

2.1.2. Optical and electrical characterization

Raman spectroscopy is performed using a home-built Raman microscope system, with an incident wavelength of 785 nm. Modes with Stokes or anti-Stokes shifts below a threshold (formaly 300cm^{-1} when the data presented in this thesis were acquired, now 60cm^{-1})are cut off by a notch filter. A piezo-actuated lens mount rasters the diffraction-limited beam over the sample surface, allowing the acquisition of spatially mapped Raman response. The mapped Si Raman intensity at 520 cm^{-1} is used to locate the center of a bowtie structure. Following electromigration, a further Raman image determines the location of the nanogap's plasmonic Raman hotspot as shown in Figure2-2. Raman spectra at that location are then acquired simultaneously with electronic transport data (I and dI/dV as a function of V, using a current preamplifier; V sourced by a digital-to-analog converter (DAC) integrated into a lock-in amplifier; differential conductance measured via lock-in using a AC signal of several mV added to V with a summing amplifier). The experimental configuration is shown in Figure 2-1.

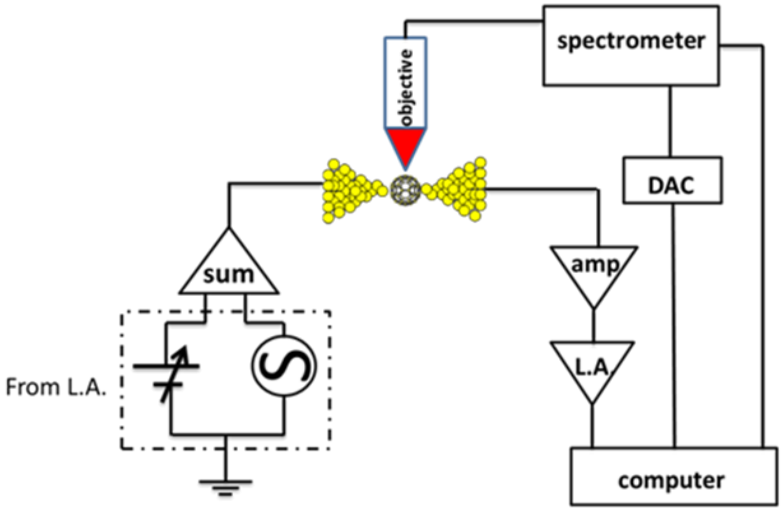

Figure 2-1 Schematic view of the experimental setup.

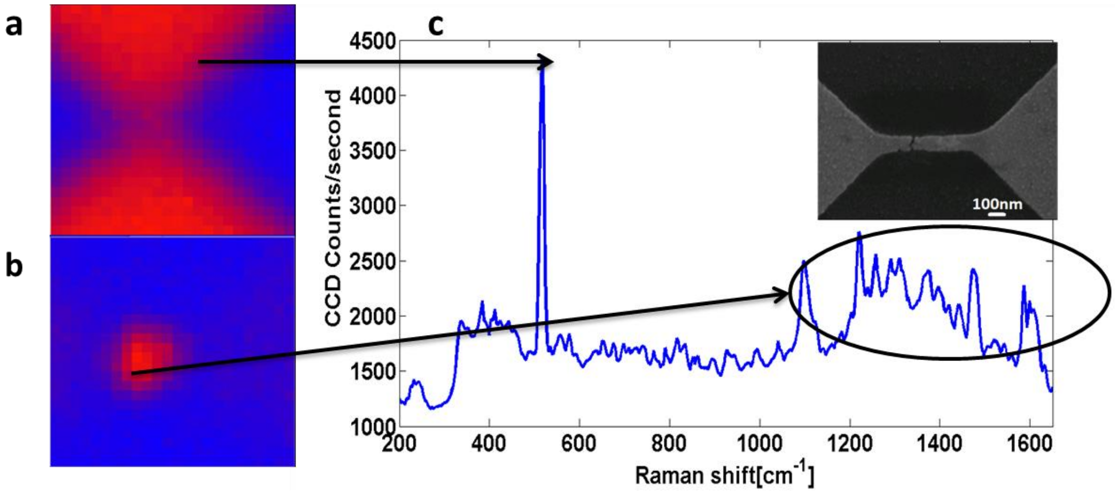

Figure 2-2 Spatial map of the Raman intensity. Spatial map of integrated Raman intensity of (a) Si line centered at 520 cm^{-1} (b) vibraional modes with energies in the range of 1000cm^{-1} to 1600 cm^{-1}. (c) SERS spectrum taken at the center of the C_{60}-gold junction, (inset) SEM image of this junction.

The Surface Enhanced Infrared Absorption (SEIRA) measurements were performed using a FTIR microscope (Nicolet continuum) attached to a FTIR spectrometer (Nicolet iS50) and equipped with a mercury cadmium telluride (MCT) detector. Data were acquired at transmission mode in purged air at room temperature. The field of view was set by a 15X objective and a 40×60 μm^2 aperture. The transmission spectra were acquired with 4 cm^{-1} resolution and averaged over 1200 scans. For spectroscopic measurements with polarized light, a ZnSe polarizer was inserted in the infrared light path. Part of the SEIRA study was conducted on the FTIR microscope in Prof. Halas group. The data acquired from that microscope is not adapted into this thesis.

2.2 Transport measurements

The molecular junctions electromigrated *in situ* can be capacitively connected with a third electrode, which give one more degree of freedom to tune the electronic levels of the molecule. The LUMO(HOMO) position of the molecule relative to the Fermi levels of the source and drain electrodes can affect the vibrational states of the molecules via the electronic occupancy, as will be discussed in more detail in Chapter 3. By bringing the conduction orbital of the molecule close to the Fermi level of the source and drain, dramatic changes of the vibrational modes are likely to be observed. Purely electronic measurements in this gated regime have been performed by several groups including our own[76,95,96]. Vibrational features in the tunneling conductance have been identified[76,96,97], and signatures of vibrational shifts with gate voltage have also been identified [96,98]. Such electronic experiments require long, stable measurements and cryogenic (~ 4.2 K) conditions.

We have attempted to perform simultaneous measurements of Raman spectroscopy and electronic transport in this gate-coupled regime. Unfortunately these measurements have been plagued by instability of junction configurations, possibly due to optical heating, and by poor Raman signal. Differential conductance of the C_{60} junctions is measured at 10K without radiation as function of the source-drain bias V and the gate voltage V_g and shown in the contour plot in Figure 2-3. The darkest areas on the left and right of the plots indicate the regions of minimum current. The bright regions located outside those areas correspond to high conducting states.

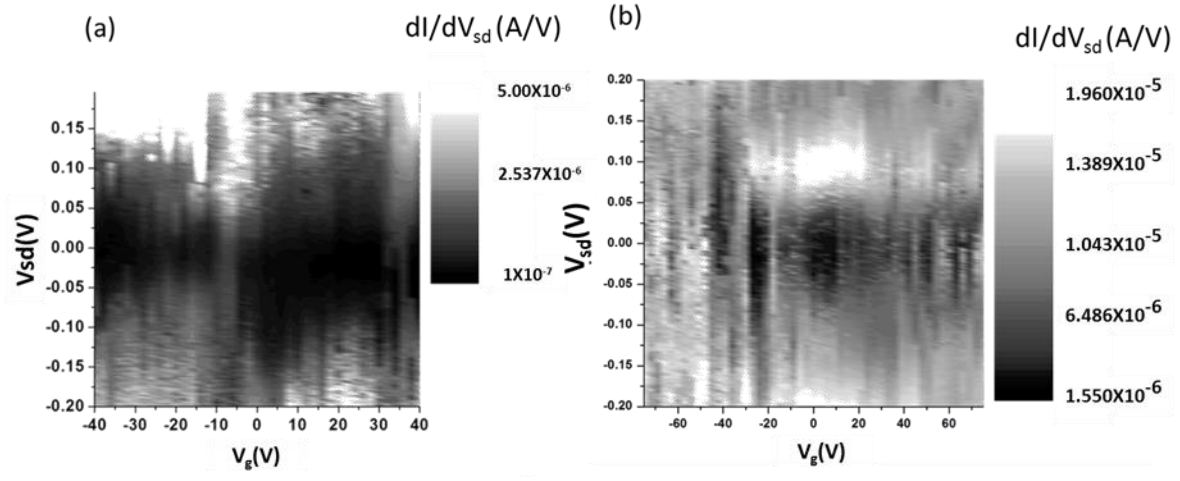

Figure 2-3 Differential conductance as a function of the source-drain bias and gate. (a) At 10K with no illumination. (b) At 10K with 785 nm laser focused on the junction.

This behavior is the signature of a single-electron transistor, a device containing a small island attached to electrodes by tunnel barriers and whose charge state can be tuned using a gate voltage, shown in Figure2-4 The charge state of the C_{60} is stable at low V_{sd}(dark regions). An electron does not have sufficient energy to tunnel onto the island and therefore current is blocked (Coulomb blockade). The region between the dark and bright defines the tunneling thresholds for transitions between charge states. Unlike bright lines as clear boundaries of the blockade reported elsewhere[76,86], the smooth transition is due to the thermal broadening. Conductance in the vicinity of $V_{sd} = 0$ is allowed at a value of gate voltage V_g, where the charge states are degenerate. That value is referred as degeneracy voltage V_c; in this case V_c is around -10V.

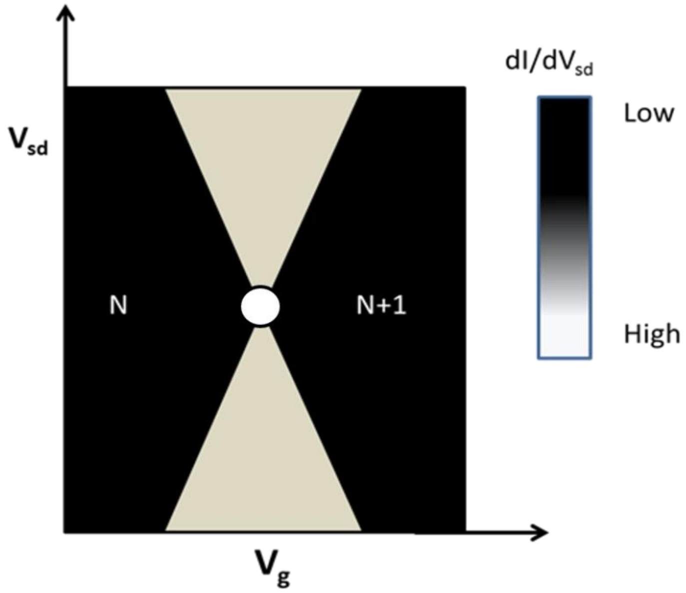

Figure 2-4 illustration of single electron transistor

The presence of the Coulomb blockade is a strong evidence of the single molecule because the degeneracy voltage V_c is different for each molecule owing to local variations in the electrostatic environment.

Figure 2-3 b shows the same measurement on the same junction upon illumination of the junction. The diamond features are absent and the differential conductance contour plot is far noisier. There are several possible explanations: the presence of the radiation will deposit heat into the junction. When the plasmons are excited in the nanojunction assembled with molecules under illumination, heat dissipation via different mechanism discussed in the following section can result in unwanted experimental consequences. These include broadening of the IETS features in the tunneling spectra, increased thermal noise, and the instability of the junction charge environment through perturbation of trap states in the nearby substrate oxide. The local plasmons can also exert forces on the molecule and electrodes through the local electric field gradient, and these could result in a geometrical configuration change of the molecule such as diffusion to a different adsorption site or an orientation change. These may affect the coupling efficiency of the molecule and gate. After the laser was turned off, differential conductance was measured and didn't show the same pattern in Figure 2-2 a, which suggests changes the molecular junctions undergo upon illumination in these conditions can be irreversible.

2.3 Simultaneous Raman and conductance measurement

As discussed in the previous chapter, blinking and spectral diffusion are commonly observed from the molecular junctions. Simultaneous electrical and spectral measurements show the correlation in time between stochastic changes in the Raman spectra and the conductance of the molecular junction. One example is shown in Figure 2-5.This is consistent with the nanoscale junctions assembled with other types of molecules such as OPV3[99] and a fluorinated oligophenylyne ethynylene.[5] As discussed in the previous chapter, the correlations are strong indications of the few-or single molecule nature of the junction.

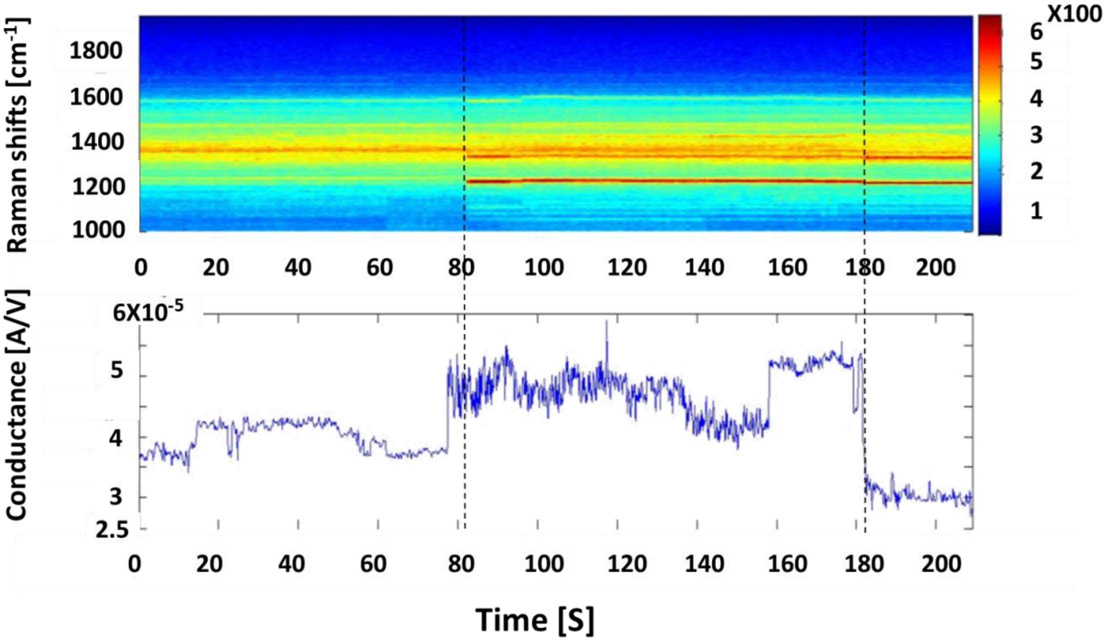

Figure 2-5 Raman spectra of p-MA assembled junction acquired simultaneously with the conductance as a function of time at 80K in vacuum.

2.4 Polarization dependence

To understand the plasmonic nature of the nanojunctions, measurement of polarization dependence was performed on the self-aligned and electromigrated junctions. In many SERS investigations by other groups of nanogaps between particles or electrodes, incident light with the electric field polarized across the gap (along the interparticle or interelectrode axis) is generally known to induce the strongest surface enhanced Raman spectroscopy (SERS) emission.[100] However, on the electromigrated or self-aligned nanogap structures with extended electrodes, we observe the opposite. The nanogaps give rise to the maximum SERS signal when the incident light is polarized in the transverse direction.

Figure 2-6 gives an example of polarization dependence of the electromigrated junction assembled with C_{60}. The intensities of the vibrational modes of the C_{60} reached a maximum with light polarized at 90 degrees, while the Raman intensity of the Si 520 cm^{-1} mode from the substrate does not follow the same trend. The fact that the Si Raman maxima are shown at both longitudinal and transverse polarization is due to the crystal orientation of the Si[101]. The polarization measurments on the molecular junctions confirm that any observed polarization dependence of the SERS signal is due to the nanogap and not caused by any asymmetry in the optical path of the Raman signal.

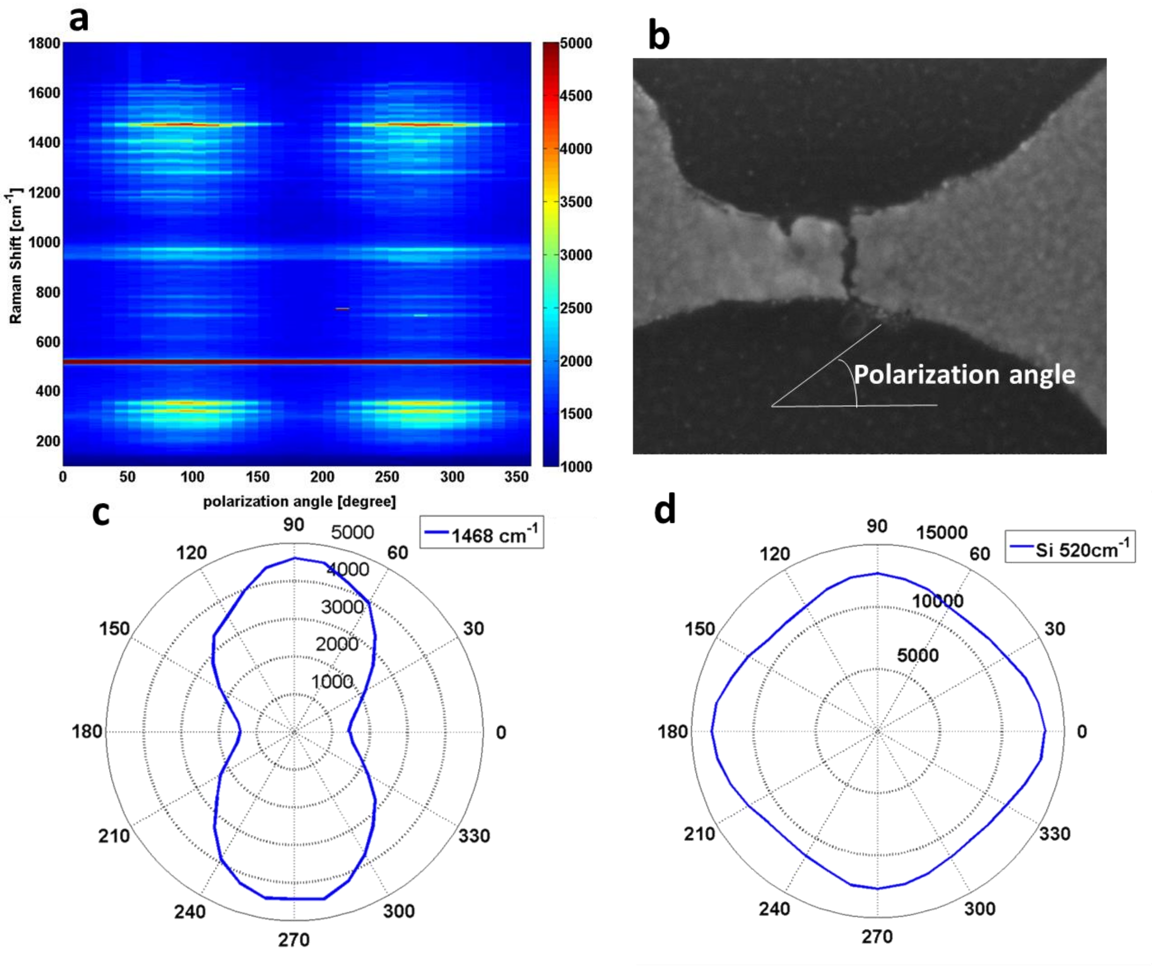

Figure 2-6 SERS spectrum of C_{60} as a function of polarized light. (a) Raman spectrum of C_{60} junction fabricated by electromigration as a function of polarization angle of incident light. (b) SEM image of the electromigrated junction with Raman spectrum shown in (a). (c) Polar plot of the intensity of the vibrational mode with energy 1468 cm^{-1} and (d) polar plot of the intensity of the silicon Raman mode as functions of polarization angle.

To further understand the origin of the anomalous polarization dependence, Cathodoluminescence(CL) imaging was used to examine the radiative plasmon mode. As shown in Figure 2-7 b, the brightness of each pixel in the CL image is proportional to the intensity of the radiated light collected from the whole structure when the electron beam is positioned at that pixel. Electromagnetic simulations were done using COSMSOL finite element methods. Electromagnetic enhancement and charge distribution were calculated and shown in Figure 2-7d,e. The simulated results show that when the light is polarized along the transverse direction, the very complicated, multipolar mode at the gap region rises through the coupling with the transverse plasmon mode in the nanowire.

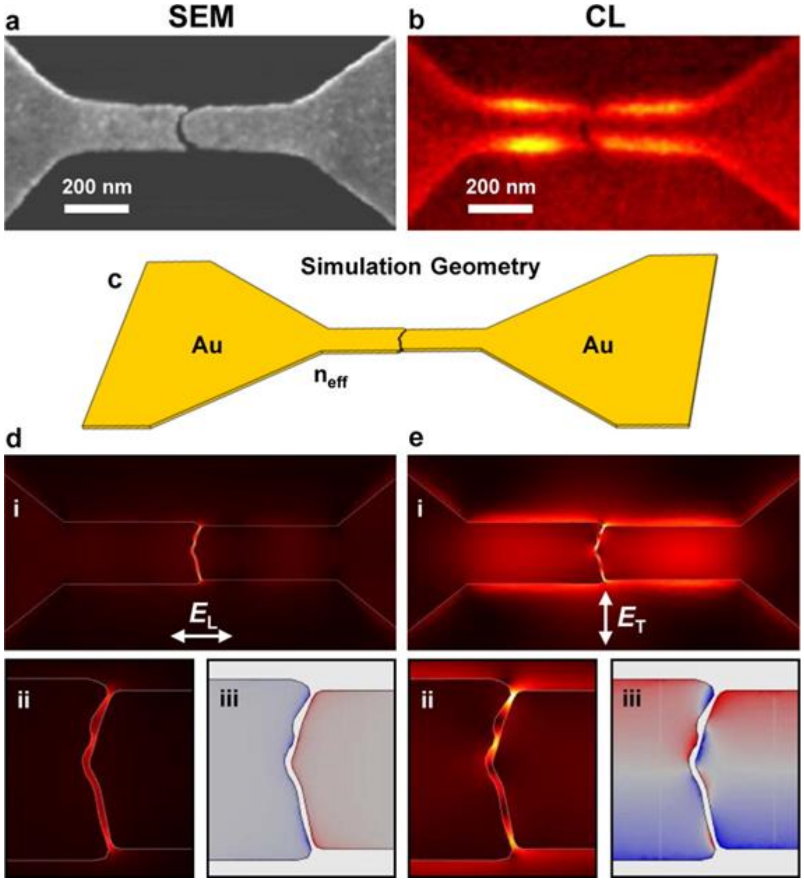

Figure 2-7 Cathodoluminescence image and simulations on a self-aligned structure. Reprinted from reference [102]*. (a) SEM image of a nanogap acquired*

in parallel with (b) an unpolarized cathodoluminescence excitability image. (c) Simulation geometry of a self-aligned nanogap used in COMSOL finite element method calculations. Calculated electromagnetic-field enhancement (i, ii) and charge distribution (iii) due to incident Gaussian light with (d) longitudinal and (e) transverse polarization. Local, very intense multipolar plasmon modes in the gap are excited efficiently when the light is transverse polarized (along the gap), because that light couples well into transverse plasmon modes of the wire. The traditional longitudinal polarization (across the average gap direction) does not efficiently excite large local fields in the gap.

The measured polarization dependence of the SERS signal of BPE assembled self-aligned junction fits well with, and is directly proportional to, the calculated local enhancement, as shown in Figure 2-8. This indicates the polarization dependence of the overall SERS enhancement factor is directly proportional to the polarization dependence of the local intensity.

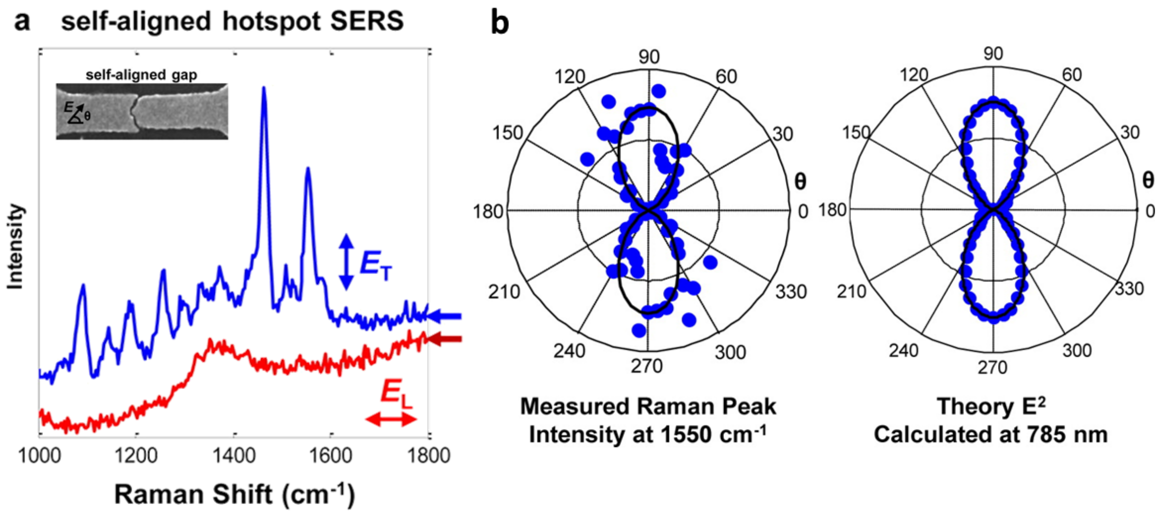

Figure 2-8 Reprinted from reference [102]. (a) SERS spectra of BPE at the center of a self-aligned nanogap with transverse, ET, and longitudinal, EL, incident polarization. (b) Left: Measured SERS intensity at a peak position of 1550 cm^{-1} *as a function of incident laser polarization. Right: Calculated local enhancement of excited mode as a function of incident laser (λ = 785 nm) polarization. Plotted is the normalized electric field squared at the gap calculated with the finite element method for simulated nanogap geometry.*

Polarization dependence of self-aligned structures without extended electrodes is studied with the radiation in the infrared regime. The nanogap structures consisting of discrete rods show that the maximum enhancement is created while the electric field is in the longitudinal direction (along the rod). The electric field is stronger in the nanogap structure with the two rods aligned side by side than two isolated rods, suggesting that the dark modes in the nanogap improve the electric field enhancement, however the most efficient way of coupling is along the rod direction. More discussion will be shown in Chapter 5.

2.5 Molecular junctions to examine energy dissipation

2.5.1. Background in SERS spectrum

A decaying continuum background at low wavenumber shifts is commonly seen in SERS emission from the electromigrated molecular junction. This background is localized at the diffraction-limited area at gap region, whereas when the excitation laser is incident on the silicon substrate or on gold away from the gap, this background is absent. The origin of this continuum is likely from the Raman scattering from the electrons from the gold.[103] On the junctions with molecules with SERS signals, the background correlations are more visible. The background is correlated with the SERS signal consistently despite the spectral blinking. Figure 2-9 shows the Raman spectra of C_{60} junction. In the spectral range of 1000cm^{-1} to 1600 cm^{-1}, along with the enhanced vibrational modes, a hump is also observed with the SERS signal. The hump is commonly observed on the junction. Its origin is the coupling between surface plasmon electrons and electrons in the metal which serves to increase coupling between the metal's electrons and the incident photons[104]. This hump increases dramatically when strong SERS signal from the molecules are present. It's .likely due to strong interaction between the surface plasmon electrons and the molecular vibrations when the vibrational modes get strongly enhanced in that spectral range. This background becomes very prominent when the SERS signal is strong. On the anti-Stokes side, a continuum is usually attributed to the Raman scattering of the electrons excited above the Fermi level of the metal.

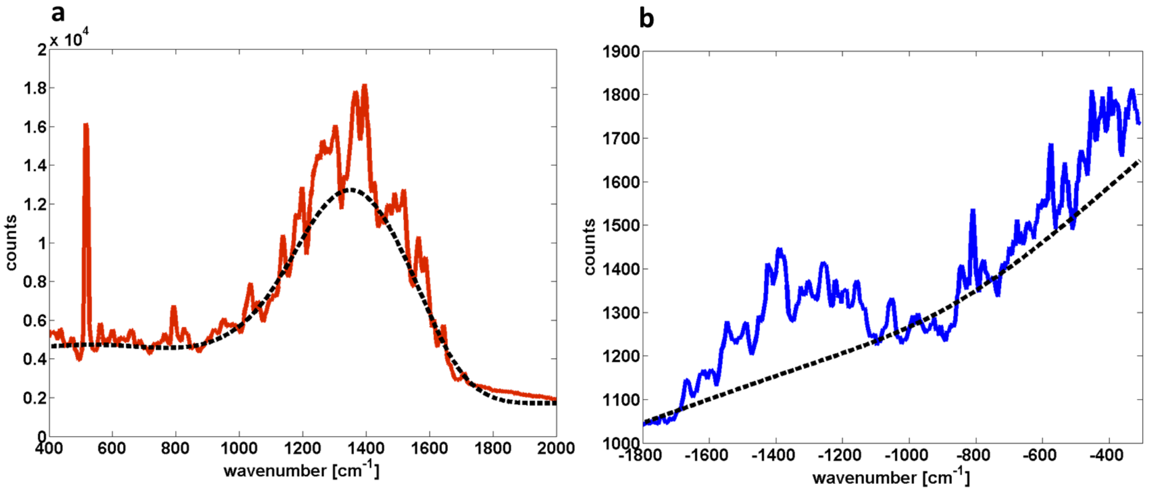

Figure 2-9 SERS spectrum of the C_{60} junction. (a) Stokes and (b) anti-Stokes spectrum. Experimental data is represented by red and blue solid lines respectively. Baseline is represented by black dotted line.

2.5.2. Vibrational and electrical heating at nanojunction

On the nanoscale, energy transforms and dissipates though various mechanisms such as plasmon decay into hot electrons, heat generation though redistribution of electron energy by electron-phonon scattering, and vibration creation though electron-phonon coupling. One way to evaluate the electronic and vibrational distributions at the nanoscale in a molecular junction is to use Raman spectroscopy as a probe. By measuring the intensity of anti-Stokes and Stokes, an effective temperature can be inferred from the equation below:

Equation 2-1

$$\frac{I_{vib}^{as}}{I_{vib}^{s}} = A\frac{(\omega_{in} + \omega_{vib})^4}{(\omega_{in} - \omega_{vib})^4}\exp(\frac{-h\omega_{vib}}{kT})$$

I_{vib}^{as} is the anti-Stokes intensity of the vibrational mode denoted as vib, I_{vib}^{s} is the stokes intensity of the same mode, and A is the coefficient that accounts for the ratio between the anti-Stokes and stokes cross-sections. T is defined to be the *effective* temperature of a particular vibrational mode – the temperature that would be required in thermal equilibrium to produce the steady-state vibrational population inferred from the Raman emission. As each mode couples to the surrounding environment differently, the rate at which energy is deposited into each mode from the electrons and other sources, and the rate at which energy is dissipated out of each vibrational mode, are different. This means that the effective vibrational temperature is usually different from mode to mode.

The effective temperature can be elevated though two processes: optical pumping and electrical pumping. In the optical pumping, the Stokes process creates vibration population, and if the rate of the Stokes process is faster than the vibrational mode's relaxation to environment, that mode's temperature rises above the equilibrium average. Electrical pumping occurs when an electron loses energy and creates a vibrational excitation in the molecule while traveling between the biased source and drain.

Information about the electronic distribution can be inferred from the continuum background in the SERS spectrum. As mentioned before, the continuum is thought to originate from the Raman scattering by electrons in the conduction band of the metal. Anti-stokes continuum emission can only be observed when the incident photon can acquire energy from the hot electrons created above the Fermi surface of the metal, and in this interpretation the continuum at a particular anti-Stokes shift should be proportional to the Fermi distribution at that shift above the Fermi energy. Any bias dependence of the continuum should then be interpreted as an increased effective temperature describing the breadth of the electronic distribution. The anti-Stokes intensity of continuum is dependent on the bias applied on the junction as below[105]

Equation 2-2

$$I_{As} \propto \frac{\varepsilon}{e^{\frac{\varepsilon}{kT_{eff}}} - 1}$$

Where the ε is the applied voltage on the junction and the T_{eff} (V) is the effective temperature of the conduction electrons.

Vibrational and electronic heating on OPV3 assembled junction has been investigated by Ward *et al*[99]. Based on the same procedures, we examined the heating on C_{60} junctions. The anti-Stokes and stokes of one example C_{60} assembled nanojunction before and after baseline subtraction are shown in Figure 2-10 a and b. In the anti-Stokes spectrum, the intensity of vibrational modes increases with larger applied bias. Curvatures in vibrational energy as a function of bias are observed from vibrational modes in the stokes spectrum, and the origin of this effect will be discussed at length in Chapter 3.

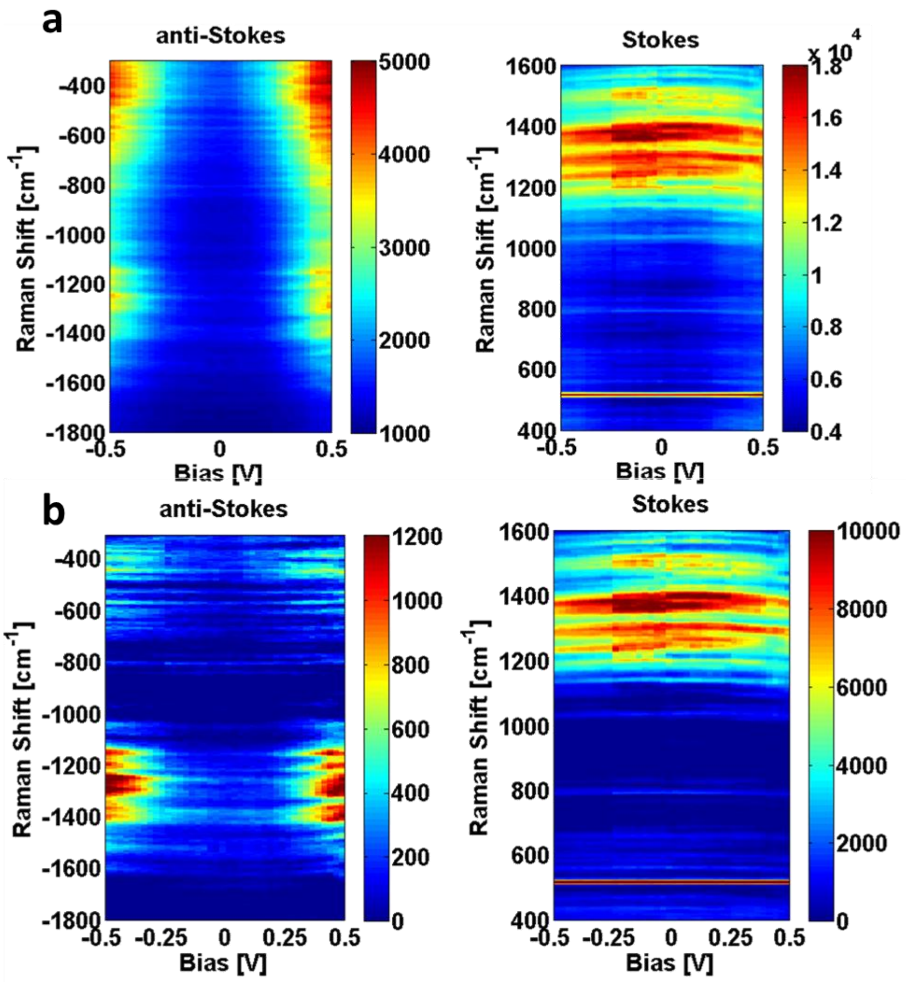

Figure 2-10 Anti-Stokes and Stokes spectra of C_{60} (a)before and (b) after baseline subtraction in nanojunction as a function of bias.

To examine the vibrational and electronic energy dissipation, the continuum background in the SERS spectrum was subtracted from the spectrum. An asymmetric lease square algrithm[106] is implemented for the baseline fitting of the Raman emission as a function of energy, as shown in Figure 2-11.

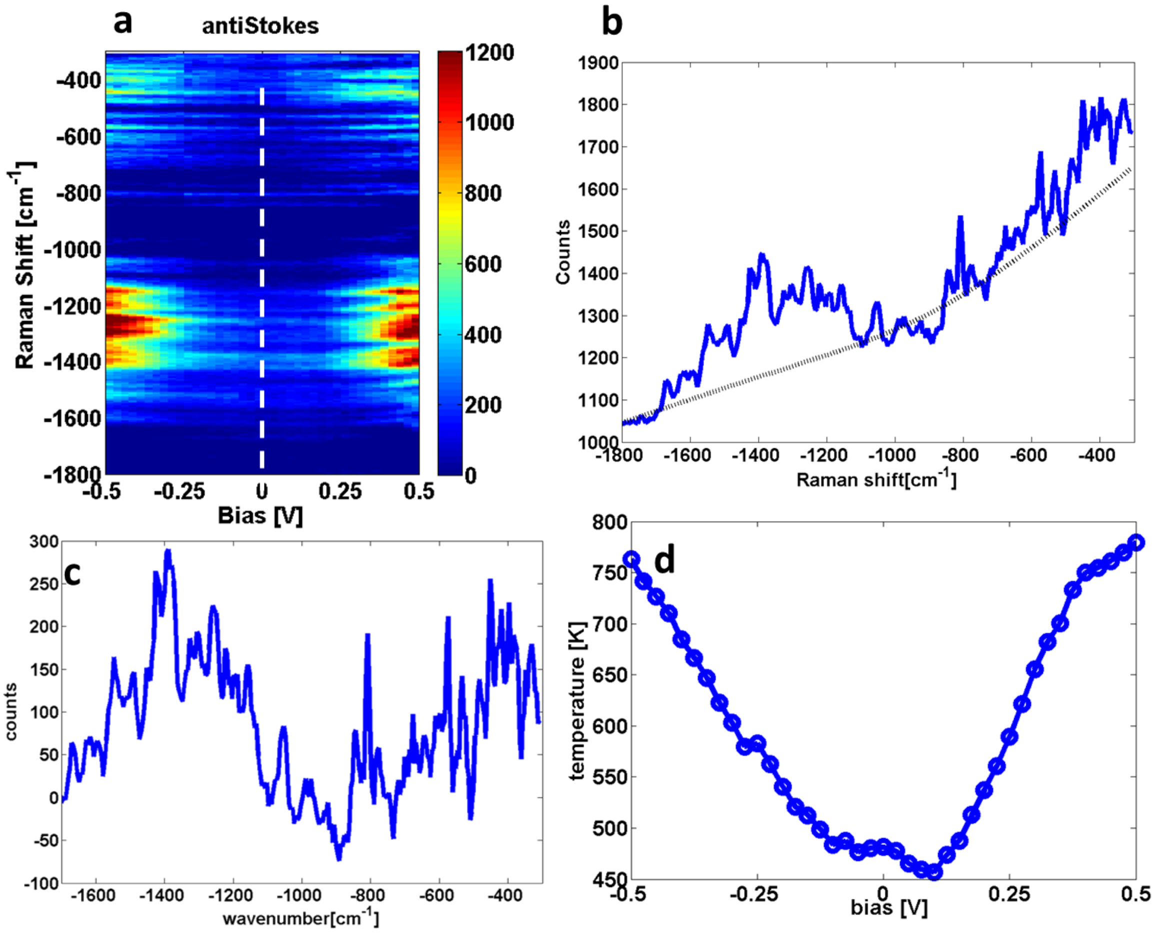

Figure 2-11 Fitting processdures to obtain background continuum of C_{60} junction. (a) Background subtracted anti-Stokes spectrum of the C_{60} in nanojunction at different bias (b) Anti-Stokes spectrum of (a) at 0 bias (solid blue line) and fitted baseline (dashed black line). (c) Baseline corrected anti-Stokes spectrum.(d) Fitted temperature from the anti-Stokes continuum

The subtracted baseline was fitted to the fermi function based on Equation 2-2 and the effective electron temperature was derived from the fitted curve as one fitting parameter. Figure 2-11 d shows the effective temperature as function of bias. The effective temperature rises as the bias applied to the C_{60} junction increases. A ~300K change in temperature is observed over 0.5V range, higher than reported on the OPV3 junction[99]. The asymmetry of the effective temperature as function of bias could be attributed to hot electron generation in the two electrodes at different rates or different thermal coupling of two sides of the nanojunction to the bulk electrodes.

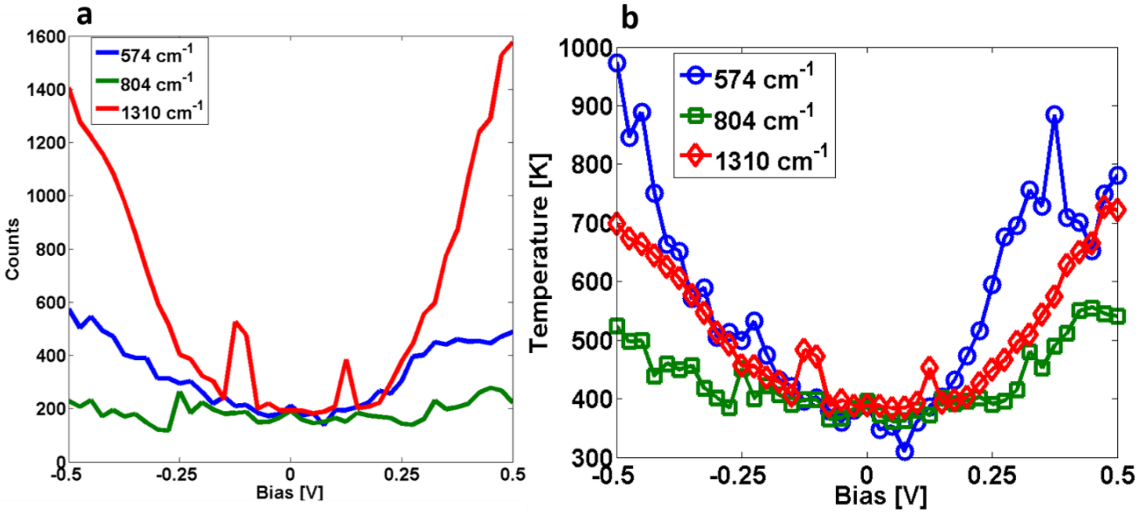

Figure 2-12 Vibrational heating of the C_{60} junction (a) anti-Stokes intensity of selected vibrational modes as function of bias.(b) Calculated effective temperature at different bias

Figure2-12 shows the vibrational heating of the C_{60} junction. Three vibrational modes with energy 574 cm^{-1}, 804 cm^{-1}, 1310 cm^{-1} are chosen to fit. In Figure 2-12 a, as the bias is increased, anti-Stokes peaks of mode 574 cm^{-1} and 1310 cm^{-1} appear and become stronger. In particular, the count rates for peaks near 574 $cm^{-1}$and 1310 cm^{-1}do not rise noticeably above 200 counts until the dc bias exceeds thresholds of approximately 140–

150 mV, similar to observations without baseline corrections[107] in Figure 2-13. Figure 2-12 (a) shows some sudden intensity change of mode 1310 cm^{-1} at around ±0.15V due to the spectra blinking and fluctuates. The intensity change of mode 804 cm^{-1} is much smaller over the ± 0.5bias compared with the other two. At bias below 0.15V, all three modes show detectable signals due to optical pumping. Effective temperatures of each mode are calculated based on Equation 2-1 and shown in Figure 2-12 b. Until the bias exceeds 140-150mV, no increase in effective temperature is observed and the effective temperatures of all three modes are very close in value. Once the bias exceeds this threshold, we see an increase in effective temperature with increasing bias. The bias dependent effective temperature is evidence of electrical pumping. Over 600K temperature increase in the effective temperature of mode 574 cm^{-1} and over 300K of mode 1310 $cm^{-1}$is observed, demonstrating that vibrations may be driven far from equilibrium via optical and electrical pumping. The effective temperatures are different for different vibrational modes, which suggest effective cross-sections for electron-vibrational pumping differ from mode to mode.

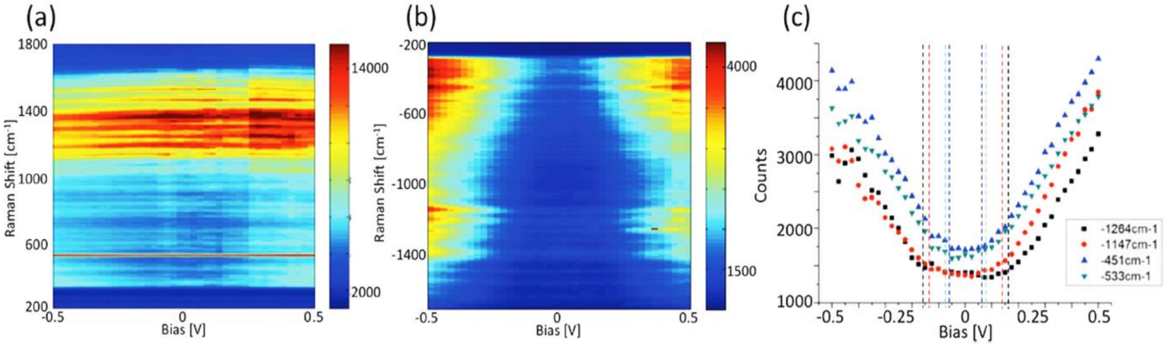

Figure 2-13 Bias driven heating in a C_{60} contain junction. Reprinted from ref[107] (a) Stokes Raman spectra as function of source-drain bias. (b) simultaneous aquired anti-Stokes spectra. (c) The raw counts of particular antistokes peaks as a function of bias.Vertical dashed lines color coded to the particular vibrational modes indicate the threshold $eV=\hbar(\delta\omega)$. Data was aquired at 80K with 3 second integration times at each bias voltage.

2.6 Summary

In this chapter, we combined both optical and electrical measurements to characterize single molecule junction. We attempted three terminal transport measurements on the C_{60} junctions. A few devices showed the Coulomb blockade features when the transport measurements were conducted at 10K in dark It turns out it’s very challenging to get the single molecule in metal nanojunctions in both gateable and optical steady state.

We studied the polarization dependence in the nanogap structures. In those SERS experiments, hybridization of dark multipolar plasmon modes with transverse bright modes produced extremely robust, high field enhancement for localized surface plasmons at the nanogaps. The resulting modes had spectral positions largely determined by the transverse bright components. Those observations lead to the choice of nanogap geometries in Chapter 5.

We also showed the simultaneous Raman and transport measurement can probe the interaction between molecules of interests and metal leads. By varying the voltage applied on the metal junction, we observed noticeable evolutions of the SERS continuum background and the vibrational mode positions as function of bias, which contain rich information of energy dissipation. Those observations motivate the systematic studies of the changes of vibrational properties of C_{60} and its derivative PCBM in nanojunctions applied with external bias in the following chapters.

Chapter 3

Voltage tuning of vibrational modes of C_{60} junctions

This chapter is based largely on ref[49].

Vibrational modes of molecules are fundamental properties determined by intramolecular bonding, atomic masses, and molecular geometry, and often serve as important channels for dissipation in nanoscale processes. Although single-molecule junctions have been employed to manipulate electronic structure and related functional properties of molecules, electrical control of vibrational mode energies has remained elusive.

We use simultaneous transport and surface-enhanced Raman spectroscopy measurements to demonstrate large, reversible, voltage-driven shifts of vibrational mode energies of C_{60} molecules in gold junctions. C_{60} mode energies are found to vary approximately quadratically with bias, but in a manner inconsistent with a simple vibrational Stark effect. The theoretical model from collaborators suggests instead that the mode shifts are a signature of bias-driven addition of electronic charge to the molecule. These results imply that voltage-controlled tuning of vibrational modes is a general phenomenon at metal-molecule interfaces and is a means of achieving significant shifts in vibrational energies relative to a pure Stark effect.

3.1 Introduction

Mechanical couplings between atoms within molecules, manifested through vibrational spectra, are critically important in many processes at the nanoscale, from energy dissipation to chemical reactions. These couplings originate from the self-consistent electronic structure and ionic positions within the molecule.[108] Vibrational spectroscopy examines this bonding, and advanced time-resolved techniques[109–112]can manipulate vibrational populations. Single-molecule junctions[113,114] have also proven to be valuable tools for examining vibrational physics. Previous work has shown that vibrational frequencies can be altered in mechanical break junctions if the chemical linkage to the moving contacts is sufficient to strain bonds in the molecule[115,116]but has also shown vibrations to be unaffected when the linkage to the contacts is less robust[117]. Controllably altering vibrational energies in the steady state is difficult, however. Electric fields can redistribute the molecular electron density and shift vibrational modes in the vibrational Stark effect[118], enabling spectroscopic probes of local static electric fields in charge double layers[119,120]and bio systems[121–123]. However, other physics may also be relevant, and studies of electrical tuning of molecular vibrational energies in single- or few-molecule-based solid-state junctions, which often provide clarity that is difficult to obtain from measurements of molecular ensembles, have been lacking.

Surface-enhanced Raman spectroscopy (SERS)[124,125]in which surface plasmons enhance the Raman scattering rate for molecules, opens up the possibility of performing detailed vibrational studies at the single-molecule level. Plasmonic junctions between extended electrodes[126–132]show correlations of Raman response and conductance implying single or few molecule sensitivity, and enable studies of vibrational physics as a function of electrical bias. Spectral diffusion is often observed in single-molecule SERS experiments[125,132,133], and there is some preliminary evidence of bias-driven mode shifts in such junctions[130], with the mechanisms of these phenomena remaining unclear.

We report vibrational mode softening in C_{60} molecules on the order of tens of wavenumbers, approximately quadratic in the external DC bias, V, applied across such a junction. We compare these observations with density functional theory (DFT) calculations to determine the underlying mechanism. The calculations suggest that the systematic softening, its magnitude, and its detailed functional dependence on V are inconsistent with a pure vibrational Stark effect. Instead, changes in molecular charge with bias[134]result in vibrational shifts that closely resemble those observed in the experiments, both in magnitude and sign. This reveals a general physical mechanism, expected to have implications for other systems and measurements.

3.2 Experimental Setup

Figure 3-1 shows a typical Raman spectrum from a C_{60}-containing junction, prepared by electromigration[135]of a lithographically defined Au constriction on an oxidized Si substrate. This junction is a useful test system, because C_{60} is known to adsorb sufficiently strongly to Au to allow the formation of reliable and reproducible junctions[136–138]. The incident wavelength for the Raman measurements is 785 nm, and the extended electrode design allows the application of a DC bias, V, across the junction and the flow of current through it. The sharp mode at 520 cm^{-1} is from the Si substrate, and the modes between 1000 cm^{-1} and 1600 cm^{-1} are broadly consistent with expectations from previous C_{60} single molecule SERS experiments and with our own calculations. We note that the close association of the molecule with the surface, necessary for SERS measurements, may result in chemical and symmetry changes that can turn previously Raman-inactive normal modes into active ones[139].Because each of our devices produces a unique Au junction possessing a specific molecular association, we track all normal modes of the molecules in the calculations. For the isolated C_{60} molecule, only the Ag and Hg modes are Raman active. They are labeled in Figures 3-4(D).

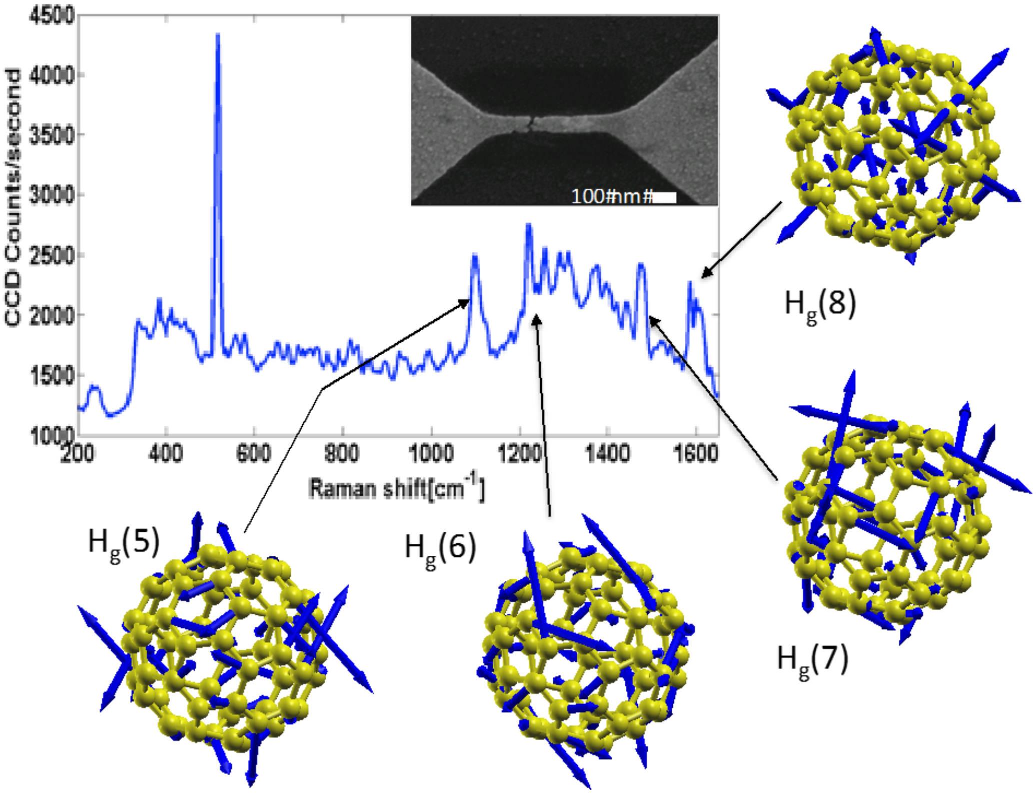

Figure 3-1 Raman analysis of C_{60} in an electromigrated junction. (Main Plot) Example of a SERS spectrum of C_{60} in an electromigrated junction. Surrounding diagrams illustrate examples of the complicated displacements associated with Raman-active modes, calculated for an isolated, symmetric, gas-phase molecule. Each such mode is fivefold degenerate in the absence of symmetry breaking. (Inset) SEM image of an electromigrated junction.

3.3 General device description

As in previous studies[127,128,130,132,140], correlations as a function of time are observed between spectral intensity fluctuations ("blinking") and the measured conductance in the tunneling regime. Since the tunneling conductance is dominated by a molecular-scale volume at the point of closest interelectrode separation, these correlations imply few- or single-molecule Raman sensitivity. For this study, the conductances range from 0.1 to a few $G_0 = 2e^2/h$, and include contributions from both through-molecule tunneling and direct metal-metal tunneling or contact in some junctions. These junctions are not in the Coulomb blockade regime.

3.4 Experimental observation

Figure 3-2 shows Stokes and anti-Stokes spectra as a function of applied bias for two representative devices. The main experimental observation is that many of the vibrational modes with energies greater than 1000 cm^{-1} shift toward low energies as the applied bias increases. These systematic shifts are routinely observed in C_{60}-based junctions, having been seen in 12 out of 23 junctions that produced a significant and stable SERS signal. The remaining 11 junctions had “blinking” (junction configuration instability) sufficiently strong that it precluded the long measurements required for a clear assessment of bias-driven effects. This yield and variation is consistent with prior experiments in such junctions.

The bias-driven shifts, apparent as a curvature of the spectral features, vary in magnitude, from a few cm^{-1} to 20 cm^{-1}. Figure 3-3 shows data from another device, employing a higher resolution grating in the spectrometer. This particular data set shows clear discontinuities in the mode intensities at a few bias voltages; these are stochastic blinking as described above. The bias-driven shifts on the devices are consistent with a quadratic dependence on applied bias, $\delta\omega \sim V^2$. Note that electromigrated junction experiments do not precisely control the molecule/metal contact geometry at the atomic scale; variability in the contact geometry and molecular environment can give junction-to-junction variations in the precise Raman spectrum. However, the sign, functional form, and magnitude of the bias-driven shifts here are consistent and reproducible.

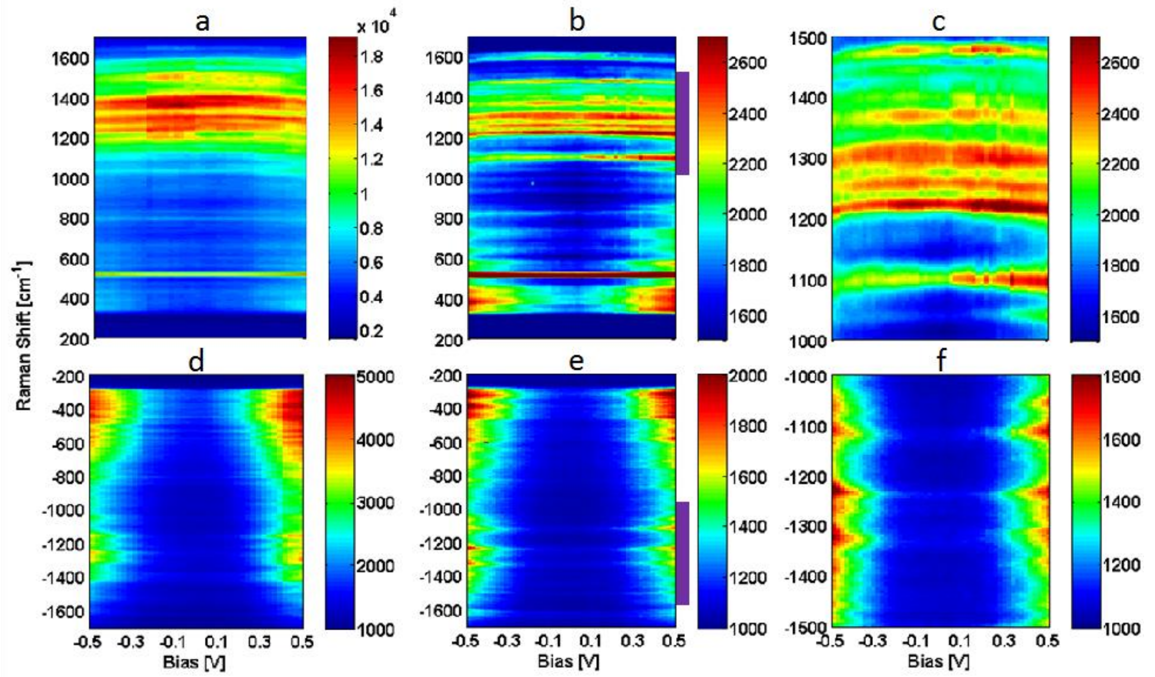

Figure 3-2 Vibrational modes and their evolution with source-drain bias. (a) Stokes and (d) anti-Stokes spectra of device 1 as a function of V. (b) Stokes and (e) anti-Stokes spectra of device 2. Color scales indicate counts per integration time. (c and f) Rescaled close-ups of the device 2 data over the wavenumber ranges indicated by the purple bars in (b) and (e) respectively. The vibrational modes curve slightly toward lower energies at larger |V|, and the anti-Stokes intensities increase at high biases. The latter effect indicates current-driven heating of vibrational degrees of freedom, as reported previously [99,141]. The

spectral shifts are more difficult to resolve in the anti-Stokes case because of this evolution of anti-Stokes intensity.

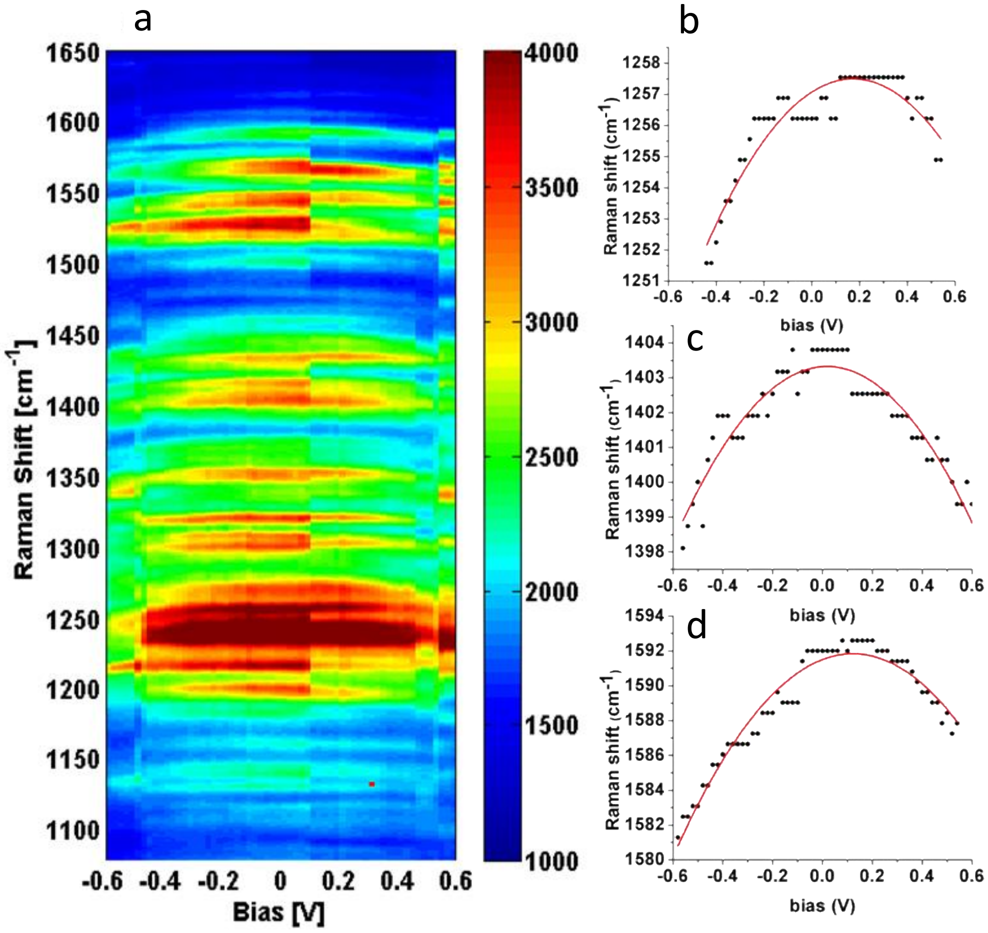

Figure 3-3 Bias-driven vibrational energy shifts. (a) Raman response of device 3 as a function of bias (x axis) and Raman shift (y axis). The sudden change in the intensity at around 0.1 V is the result of blinking. (b–d) Vibrational energy shift as a function of bias for three particular modes: 1258 cm^{-1}, 1404 cm^{-1}, and 1592 cm^{-1}. The discretized Raman shift data result from pixilation of the detector.

3.5 Theoretical calculation

To understand the mechanism at work, we use DFT to compute the vibrational frequencies of C_{60} as a function of external field and charge state. In principle, the local field and charge state of a molecule in a junction depend on atomistic features of the molecule-metal contact which are highly complex, generally unknown, and vary from device to device. Here, we neglect explicit treatment of the electrodes and instead model the C_{60} environment, as a function of bias, through changes in fields and steady-state occupation. Initially, we compute the vibrational frequencies of a gas-phase C_{60} molecule in the presence of constant electric fields. For several external fields up to 1.2 V/nm (approximately twice the range probed by the experiment), the C_{60} geometry is relaxed and the vibrational modes are computed within DFT for constant charge state. Both neutral C_{60} and the C_{60}^{-1} anion are considered. Mirjani et al.[142]recently considered the impact of full reduction or oxidation on vibrational modes of molecules in junctions, observing appreciable shifts relative to the neutral species. However, the lack of resonant transport (see Supporting Information of ref[49]) confirms that the applied bias in this experiment is insufficient to fully change the average redox state of the molecule by an entire electron. Therefore, the anion represents the limit of charging possible in the system. For the neutral C_{60}, our calculations are in good agreement with previous theory and experiment (see SI of ref[49]). Calculated field-induced vibrational shifts for the neutral molecule (anion) are typically far less than 1 cm^{-1} (5 cm^{-1}) in magnitude, at maximum field (1.2 V/nm); moreover, the shifts vary in sign and do not exhibit a generally quadratic functional form with field, in contrast with experiment. This rules out the well-known vibrational Stark effect as the origin of the observed phenomena.

A major clue toward an alternative explanation is that, at constant field, differences between specific mode frequencies of the neutral and anion are large, of order 10-150 cm^{-1}, and notably, the affected anion modes are red-shifted relative to the neutral molecule (see SI in ref[49]). This suggests an explanation in terms of bias-driven changes of the C_{60} charge state. To explore this possibility, we recomputed the C_{60} vibrational spectrum, adding small fractions of an electron, from 0 to 1, in steps of 0.1 e. In the case of significant hybridization between the molecule and metal contact, partially-occupied states in the junction are expected. Furthermore, in an open system a fractional number of electrons in DFT is defined via an ensemble of integer-electron states and interpreted as a time average of a fluctuating number of particles.[143]Therefore, one can infer the effect of partial molecular charging in the junction from calculations of a single partially-charged C_{60} molecule. A fractional occupation of the C_{60} LUMO upon adsorption into a junction is consistent with the established large electronegativity of C_{60} [136,144]and with STM studies of C_{60} adsorbed on clean metal surfaces[145]. As the molecule is (partially) charged, several C_{60} vibrational modes shift systematically to lower energies, by tens of cm^{-1}. We compute that these are Raman-active Hg modes which couple strongly to the t_{1u} LUMO[146–150]and are present throughout the 1000-1600 cm^{-1} measurement range (see Figure 3-4). This trend is reasonable on general chemistry grounds: Adding an electron to the neutral C_{60} occupies an anti-bonding LUMO that is delocalized over the entire molecule, thereby softening many intramolecular bonds. Thus a redshift of vibrational modes coupled to an antibonding LUMO upon electronic charging would be expected quite generally.

Only a relatively small amount of charging is necessary to result in the mode shifts seen here, and small changes in charge state are very plausible under bias. Figure 3-4 shows a simple model for the energy level alignment of the junction. At zero applied bias, the triply degenerate LUMO resonance will be positioned near the Fermi energy[145,151], and broadened by its coupling to the source and drain electrodes. Assuming that electrons tunneling from the source to drain and drain to source, respectively; that they are non-interacting and are therefore occupied according to their original source or drain quasi Fermi levels[152]; and that the resonance lineshape is Lorentzian with a width $\Gamma = \Gamma_S + \Gamma_D$, the change in steady-state occupation, $\delta\rho$ of a single triply degenerate level at energy E_0 above the equilibrium Fermi level EF, at bias V, can be expressed as [108,134]

Equation 3-1

$$\delta\rho = \int_{-\infty}^{\infty} \tfrac{1}{2}\, g(E)\left[f\left(E + \tfrac{eV}{2}\right) + f\left(E - \tfrac{eV}{2}\right) - 2f(E)\right]dE$$

where, in this case, the density of states $g(E) = (d\,\Gamma/\pi)/(\Gamma^2+(E-E_0)^2)$ is Lorentzian with degeneracy d (d = 6 in this case due to spin and orbital degeneracy) and $f(E) = 1/(e^{E/kT} + 1)$ is the Fermi-Dirac distribution function, with the zero-bias Fermi level E_F taken as the energy reference, i.e. $E_F=0$. Here a symmetrical voltage drop is assumed, with the source and drain chemical potentials taken to be μ_S=eV/2 and μ_D=-eV/2, respectively. Recently, Kaasbjerg et al.[153]developed a non-equilibrium Green's function framework for understanding bias-dependent molecular vibrational mode damping and heating in junctions. Including physics similar to what we consider here with our C_{60}-specific model, this approach also captures vibrational frequency renormalization associated with charging and screening[153].

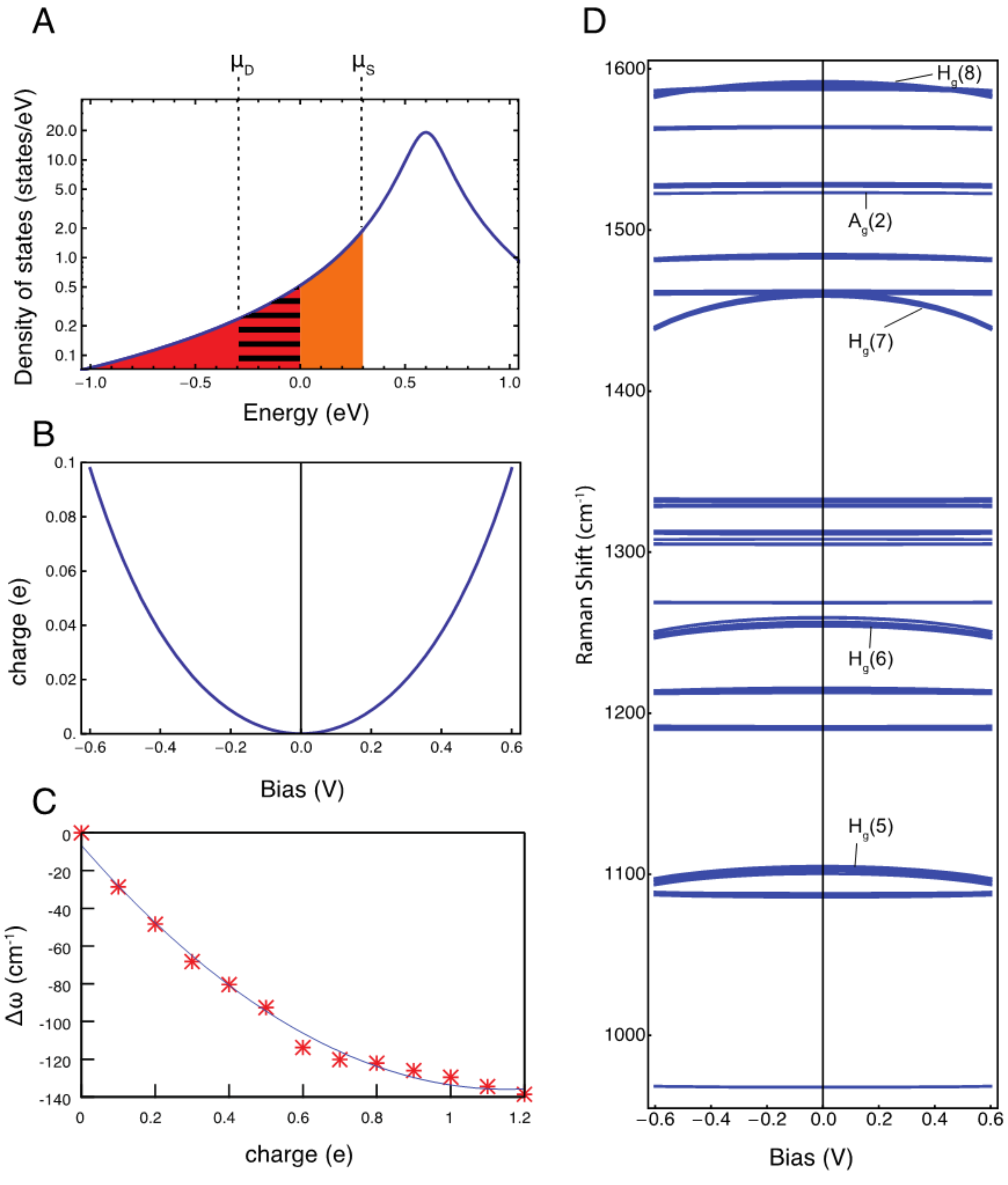

Figure 3-4 Model of bias-driven changes in molecular charging. (A) At zero bias, the triply degenerate LUMO resonance, centered at E_0 with width Γ, is occupied proportionally by the red shading. As the bias V is applied, the molecular level gains additional occupation proportional to the area shown by the orange shading and loses occupation proportional to the hatched portion of the

Lorentzian. (B) The expression for charging with bias at 80 K (solid) is visually identical to the charging at 0 K (for 300-K charging in SI of ref[49]). The change in partial charge is approximately quadratic in bias. (C) A representative mode's [Hg(7) at 1467 cm^{-1}] change in vibrational energy with charging, computed via DFT. This dependence, combined with the variation in charge with bias, strongly suggests that bias-driven charging is the origin of the systematic mode softening observed in the experiments. (D) Mode energies as a function of bias from such a calculation.

Previous STM experiments and DFT calculations of C_{60} on metal surfaces yielded Γ ~ 0.1 eV and E_0 ~1.0 eV[151] . However, in a junction environment, where C_{60} is contacted on both sides with rough surfaces, E_0 will be closer to E_F [145]. Depending on the specifics of the Au-C_{60} contact within a particular junction, E_0 may vary somewhat. The value for Γwill also vary to some degree but numerous experiments have shown significant coupling of C_{60} to Au. To demonstrate our reasoning, we take E0 = 0.6 eV above EF at zero bias and Γ = 0.1 eV (the effect of other choices for these parameters is explored in Figure S8 of the SI in ref[49], but the general effect of charging is preserved). Together with the above model dependence of δρ on V (Figure 3-4 B) and DFT-computed depence of the frequency on δρ (Figure 3-4 C), we compute the vibrational mode frequency as a function of bias for voltages up to +/-0.6 V, as shown in Figure 3-4 D. This simple model explains the measured mode softening trends.

For the choice of model parameters E_0 and Γ, the finite temperature spread of the Fermi-Dirac distribution of the electrons in the source and drain has a negligible effect on the molecular charge at 80 K, but is more important at 300 K. This suggests that any heating of the electronic distribution at high bias[130] could also play a role in determining the molecular charge and hence vibrational energies.

3.6 Conclusions

Using nanojunction-based SERS, we observe systematic bias-driven softening of vibrational modes in C_{60}. Comparisons with DFT calculations show that Stark physics alone cannot be responsible for these effects, and bias-driven alteration of the molecular charge state is the likely explanation. By combining realistic computational models of junctions with measurements of this type, the presence and degree of bias-induced mode softening can turn these junctions into a direct local probe of molecule/metal energetics. Interpreted in light of these observations, the earlier preliminary observations of bias-driven mode softening in a junction based on an oligophenylene vinylene (OPV) molecule[130] suggest that in that particular device the LUMO must lie close to the electrode Fermi levels. Indeed, recent calculations by Kaasbjerg et al. [149]arrive at similar conclusions regarding the origin of OPV mode shifts under bias observed in [130]. Similarly, it is worth considering whether much of the spectral diffusion observed in single-molecule Raman measurements results from small changes in the effective molecular charge density, due to changes in the occupation of proximal surface states or the presence/absence of nearby molecular adsorbates. Finally, the observations reported here point out that considerable care should be taken in the interpretation of vibrational Stark effect data in other contexts.

While good agreement between theoretical expectations and observations has been reported[118] when considering only Stark physics, it is important to note that charging effects can be of similar or greater magnitudes in some circumstances.

Chapter 4

Interplay of bias-driven charging and the vibrational Stark effect in molecular junctions

The majority of this chapter is based on ref[50].

We observe large, reversible, bias driven changes in the vibrational energies of PCBM, based on simultaneous transport and surface-enhanced Raman spectroscopy (SERS) measurements on PCBM-gold junctions. A combination of linear and quadratic shifts in vibrational energies with voltage is analyzed and compared with similar measurements involving C_{60}-gold junctions. A theoretical model based on DFT calculations from the co-authors in ref[50] suggests that both a vibrational Stark effect and bias-induced charging of the junction contribute to the shifts in vibrational energies. In the PCBM case, a linear vibrational Stark effect is observed due to the permanent electric dipole moment of PCBM.

The vibrational Stark shifts shown here for PCBM junctions are comparable to or larger than the charging effects that dominate in C_{60} junctions.

4.1 Introduction

An applied voltage across a molecular junction can influence the mechanical coupling between the constituent atoms both by Stark physics [118](rearrangement of the charge density within the molecule by bias-driven electric fields) and through charge transfer between the molecule and metal electrodes[49]. At the same time, coupling between the electrons and vibrational modes is a critical mechanism for energy transfer in electronic conductors. Probing the relative effects of local electric field and charge state on molecular vibrations therefore lays the groundwork for better understanding of energy dissipation at the nanoscale. Vibrational Stark spectroscopy is one means to investigate the influence of electric field on the dynamics or populations of species undergoing the chemical reactions. Quantitative analysis of the spectral Stark shifts can reveal rich information on variations in the local electric field, and its effect on mutations in biomolecules, conformational changes, and ligand binding[154–157]. The sensitivity of the vibrational transitions to an electric field can also provide a probe into the local electrostatics of an ordered system[158,159].

Previous vibrational Stark effect work has largely focused on analysis of the line-shape evolution of Stark spectra for large ensembles of molecules[160,161]. Methods that provide averaged information may not be sufficient to study surface chemical reactions, because often molecules adsorbed at specific interfacial sites govern surface reactivity.

Surface enhanced Raman spectroscopy (SERS)[32,162] with single-molecule sensitivity[107,163,164] can be utilized to probe the interfacial electric field in diffuse layers[159] and to study the potential-dependent vibrational frequencies of adsorbates on a variety of transition metal surfaces[165]. The vibrational Stark effect was previously utilized as a measurement tool to infer the plasmonic field enhancement in metallic nanostructures[166–169] ; complementary studies, where an applied field is instead used to examine chemical bonding and electrostatic field effects on vibrational modes at the single molecule level, would be of interest and remain challenging. Molecular-scale junctions have proven to be valuable tools for studying vibrational physics[72,75]; as SERS hotspots under conditions of electronic bias they are an enabling technology[5,170] for such studies.

In this chapter, we report the voltage bias-driven vibrational energy shifts of junctions nominally containing individual PCBM (phenyl-C_{61}-butyric acid methyl ester) or C_{60} molecules, at a substrate temperature of 80 K. Analyzing the bias dependence of the vibrational peak energies, we find that statistically the PCBM-containing junctions have noticeably larger linear-in-bias contributions to the peak shifts, compared with C_{60}-containing junctions. We compare these observations with DFT calculations to evaluate the relative importance of the vibrational Stark effect and bias-driven charging mechanisms. The calculations qualitatively reproduce the systematic differences observed between PCBM and C_{60} junction bias dependences, and suggest that while the dominant quadratic shifts in C_{60} junctions are attributable to charging effects[49], the dominant linear shifts in PCBM junctions have significant contributions from vibrational Stark physics. Quantitative discrepancies between the calculation and measurement are attributed to image charge and related electrode effects, explicitly neglected in the theoretical model.

4.2 Experimental setup

Figure 4-1a shows the experimental design of the combined Raman spectroscopy and electronic transport measurement system. As described previously [5,170], Au electrodes connected by a nanowire constriction 120 nm wide and several hundred nm in length are fabricated using electron beam lithography on an oxidized Si substrate. The resulting bow-tie structures are cleaned via exposure to oxygen plasma and spin-coated at 1800 rpm with 0.1 mM solution of PCBM or C_{60} in toluene. The devices are wire-bonded to a chip carrier for electrical measurement and are placed in a microscope flow cryostat. The substrate is cooled in high vacuum to 80 K. For each device, following electromigration[73] at this temperature, the constriction is broken to form a tunnel junction with a closest inter-electrode separation on the nanometer scale. The nanometer gap supports localized surface plasmon resonances with large electric field enhancements, sufficient for SERS studies of single molecules[4,107,163]. After the molecular junction is prepared by electromigration, AC and DC biases are applied to the metal electrodes through a summing amplifier to measure the differential conductance at each DC bias. The rms AC bias is typically 10 mV or less, while the DC bias ranges from -0.5 V to 0.5 V, limited by the device stability. A simultaneous Raman measurement is performed using a home-built Raman microscope with a 785 nm diode laser illumination source. Figure 4-1b shows the Raman spectrum of a typical device. As described in previous chapters, mapping of this Si emission is used to locate the center of the junction. Other peaks shown are believed to be PCBM vibrations. We observe a larger number of PCBM vibrational modes than previously reported [171,172]. One possible explanation for this and similar observations in C_{60} containing junctions[49] is that adsorption in the junction results in a polarizability tensor of lower symmetry than that of the isolated molecule, as the presence of the electrode and nature of the molecule-electrode interaction lifts mode degeneracies and alters selection rules. Multiple molecules in the SERS hotspot is another possibility, though the observation that changes in Raman emission correlate with changes in the (extremely spatially localized[173]) inter-electrode tunneling conductance limits this possibility[174]. Another explanation for the proliferation of modes could be chemical damage due to direct, catalytic, or hot electron photochemistry at the metal interface. Further investigations are ongoing.

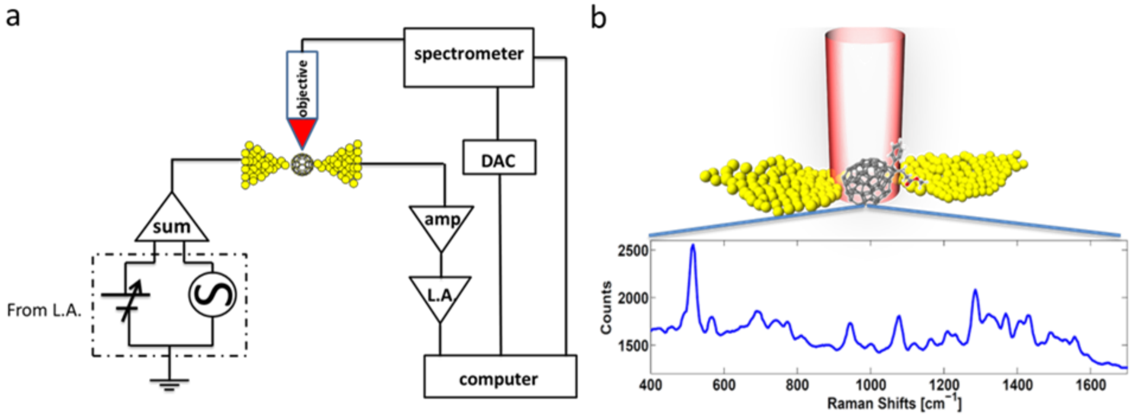

Figure 4-1 (a) Diagram of the Raman measurement setup. (b) Raman spectra of PCBM in an electromigrated junction.

4.3 Comparison between PCBM and C_{60}

Figure 4-2a shows the Stokes spectra as a function of applied bias for a typical PCBM containing junction. Note that a “blinking” event occurs at 0 V and another at ~ 0.3 V, as evident by the intensity changes of the spectrum. These are likely due to a stochastic configuration change such as reorientation of the molecule with respect to the metal electrodes. For each individual spectrum the peak positions are determined using an automated procedure, and results are shown in Figure 4-2b. The dominant peaks that display continuous evolution of the mode position with respect to the bias are highlighted in pink. Each vibrational mode has a unique shift as a function of DC bias voltage. Some peak positions do not shift discernably with applied bias, while others increase or decrease by as much as 20 cm^{-1} across the bias window. The energy shifts are fitted to a quadratic function,

Equation 4-1

$$\nu=\nu_0+p_1V+p_2V^2.$$

Here V is the applied DC bias, and p_1 and p_2 are fitting coefficients. For all curves highlighted in Figure 4-2b, the $|p_2 \times V_{\mathrm{max}}|$ is found to be significantly smaller in magnitude than p_1, implying that the dominant bias-driven effect is a linear-in-bias shift of the vibrational energy. Figure 4-2c shows p_1 for each vibrational mode highlighted in Figure 4-2b.

Corresponding equivalent measurements of a representative C_{60}-containing junction are shown in Figures 4-2d,e,f. There are noticeable differences in the bias dependence of the vibrational modes as compared to PCBM. of the modes found to shift, the majority shift quadratically in bias. The coefficient of the linear shifts, p_1, in the C_{60} junctions is generally smaller than in the PCBM case. The largest magnitude of p_1 for this C_{60} junction does not exceed 5 cm^{-1}/V. Note that there is some “noise floor” in our ability to determine p_1 through peak tracking. The nonzero values of p_1 in this C_{60} device show the limits on such an analysis due to the resolution of the spectrometer, precision of peak finding, and spectral blinking. The inherent asymmetry of the junction geometry (e.g., slight differences in work function between source and drain electrodes due to crystallographic asymmetries) can in principle lead to a “built-in” potential at the junction even when the macroscopic applied bias is zero[175]. This would also impose a systematic voltage asymmetry, though this would be expected to affect all peaks equally[49]. Despite the junction-to-junction variation in the Raman spectrum, the sign, the quadratic form, and the magnitude have been consistent over 9 measured PCBM devices; the remaining 7 devices suffer strong stochastic intensity fluctuations and spectral diffusion during the timescale of the measurements, preventing a clear evaluation of the bias-driven shifts in those junctions. As analyzed in previous work[49], the quadratic bias dependence of the C_{60} junctions is believed to originate not from Stark physics, but from the effect of voltage on charge transfer[176,177] between the Au electrodes and the C_{60}, together with the dependence of vibrational frequencies on the effective occupation of antibonding molecular orbitals.

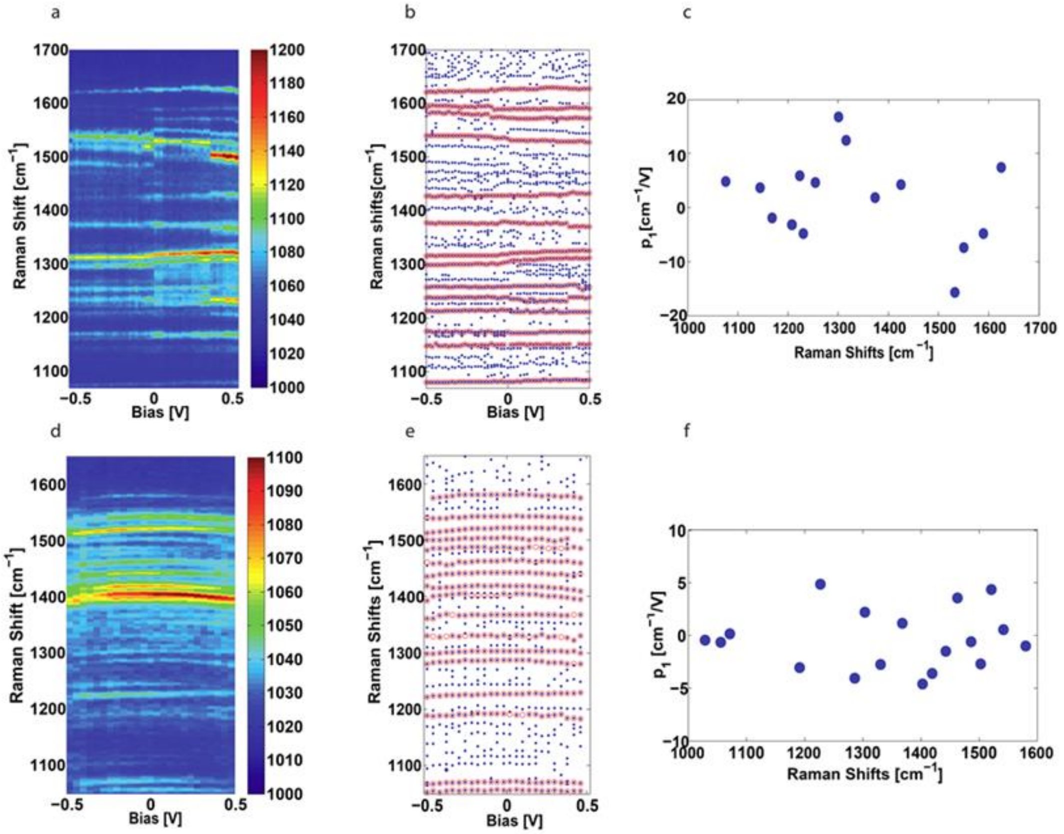

Figure 4-2 Evolution of vibrational modes with applied bias. (a) Stokes Raman emission of PCBM in a typical electromigrated junction as a function of bias. An automated peak-finding routine generates a map of the evolution of the peak positions of dominant modes in (a), highlighted in pink. (c) Linear bias-dependent tuning rates of each highlighted mode are extracted from fitting the peak position to applied potential according to equation 4-1. (d) to (f) Corresponding analogous data sets measured on a typical C_{60}-containing junction.

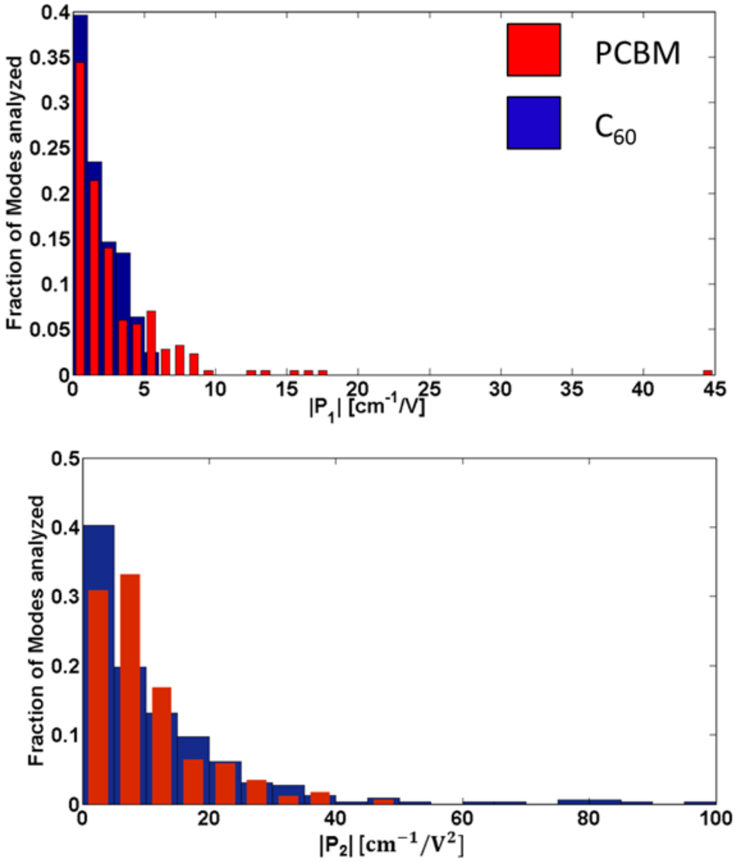

Figure 4-3 Statistical analysis of first order and second order vibrational shifts of PCBM and C_{60}. 9 C_{60}-containing junctions and 9 PCBM-containing junctions which showed the bias dependence are analyzed. Each junction typically exhibited 20 to 30 modes clearly identified through peak-tracking for analysis according to Equation. 4-1. Top and bottom panels: normalized histogram of $|p_1|$ and $|p_2|$ distribution, respectively. PCBM data are plotted in red, narrow columns and C_{60} data in blue, wide columns.

The extracted distributions of $|p_1|$ and $|p_2|$ coefficients of modes tracked in the stable PCBM and C_{60} junctions are presented as normalized histograms in Figure 4-3. For both types of junctions, p_1 is smaller than 2 cm^{-1}/V for more than half of the modes. Because of stochastic intensity fluctuations, spectral diffusion, and systematics associated with the peak identification and tracking, this represents essentially the lower bound of our ability to identify linear bias dependences of mode energies. We also note that inherent asymmetries in the junction would systematically shift the "zero" of voltage and would cause the fitting procedure of Equation. 4-1 to find some small linear shift even in the absence of other physics. For C_{60} junctions, the percentage of modes with larger linear shifts decreases rapidly and the distribution cuts off at p_1=6 cm^{-1}/V. In contrast, for PCBM junctions, the p_1 distribution extends much further, to about 20 cm^{-1}/V, with one extreme case of $p_1 \approx 42$ cm^{-1}/V. The comparatively broad distribution of p_1 values of PCBM junctions suggests different mechanisms that are less relevant to C_{60} junctions. We note that this systematic difference between C_{60} and PCBM-containing junctions in the magnitude of linear bias dependences of mode energies is something that the human eye picks out relatively readily from the color plots like Figure 4-2a, even without formal quantitative peak-tracking analysis.

The distribution of p_2 represents the second order vibrational shifts observed as a function of applied potential. For C_{60}, DFT calculations[49] based on imposing an external DC electric field on the molecule in vacuum have shown that shifts caused by the vibrational Stark effect are not systematically quadratic in bias, nor do they favor mode softening. In that work, bias-driven charging of C_{60} in the junction was found to give rise to quadratic-in-bias mode softening of a magnitude comparable to that observed in the experiments. Similar mode softening is observed here, via negative values of p_2. For over 60 percent of the modes for both C_{60} and PCBM, p_2 is less than 10 cm^{-1}/V^2, with the distribution decreasing as p_2 increases. The p_2 distribution of C_{60} is comparatively extended above 20 cm^{-1}/V^2 and the tail of the distribution goes up to about 100 cm^{-1}/V^2. This is consistent with charge transfer having a dominant influence on the second order vibrational energy shifts of C_{60}. For PCBM, the distribution cuts off at 50 cm^{-1}/V^2. The bias-driven charging model predicts greater shifts as the energy difference, E_0, between the lowest unoccupied molecular orbital (LUMO) and the Au Fermi level is decreased. The difference in p_2 distribution between PCBM and C_{60} may indicate a species-specific difference in molecular level alignment and/or a different coupling between the molecule and electrodes.

4.4 Theoretical calculation

To understand the so-far unique linear-in-bias Raman shift behavior of PCBM junctions, our co-authers of ref[50] use DFT to compute the vibrational frequencies of PCBM as a function of both external electric field and partial charge. As discussed above, prior work on C_{60} junctions has shown that bias-driven changes of the C_{60} charge state can lead to significant negative shifts in vibrational mode frequencies but with no significant linear dependence of the shift on bias. PCBM, despite being a fullerene derivative, is quite asymmetric, and because of the presence of a permanent dipole moment and large polarizability we would expect a significant linear vibrational Stark effect with bias, in addition to any charging effects. To explore this quantitatively for PCBM junctions, we neglect explicit treatment of the electrodes and instead model the PCBM junction as a function of bias with a gas-phase PCBM molecule in an external electric field, with steady-state charge derived from a single-level Lorentzian model and assuming coherent tunneling, as was done previously[49] for C_{60}. We then fit the calculated bias dependence of the mode energies to predict the parameters p_1 and p_2 for each mode.

Importantly, experimental electron affinities (EA) for gas-phase PCBM and C_{60} are quite similar: 2.63 eV and 2.68 eV, respectively[178]. This agrees well with our extended basis set DFT calculations, which yielded EAs of 2.8 eV and 2.9 eV, respectively. [1]. Furthermore, in both molecules the LUMO interacting with the Fermi level electrons of the Au contact has a very similar character in extent and symmetry. Therefore, if the PCBM "tail" does not interfere with bonding it is reasonable to expect the Au Fermi level to LUMO energy difference, E_0, and the Lorentzian broadening, Γ, for both molecules to be quite similar. Therefore we use the same values - E_0 =0.8 eV and Γ=0.10 eV – for both molecules. This case would lead to approximately maximal charge transfer (smallest E_0 and largest Γ) for PCBM.

---

[1] Importantly, standard basis set calculations resulted in *much* lower electron affinity values, of 1.53 eV and 1.51 eV for PCBM and C_{60}, respectively. However, sampling of a variety of field and charge conditions showed that extended and standard basis sets produce similar results for the vibrational shifts. Therefore the results shown here were all computed with standard basis sets – see the SI of ref[50] for more details

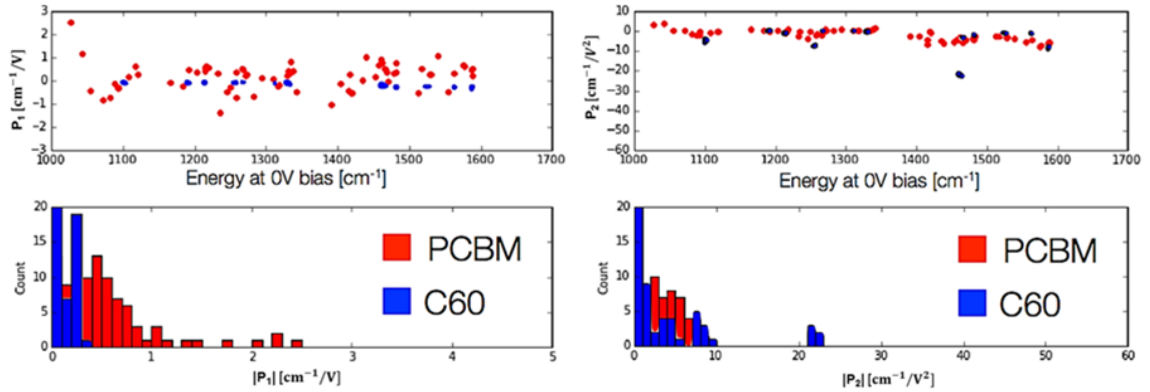

Figure 4-4 Fits to the expression $\nu=\nu_0+p_1V+p_2V^2$ for data computed with our theoretical model, including bias-induced charging and field. (a) Top plot: p_1, the linear fit coefficient of shift with respect to the zero bias normal mode energy. Bottom plot: a histogram of the absolute values of all shifts, obtained with 0.1 cm^{-1}/V binning. (b) Top plot: p_2, the quadratic fit coefficient of shift with respect to the zero bias normal mode energy. Bottom plot: a histogram of the absolute values of all shifts, obtained with 1 cm^{-1}/V binning.

In Figure 4-4, we plot the calculated p_1 and p_2 values derived from our model for each mode for both C_{60} and PCBM.[2] For the above model parameters the calculated bias-induced vibrational shifts for PCBM, including both field and charging effects, show linear

---

[2] Importantly, the calculated vibrational spectrum for gas-phase PCBM is in good agreement with prior work. For example, for prominent modes such as the primary C-H_2/C-O peak and C=O stretch found at 1163 cm^{-1} and 1745 cm^{-1}, respectively, our calculations agree well with previous calculations[179] (1152 cm^{-1} and 1732 cm^{-1}) and experiments[180,181] (1187 and 1738, 1740 cm^{-1}).]

components of up to ∼ 2 cm^{-1}/V and quadratic elements of up to ∼7 cm^{-1}/V^2 in magnitude, at maximum field (1.4 V/nm). In contrast, for our calculations of C_{60} using the same parameters, linear shifts with bias show a maximum of ∼0.4 cm^{-1}/V and quadratic shifts of up to 20 cm^{-1}/V^2.

To lowest order, the linear term in the vibrational Stark effect is known to originate with the second derivative of the induced dipole moment with mode displacement[182], which will only be nonzero for IR active (or polar) vibrational modes. As PCBM lacks inversion symmetry, it features more IR active modes than centrosymmetric C_{60}; this is consistent with the greater linear shifts (and p_1 values) exhibited by PCBM modes. Future atomistic treatment of both molecules beyond the gas-phase including electrodes would be desirable to further explore the role of the electrodes, the bias (and associated electric field), and charging in more detail.

Binned in analogous fashion, our calculations for each mode of both p_1 and p_2 are strikingly consistent with the statistical trends in Figure 4-3, though the calculated magnitudes are smaller than the experimental values, by factors of ∼ 10 and 4, respectively. While small changes in E_0 and Γ can bring the calculated p_2 values for the C_{60} junctions into better quantitative agreement with the experiments, we find that no such adjustments can significantly increase the calculated PCBM p_1 coefficient, even allowing model parameters that lead to more complex bias dependences (*e.g.*, small values of E_0/Γ such that the metal Fermi level approaches resonance with the LUMO Lorentzian).

Although successful qualitatively, our model necessarily misses some essential physics of the real device structures that could magnify the impact of the PCBM linear-in-bias response. For example, by not treating the full junction environment, including the metal electrodes and their static and dynamic screening[183], the present calculation explicitly neglects, e.g., image charge physics. A classical "toy model" of a particle harmonically bound to a conducting surface that incorporates image charge effects will show, over some range of parameters, an approximately linear-in-bias shift of vibrational frequency (see SI of ref[50]). Further investigations, including more sophisticated calculations that include static and dynamic screening effects in realistic junction geometries, should constrain this possibility.

Chapter 5

Surface Enhanced Infrared Absorption using self-aligned nanogap structures

This chapter is based largely on a forthcoming paper.

Plasmonic nanostructures are often used in SEIRA spectroscopy to probe surface assembled molecules or the dielectric environment surrounding the metallic nanostructures. Here we fabricate metallic nanogap structures using self-aligned techniques on an intrinsic silicon substrate and compare resulting SEIRA spectra dependent on the choice of electrode geometry. These structures provide a gap size below 10 nm and support strong electric field enhancements. The structures demonstrate their sensitivity through the enhanced absorption signature of the Si-O stretch in the nearby native silicon oxide layer of nanometer thickness. Simulations reveal this thin layer plays a critical role in determining the plasmon modes of the nanostructures. Numerical simulations of the optical properties are consistent with the observations, highlighting the enhanced electromagnetic fields in the underlying oxide.

5.1 Introduction

Infrared vibrational spectroscopy provides important information about the composition, structure and orientation of the chemical species. However, it is challenging to study a small number of molecules using infrared vibrational spectroscopy due to the comparatively small absorption and Raman cross sections of non-resonantly excited molecules. However, as mentioned previously, noble metal nanostructures with small gaps can support localized plasmon resonances that may be driven optically, effectively concentrating light in a deep subwavelength region, enabling new “surface-enhanced” spectroscopic studies. As is well known, SERS relies critically on this plasmonic field enhancement[4,32,49,50,107,184,185]. Exciting the nanostructure plasmon modes can greatly enhance E in the near-field, increasing Raman emission by orders of magnitude, and hence the sensitivity for the SERS detection of chemical species to single molecule level[162]. Infrared absorption spectroscopy is an important complementary analytical technique to Raman spectroscopy. Plasmon resonances can be designed to fall into the infrared regime and can therefore be utilized for SEIRA spectroscopy.

To achieve this goal, various geometries of plasmonic devices such as rough metal surfaces[186], metallic islands[187], nanorods[188–190], antennas[191], rings[192], cavities[193,194] have been engineered to provide enhanced local field for the study of surface assembled molecules.

Coupled nanogap structures take advantage of highly localized gap plasmon modes and can possess an ideal geometry for maximizing the field intensity for detecting vibrational features of the surrounding molecules. As shown in previous studies[194], metallic nanostructures with gaps in the sub 10 nm regime are highly desirable to provide the maximized field intensity, to overcome the limitation of small infrared absorption cross section of molecules. There have been various methods such as electron beam lithography (EBL)[191], focused ion beam(FIB)[195] etching, and nanosphere lithography, to fabricate the nanogap structures, aiming at achieving sub 10 nm gaps[196]. Reproducibly fabricating plasmonically active sub-10 nm gap structures remains a challenge in infrared spectroscopy.

In this chapter, we compare infrared absorption properties of metal nanostructures with nanometer sized gaps created using self-aligned techniques. The self-aligned methods provide a controllable means of mass production of nanostructures with sub-10 nm gaps. Previous studies proved that the self-aligned nanogap structures support great field enhancement for SERS detection at single-molecule level, and that the presence of particular plasmonic modes leads to an unusual polarization dependence[4,102,107]. As discussed in Chapter 2, in those SERS experiments, hybridization of dark multipolar plasmon modes with transverse bright modes produced extremely robust, high field enhancement for localized surface plasmons at the nanogaps. The resulting modes had spectral positions largely determined by the transverse bright components, which could be controlled well by e-beam patterning, and not very spectrally sensitive to the precise nanogap size. The choice of nanogap geometries in this chapter is driven by these observations, to see if a similar dark-bright hybridization approach could give SEIRA structures, with the nanogap advantage of large enhancements and the hybrid approach advantage of spectral insensitivity to nm-scale nanogap details.

Here we demonstrate that self-aligned gold nanogap structures have sufficient SEIRA sensitivity to provide direct information about the local dielectric environment in the nm scale. Through the infrared extinction of these structures as measured with Fourier transform infrared spectroscopy (FTIR), we were able to detect the local native silicon oxide layer in close vicinity of the nanostructures. We compared the intensity of the Si-O vibrational spectral feature between arrays of rods and two configurations of nanogap structures. Simulations using finite difference time domain (FDTD) methods were conducted to calculate the absorption and the enhanced near field data of the nanorods and self-aligned nanogap structures, and to confirm the particular plasmon resonances of relevance in the various structures.

5.2 Experimental methods

The metal nanostructures for the SEIRA investigations were fabricated on a 500 micron-thick intrinsic silicon substrate with resistivity of 10,000 ohm -cm. For a comparative reference, arrays of *individual* nanorod resonators were patterned using e-beam lithography and liftoff processing. The rod metallization was 1 nm Ti (adhesion layer) followed by 20 nm of Au. Arrays of rods with long axes defining the *x* direction were prepared with rod lengths between 800 and 1100 nm and rod widths of ~ 70 nm. Within the arrays the rods were separated by 4 μm in *x* and 2 μm in *y*. Two types of self-aligned nanogap structures were created for comparison with the rods: transversely coupled dimers (two rods adjacent to one another separated in *y* by a self-aligned nanogap), and longitudinally coupled dimers (two rods adjacent to one another separated in *x* by a self-aligned nanogap). The fabrication of self-aligned nanogaps[94] involves two steps of e-beam lithography. In the first step one nanorod of a desired length (discussed below) was patterned on the intrinsic silicon wafer via e-beam lithography. After development, metal layers of 1 nm Ti, 20 nm Au and 11 nm Cr were evaporated onto the substrate, followed by liftoff of the remaining resist. The chromium layer oxidizes in air and forms a few-nm chromium oxide layer that acts as a shadow mask for the subsequent steps. In the second step of lithography the other nanorod was patterned overlapping the rod fabricated in the first step. The same set of metal layers was again deposited. Following liftoff, the substrate was then placed in a chromium etchant to remove the overlapping materials as well as the chromium layer, leaving gaps formed between two adjacent rods. The SEM image in Figure 5-1 shows the two typical self-aligned nanogap structures on the Si substrate. The nanogap structures consist of two rods coupled either in the vertical direction or in the longitudinal direction. The gap size is typically within 10 nm.

All optical characterizations were performed using a FTIR microscope (Nicolet continuum) attached to a FTIR spectrometer (Nicolet iS50) and equipped with a mercury cadmium telluride (MCT) detector. Data were acquired at transmission mode in purged air at room temperature. The field of view was set by a 15X objective and a 40×60 μm^2

aperture for spectra acquisition which contains 300 nanorods and 150 dimers in the nanogap structure case. The transmission spectra were acquired with 4 cm^{-1} resolution and averaged over 1200 scans. For spectroscopic measurements with polarized light, a ZnSe polarizer was inserted in the infrared light path. The background measurement was carried on the blank substrate of the same area centered 100 micron away from the devices. To compare the field enhancement, the measurements were conducted on the arrays of nanorod and self-aligned nanogap structures.

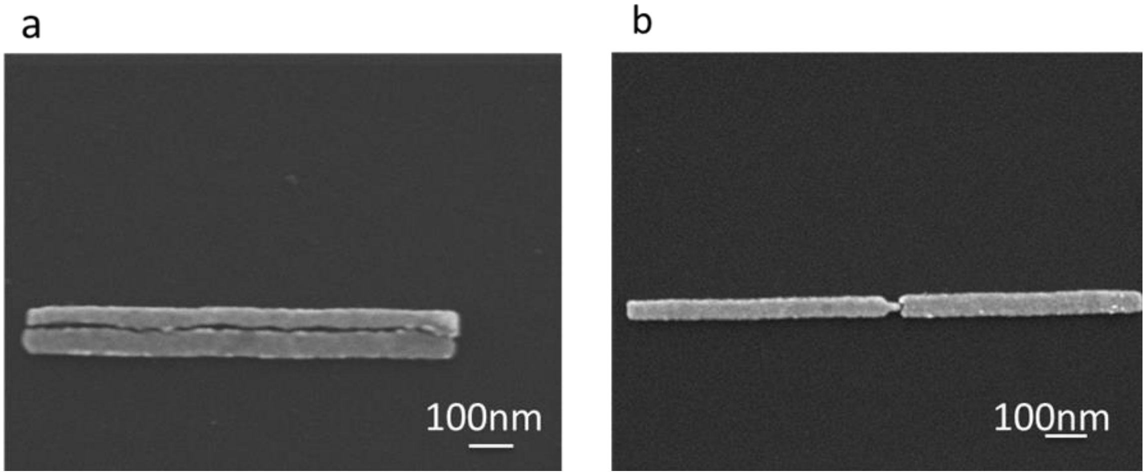

Figure 5-1 SEM images of the two types of self-aligned nanogap structures. (a) Transverse couple self-aligned nanogap structure. Two rods coupled in the vertical direction. The gap is formed between the sides of the rod. (b) Longitudinal coupled self-aligned nanogap structure. Two rods coupled in the horizontal direction. The gap is formed between the ends of the rods.

5.3 Results and Discussion

We first measured the transmission spectra of arrays of the individual nanorods and compared these with FDTD simulation results of a single rod in different dielectric environments. Figure 5-2a shows the transmission spectra of arrays of the nanorods with different lengths and fixed width. The dip in transmission corresponds to extinction due to absorption and scattering associated with the longitudinal plasmon resonance of each rod. The center to center distance between each rod is 4 μm in the *x* direction (parallel to the rod) and 2 μm in the *y* direction (perpendicular to the rod); there is no expectation of collective effects in the extinction as these spacings have no particular commensurability with the resonant wavelength associated with the individual rods. As the rod length increases, the plasmon resonance shifts further toward longer wavelength, and the magnitude of the transmission dip increases as well.

As the plasmon resonance shifts close to 1300 cm^{-1}, a peak emerges at 1250 cm^{-1}, which is the energy of the Si-O vibrational mode. Note that the signature of spectrally narrow infrared absorption taking place alongside the much broader plasmon resonance is a peak in the transmission – this is the result of Fano interference [197]. To compare with the experimental data, simulations were performed using FDTD methods with Lumerical Solutions, as shown in Figure 5-2b. The simulation calculated the absorption of single gold nanorod of length 1 μm in the dielectric environment of 1 nm Ti, 1 nm SiO_2 on top of intrinsic silicon as well as the spatial map of electric field enhancement. The absorption peak around 1300 cm^{-1} and a sharp dip within the absorption peak at around 1250 cm^{-1} are obtained from the simulation results. The consistency between the experimental observation and the simulated results suggests that thin dielectric layer plays a critical role in determining the plasmon resonance of the metal nanostructures located on top of the dielectric layer. The spatial map of the electric field distribution at the energy of the plasmonic resonance maximum, 1443 cm^{-1}, was calculated. This clearly shows that the electric field at the two ends of the nanorod is maximally enhanced, indicating that the dominant contribution to the absorption peak is the longitudinal dipole mode in the nanorod, with the field further locally enhanced by sharp features (the corners of the rod).

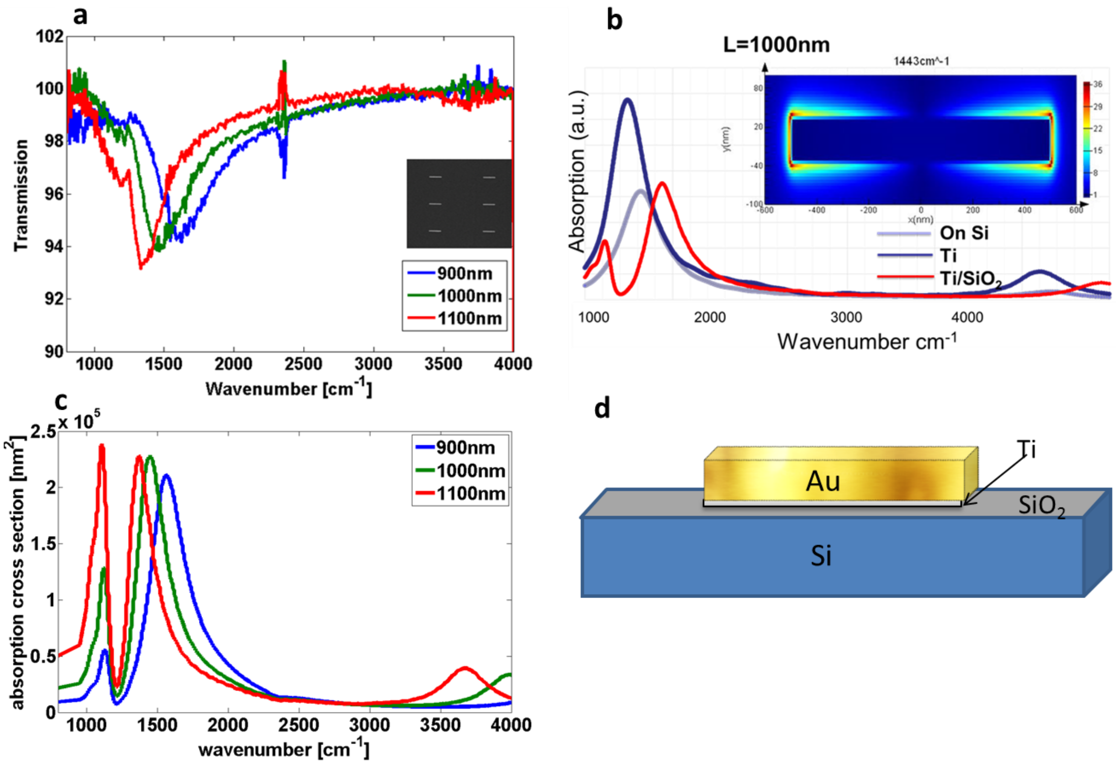

Figure 5-2 Transmission spectra of the single rod and FDTD simulation of the single-rod optical response. (a) Transmission spectra of arrays of nanorods with different length. Longer rods lead to a red-shifting of the longitudinal, dipolar plasmon resonance, while the peak feature near 1250 cm^{-1} is the signature of the infrared absorption of the Si-O stretch in nearby native oxide. (b) Simulations of the absorption of a single 1 μm long rod in different dielectric environments. Inclusion of the 1 nm Ti layer is necessary to match the spectral position of the resonance, and inclusion of the nm-scale native oxide between the rod and the Si substrate leads to the appearance of a Si-O absorption feature in the total absorption spectrum. (c) Absorption cross section calculated using FDTD method. (d) Schematic view of the structure configuration used in the simulation.

To gain insight into the field enhancement in the nanostructures, the FTIR signal intensity of Si-O phonon mode was measured and compared between the three nanostructure architectures: arrays of single nanorods, arrays of transverse-coupled self-aligned nanogap dimers shown in Figure 5-1a, and arrays of longitudinal-coupled self-aligned nanogap structures shown in Figure 5-1b. The motivation for considering the transverse-coupled nanogap dimers stemmed from the unusual plasmon modes that are present in appropriately designed nanogap SERS structures[102]. In those structures, very large, highly local intensity enhancements result from the hybridization between a dipole-active transverse plasmon mode of a metal strip (resonant with a free-space wavelength of 785 nm) and higher order multipolar modes present at a nanogap defined in the strip. This hybridization is possible due to the broken symmetry of the nanogap region. In the present work, the question is whether an analogous effect can take place in transverse-coupled nanowire dimers, with each rod longitudinally resonant with the incident infrared excitation, and the imperfections of the nanogap fabrication process leading to hybridization between those longitudinal resonances and localized multipolar modes within the nanogap. The longitudinal-coupled dimers are a more conventional point of comparison, supporting a localized plasmon resonance at the inter-rod nanogap due to direct hybridization between the longitudinal modes of the individual rods. Longitudinal coupling of nanorods with nanogaps fabricated by direct lithography[191] and by other nanogap fabrication methods[195,196] have already been demonstrated.

The separation of the nanorod dimers within the dimer arrays was set to be 4 μm in both *x* and *y* directions. The same aperture size was set for FTIR measurement in all three cases. Thus, the data comes from a total of 300 nanorods, either in an array of 300 individual rods, or in arrays of 150 dimers. The total amount of Au (and the total number of rod ends, where fields tend to be enhanced for the individual rod resonances) is therefore the same between the different samples. Figure 5-3 shows the experimental data and corresponding baseline corrected spectra (see below). Distorted absorption lineshapes were observed for Si-O stretching mode, which is an evidence of Fano resonance[197–201] due to the coupling between the broad plasmon resonance of the metal nanostructures and the narrow Si-O phonon mode from the underlying silicon dioxide layer. Vibrational absorption features from CO_2 were also observed at 2400 cm^{-1} in the spectral range as either a peak or dip. This inconsistency arises from the background subtraction procedure and fluctuations in the ambient CO_2 concentration during the baseline and data collection scans.

The transmission spectra show that the overall dip of the plasmon mode in the transmission is stronger in the individual nanorod array, confirming that each nanorod acts as an individual source of scattering and absorption. However, we observe a stronger signal intensity of the Si-O stretching mode from the self-aligned nanogap structures than the individual nanorod array in general. This indicates that the integrated local near field intensity giving enhanced IR absorption is stronger in the nanogap structures than in the nanorod arrays. The longitudinal self-aligned gap has the strongest signal among the three different geometries, indicating the field intensity in the gap region is enhanced most when the two components couple in the horizontal direction. Further evidence for the strong coupling in the longitudinal direction is that shorter nanorods are required in this configuration for the plasmon mode to appear at the same spectral position, consistent with a strong redshift in the hybridized coupled-rod plasmon relative to the longitudinal modes of the individual nanorods. Transmission spectra with polarized incident light are shown in Figure 5-3b. The dip in the transmission spectra is maximized when the samples are excited with longitudinally polarized light, confirming that the dipole mode is the major contribution to the plasmonic dip in the transmission spectra. Similar results are observed in the transverse coupled self-aligned nanogap structures. The longitudinal polarization leads to the maximal response in the transverse-coupled dimers as well. This is consistent with the longitudinal rod mode being essential, as in both the individual-rod case and in the hybridized dark plasmon scenario of reference [102]. To get a better sense of the possible importance of such a hybridized mode, we must quantitatively compare the enhanced IR absorption signals.

To isolate the signal intensity of the Si-O phonon mode, the baseline plasmon dip in transmission from the metal nanostructures was modeled numerically (see Figure 5-3c) and subtracted. Gaussian functions were employed for the baseline fit. Figure 5-3c illustrates the fitting procedure: taking the transverse nanogap dimer structure with 1100 nm long nanorods as an example (denoted as SA1100TG), the date from the Si-O spectral region were omitted to form a baseline of the plasmon contribution to the extinction, and this baseline was fit to Gaussians. For comparison, an asymmetric least square method

(AsLS) to model the plasmonic baseline was also applied [194]. The comparison between the two methods is shown in Figure 5-4. The Gaussian approach more closely matches the plasmonic baseline relative to AsLS, though the overall conclusions are unaltered. The baseline resolved Si-O contribution spectra of the nanorod and self-aligned nanogap structures are presented in Figure 5-3d. The results clearly show that the existence of the gap in the nanostructures greatly enhances the signal of the Si-O stretching. Residual vibrational features in the spectral range from 1500 cm^{-1} to 1700 cm^{-1} originate from water bending modes[202] since the measurement was conducted in the open FTIR microscope.

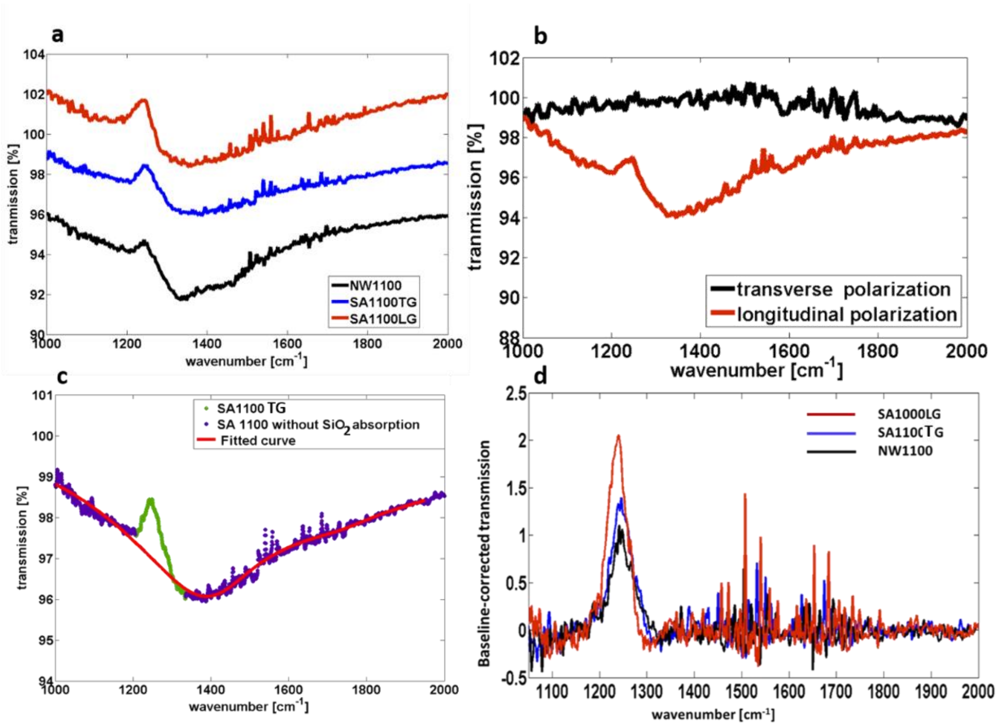

Figure 5-3 Transmission spectra with baseline correction. (a) Transmission spectra of three different nanostructures. Red curve shows the measured transmission from longitudinal coupled self-aligned nanogaps (denoted as

SA1000LG), the blue curve shows the transverse coupled self-aligned nanogaps (denoted as SA1100TG) and the black curve shows the nanorod case (denoted as NW1100). (b) Transmission spectra of the transverse self-aligned nanogap structure at different polarizations. Red curve shows the polarization is along the long axis and the black curve shows transverse polarization. (c) Transmission with baseline subtracted from the experimental curve. Red curve represents the longitudinal self-aligned nanogaps, blue curve represents the transverse (vertical) self-aligned nanogaps and the black curve presents the nanorod case. (d) Transmission spectra of the arrays of vertical self-aligned nanogaps. Green curve is data points of the Si-O phonon mode in transmission mode, purple curve is the remaining part of the data points and the red curve is a curve fit.

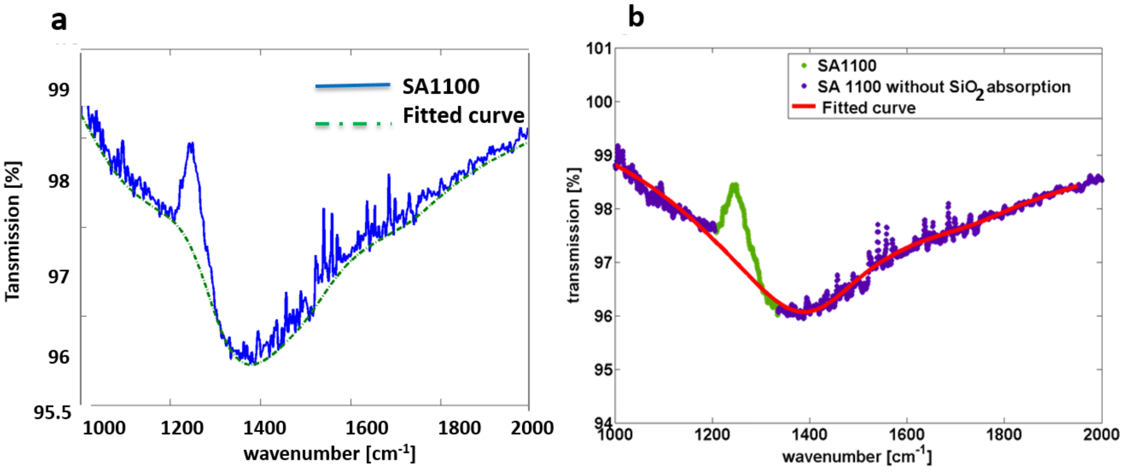

Figure 5-4 Comparison of Baseline fitted using (a)AsLS and (b) Gaussian

To investigate the origin of the enhanced Si-O stretch mode, the spatial electric field distribution is calculated using FDTD by fellow group member Mathieu Simeral. Figure 5-5 shows the transverse self-aligned nanogap for which each rod has a length of 800 nm. The width of each rod is 70 nm and the separation between the rods is 5 nm. The parameters of the dielectric environment are 1 nm Ti on top of 1 nm SiO_2 which in turn sits upon intrinsic silicon. The incoming electromagnetic field is polarized in the x direction with an energy of 1387 cm^{-1}. Figure 5-5b shows the resulting electric field amplitude in the x-y plane. For the transverse nanogap structure the simulations reveal that the maximum field amplitude is located at the ends and corners of the rods indicating the excitation of longitudinal plasmons. The field intensity in the gap is not greatly enhanced. Therefore, the strong signal observed in the experiments for the corresponding geometry is likely to originate from broken symmetry due to the imperfection and rough edges produced from the fabrication process, which are visible in Figure 5-1(a). Figure 5-5d shows the electric field amplitude in the x-z plane. The maximum field is located at the SiO_2 interface and the fields are highly localized, which explains the strong signal observed in the experiments.

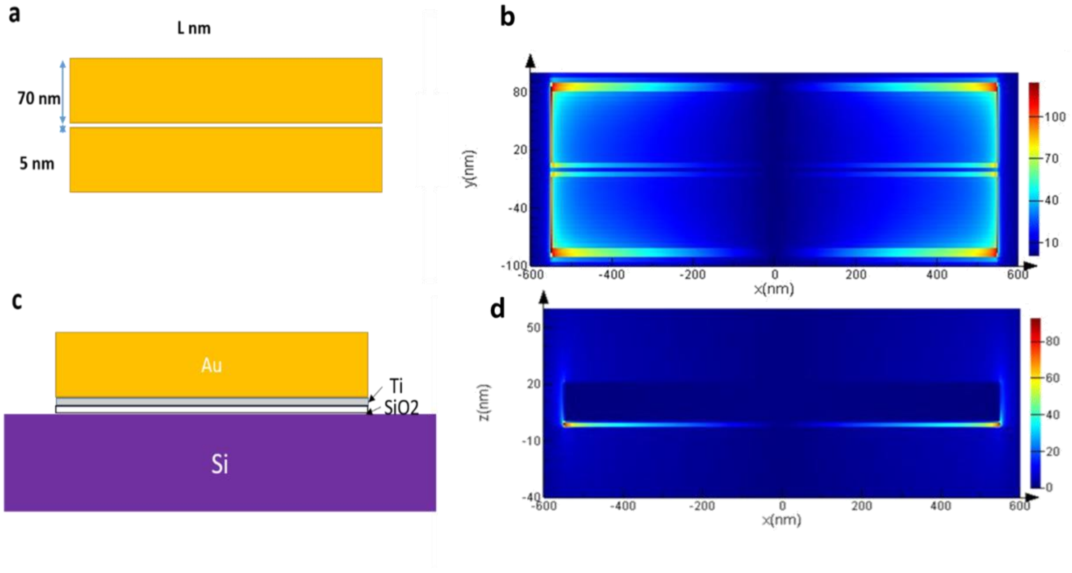

Figure 5-5 Simulations of the local field intensity of the transverse structures using FDTD. Illustration of the geometry of the transverse nanogap structures in the (a) x-y and (c) x-z plane in the simulations. (b) and (d) Calculated electrical field intensity with energy of1387cm^{-1} in x-y and x-z planes.

We also compute the numerically integrated losses in the SiO_2 layers for the three different configurations, and make a quantitative comparison with the data in Fig. 5-3(d). The relative magnitudes of the integrated losses in SiO2 layer for those three structures are consistent with the experimental trend. We are continuing to develop the FDTD simulations to consider different broken symmetry configurations of the transverse-coupled nanorods, to see quantitatively how this affects the field distributions and computed integrated oxide absorption.

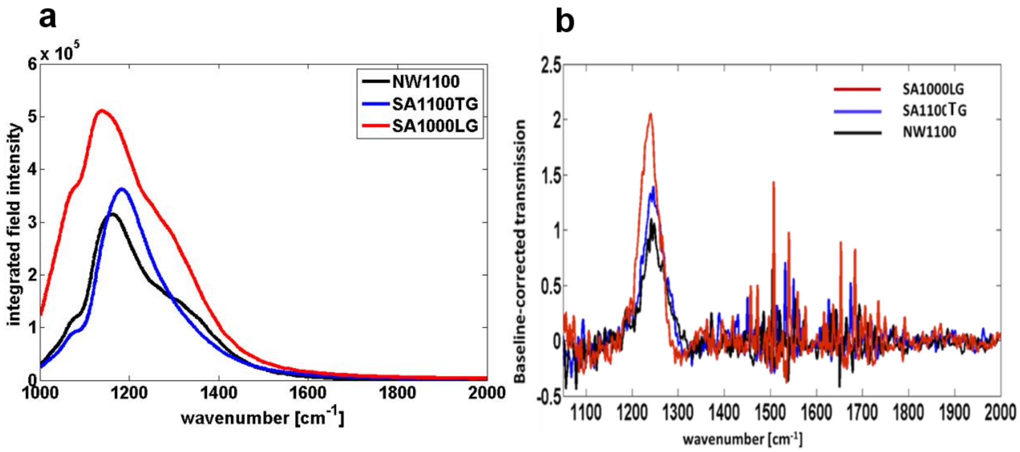

Figure 5-6 (a)Integrated losses in the SiO_2 layer from FDTD simulations. (b) Transmission spectra of the arrays of vertical self-aligned nanogaps,adapted from Figure 5-3(d)

5.4 Conclusion

In summary, we've shown that the nanogap structures with sub 10 nm gaps can support high field enhancements. The dominant plasmon mode in the nanogap structures is the dipolar mode. The presence of the gap enables the strong coupling of the plasmon modes in adjacent rods. The resulting plasmons create an enhancement of the local electromagnetic field. The enhanced field is highly localized at the interface of the SiO_2 layer with the thickness down to 1 nm, which demonstrates the high sensitivity of the nanogap structures as probes of the surrounding dielectric environment.

Chapter 6

Final remarks and future directions

In this thesis optical vibrational spectroscopy and electrical characterization were combined to study the mechanical and electronic properties of single molecules in the nanojunction. The nature of how an external voltage applied on the metal electrodes affects the vibrational states of the molecules was investigated. We discovered voltage-driven shifts of vibrational mode energies of C_{60} molecules in gold junctions. The majority of C_{60} mode energies were found to vary approximately quadratically with bias with a small fraction showing linear bias dependence. The overall trend is inconsistent with a simple vibrational Stark effect. A theoretical model developed by collaborators suggests instead that the mode shifts are a signature of bias-driven addition of electronic charge to the molecule. These results imply that voltage-controlled tuning of vibrational modes is a general phenomenon at metal-molecule interfaces and is a means of achieving significant shifts in vibrational energies relative to a pure Stark effect. To the best of our knowledge, this measurement is the first demonstration of controllably and reversibly softening bonds between atoms by applying a voltage and running an electric current through a single molecule.

With similar measurements involving PCBM-gold junctions, a combination of linear and quadratic shifts in vibrational energies with voltage was observed. A theoretical model based on DFT calculations suggests that both a vibrational Stark effect and bias-induced charging of the junction contribute to the shifts in vibrational energies. In the PCBM case, a linear vibrational Stark effect is observed due to the permanent electric dipole moment of PCBM. The vibrational Stark shifts shown in Chapter 4 for PCBM junctions are comparable to or larger than the charging effects that dominate in C_{60} junctions.

These discoveries show the possibility of using an external electric field to tune the charge of a single molecule and therefore change the mechanical properties of certain molecules. These results may reveal some possible origins of the spectral diffusion as one of the features of single molecule spectroscopy. The shifts of the vibrational modes obtained from the SERS spectrum could also serve as a probe of the local electric fields. Furthermore, an interesting question arises: is it possible to drive certain chemical reactions by adjusting the external electrostatic environment?

We also explored the potential of using self-aligned nanogap structures on an intrinsic silicon substrate as a SEIRA substrate. These structures provide a gap size below 10 nm and support strong electric field enhancements. The structures demonstrate their sensitivity through the enhanced absorption signature of the Si-O stretch in the nearby native silicon oxide layer of nanometer thickness. Simulations reveal this thin layer plays a critical role in determining the plasmon modes of the nanostructures. Numerical simulations of the optical properties are consistent with the observations, highlighting the enhanced electromagnetic fields in the underlying oxide.

The presence of the metal surface can affect the polarizability of molecules in the vicinity of the metal. The positions of the vibrational modes vary from the bulk and certain IR-active modes are present in the Raman process. The selection rules determining which vibrational modes being activated or enhanced is still unclear. The extent of chemical enhancement in revealing these modes remains to be answered.

Heat generation in the nanojunction was also explored. The heat generation can originate from direct light-metal interaction, plasmons decaying into hot electrons, and the interaction mediated from the molecule[203]. It's important to understand and characterize the temperature rise and heat distribution resulting from different mechanisms. The charge tuning and the hot electrons generated in the nanogap show the potential of using the nanojunction to study photoexcited chemistry.

There is plentiful future research in studying the potential of nanostructures for surface enhanced infrared spectroscopy, especially towards the goal of reaching single molecule sensitivity. It's worthwhile to investigate different materials and use novel fabrication techniques to achieve different geometries.

References

1. Reed, M. A., Zhou, C., Muller, C. J., Burgin, T. P. & Tour, J. M. Conductance of a Molecular Junction. *Science* **278,** 252–254 (1997).
2. Tao, N. J. Electron transport in molecular junctions. *Nat Nano* **1,** 173–181 (2006).
3. Lim, D.-K., Jeon, K.-S., Kim, H. M., Nam, J.-M. & Suh, Y. D. Nanogap-engineerable Raman-active nanodumbbells for single-molecule detection. *Nat Mater* **9,** 60–67 (2010).
4. Ward, D. R. *et al.* Electromigrated Nanoscale Gaps for Surface-Enhanced Raman Spectroscopy. *Nano Lett.* **7,** 1396–1400 (2007).
5. Ward, D. R. *et al.* Simultaneous Measurements of Electronic Conduction and Raman Response in Molecular Junctions. *Nano Lett.* **8,** 919–924 (2008).
6. Raman, C. V. A new radiation. *Proc. Indian Acad. Sci.* **37,** 333–341 (1953).
7. Eine neue Erscheinung bei der Lichtzerstreuung in Krystallen. *Naturwissenschaften* **16,** 557–558 (1928).
8. Bethune, D. S. *et al.* Vibrational Raman and infrared spectra of chromatographically separated C60 and C70 fullerene clusters. *Chemical Physics Letters* **179,** 181–186 (1991).
9. Lau, W. S. *Infrared Characterization for Microelectronics*. (World Scientific, 1999).
10. Barth, A. Infrared spectroscopy of proteins. *Biochimica et Biophysica Acta (BBA) - Bioenergetics* **1767,** 1073–1101 (2007).

11. Oxford University Press | Online Resource Centre | Atkins & de Paula: Elements of Physical Chemistry 6e. Available at: http://global.oup.com/uk/orc/chemistry/echem6e/. (Accessed: 27th May 2016)
12. in *Surface Plasmons on Smooth and Rough Surfaces and on Gratings* 4–39 (Springer Berlin Heidelberg, 1988).
13. Ninham, B. W., Powell, C. J. & Swanson, N. Plasmon Damping in Metals. *Phys. Rev.* **145,** 209–217 (1966).
14. Sönnichsen, C. *et al.* Drastic Reduction of Plasmon Damping in Gold Nanorods. *Phys. Rev. Lett.* **88,** 77402 (2002).
15. Lee, K.-C., Lin, S.-J., Lin, C.-H., Tsai, C.-S. & Lu, Y.-J. Size effect of Ag nanoparticles on surface plasmon resonance. *Surface and Coatings Technology* **202,** 5339–5342 (2008).
16. Peng, S., McMahon, J. M., Schatz, G. C., Gray, S. K. & Sun, Y. Reversing the size-dependence of surface plasmon resonances. *PNAS* **107,** 14530–14534 (2010).
17. Link, S. & El-Sayed, M. A. Shape and size dependence of radiative, non-radiative and photothermal properties of gold nanocrystals. *International Reviews in Physical Chemistry* **19,** 409–453 (2000).
18. Wang, H., Brandl, D. W., Le, F., Nordlander, P. & Halas, N. J. Nanorice: A Hybrid Plasmonic Nanostructure. *Nano Lett.* **6,** 827–832 (2006).
19. Fan, J. A. *et al.* Self-Assembled Plasmonic Nanoparticle Clusters. *Science* **328,** 1135–1138 (2010).

20. Westcott, S. L., Oldenburg, S. J., Lee, T. R. & Halas, N. J. Formation and adsorption of clusters of gold nanoparticles onto functionalized silica nanoparticle surfaces. *Langmuir* **14,** 5396–5401 (1998).
21. Naik, G. V., Shalaev, V. M. & Boltasseva, A. Alternative Plasmonic Materials: Beyond Gold and Silver. *Adv. Mater.* **25,** 3264–3294 (2013).
22. Grady, N. K., Halas, N. J. & Nordlander, P. Influence of dielectric function properties on the optical response of plasmon resonant metallic nanoparticles. *Chemical Physics Letters* **399,** 167–171 (2004).
23. Holmgaard, T. & Bozhevolnyi, S. I. Theoretical analysis of dielectric-loaded surface plasmon-polariton waveguides. *Phys. Rev. B* **75,** 245405 (2007).
24. Wiley: Introduction to Solid State Physics, 8th Edition - Charles Kittel. Available at: http://www.wiley.com/WileyCDA/WileyTitle/productCd-EHEP000803.html. (Accessed: 27th May 2016)
25. Benson, O. Assembly of hybrid photonic architectures from nanophotonic constituents. *Nature* **480,** 193–199 (2011).
26. Prodan, E. & Nordlander, P. Plasmon hybridization in spherical nanoparticles. *The Journal of Chemical Physics* **120,** 5444–5454 (2004).
27. Fleischmann, M., Hendra, P. J. & McQuillan, A. J. Raman spectra of pyridine adsorbed at a silver electrode. *Chemical Physics Letters* **26,** 163–166 (1974).
28. Jeanmaire, D. L. & Van Duyne, R. P. Surface raman spectroelectrochemistry. *Journal of Electroanalytical Chemistry and Interfacial Electrochemistry* **84,** 1–20 (1977).

29. Lombardi, J. R., Birke, R. L., Sanchez, L. A., Bernard, I. & Sun, S. C. The effect of molecular structure on voltage induced shifts of charge transfer excitation in surface enhanced Raman scattering. *Chemical Physics Letters* **104,** 240–247 (1984).

30. Osawa, M., Matsuda, N., Yoshii, K. & Uchida, I. Charge transfer resonance Raman process in surface-enhanced Raman scattering from p-aminothiophenol adsorbed on silver: Herzberg-Teller contribution. *J. Phys. Chem.* **98,** 12702–12707 (1994).

31. Kambhampati, P., Child, C. M., Foster, M. C. & Campion, A. On the chemical mechanism of surface enhanced Raman scattering: Experiment and theory. *The Journal of Chemical Physics* **108,** 5013–5026 (1998).

32. Nie, S. & Emory, S. R. Probing Single Molecules and Single Nanoparticles by Surface-Enhanced Raman Scattering. *Science* **275,** 1102–1106 (1997).

33. Kneipp, K. *et al.* Single Molecule Detection Using Surface-Enhanced Raman Scattering (SERS). *Phys. Rev. Lett.* **78,** 1667–1670 (1997).

34. Song, L., Hennink, E. J., Young, I. T. & Tanke, H. J. Photobleaching kinetics of fluorescein in quantitative fluorescence microscopy. *Biophys J* **68,** 2588–2600 (1995).

35. Etchegoin, P. G., Le Ru, E. C. & Meyer, M. Evidence of Natural Isotopic Distribution from Single-Molecule SERS. *J. Am. Chem. Soc.* **131,** 2713–2716 (2009).

36. Dieringer, J. A., Lettan, R. B., Scheidt, K. A. & Van Duyne, R. P. A Frequency Domain Existence Proof of Single-Molecule Surface-Enhanced Raman Spectroscopy. *J. Am. Chem. Soc.* **129,** 16249–16256 (2007).

37. Kleinman, S. L. *et al.* Single-Molecule Surface-Enhanced Raman Spectroscopy of Crystal Violet Isotopologues: Theory and Experiment. *J. Am. Chem. Soc.* **133,** 4115–4122 (2011).

38. Etchegoin, P. G. & Le Ru, E. C. Resolving Single Molecules in Surface-Enhanced Raman Scattering within the Inhomogeneous Broadening of Raman Peaks. *Anal. Chem.* **82,** 2888–2892 (2010).

39. Ren, M. *et al.* Linearly Polarized Light Emission from Quantum Dots with Plasmonic Nanoantenna Arrays. *Nano Lett.* (2015). doi:10.1021/nl5047973

40. Efros, A. L. & Rosen, M. Random Telegraph Signal in the Photoluminescence Intensity of a Single Quantum Dot. *Phys. Rev. Lett.* **78,** 1110–1113 (1997).

41. Weiss, A. & Haran, G. Time-Dependent Single-Molecule Raman Scattering as a Probe of Surface Dynamics. *J. Phys. Chem. B* **105,** 12348–12354 (2001).

42. Emory, S. R., Jensen, R. A., Wenda, T., Han, M. & Nie, S. Re-examining the origins of spectral blinking in single-molecule and single-nanoparticle SERS. *Faraday Discuss.* **132,** 249–259 (2006).

43. Futamata, M., Maruyama, Y. & Ishikawa, M. Adsorbed Sites of Individual Molecules on Ag Nanoparticles in Single Molecule SensitivitySurface-Enhanced Raman Scattering. *J. Phys. Chem. B* **108,** 13119–13127 (2004).

44. Futamata, M., Maruyama, Y. & Ishikawa, M. Metal nanostructures with single molecule sensitivity in surface enhanced Raman scattering. *Vibrational Spectroscopy* **35,** 121–129 (2004).

45. Haran, G. Single-Molecule Raman Spectroscopy: A Probe of Surface Dynamics and Plasmonic Fields. *Acc. Chem. Res.* **43,** 1135–1143 (2010).

46. Maher, R. C. *et al.* Physics of single molecule fluctuations in surface enhanced Raman spectroscopy active liquids. *The Journal of Chemical Physics* **121,** 8901–8910 (2004).

47. Dieringer, J. A., Lettan, R. B., Scheidt, K. A. & Van Duyne, R. P. A Frequency Domain Existence Proof of Single-Molecule Surface-Enhanced Raman Spectroscopy. *J. Am. Chem. Soc.* **129,** 16249–16256 (2007).

48. Sonntag, M. D. *et al.* Single-Molecule Tip-Enhanced Raman Spectroscopy. *J. Phys. Chem. C* **116,** 478–483 (2012).

49. Li, Y., Doak, P., Kronik, L., Neaton, J. B. & Natelson, D. Voltage tuning of vibrational mode energies in single-molecule junctions. *PNAS* **111,** 1282–1287 (2014).

50. Li, Y. *et al.* Interplay of Bias-Driven Charging and the Vibrational Stark Effect in Molecular Junctions. *Nano Lett.* **16,** 1104–1109 (2016).

51. Aviram, A. & Ratner, M. A. Molecular rectifiers. *Chemical Physics Letters* **29,** 277–283 (1974).

52. Reed, M. A., Zhou, C., Muller, C. J., Burgin, T. P. & Tour, J. M. Conductance of a Molecular Junction. *Science* **278,** 252–254 (1997).

53. Reichert, J. *et al.* Driving Current through Single Organic Molecules. *Phys. Rev. Lett.* **88,** 176804 (2002).

54. Huber, R. *et al.* Electrical Conductance of Conjugated Oligomers at the Single Molecule Level. *J. Am. Chem. Soc.* **130,** 1080–1084 (2008).

55. González, M. T. *et al.* Electrical Conductance of Molecular Junctions by a Robust Statistical Analysis. *Nano Lett.* **6,** 2238–2242 (2006).

56. Kergueris, C. *et al.* Electron transport through a metal-molecule-metal junction. *Phys. Rev. B* **59,** 12505–12513 (1999).

57. Wu, S. *et al.* Molecular junctions based on aromatic coupling. *Nat Nano* **3,** 569–574 (2008).

58. Dulić, D. *et al.* One-Way Optoelectronic Switching of Photochromic Molecules on Gold. *Phys. Rev. Lett.* **91,** 207402 (2003).

59. Djukic, D. & van Ruitenbeek, J. M. Shot Noise Measurements on a Single Molecule. *Nano Lett.* **6,** 789–793 (2006).

60. Lörtscher, E., Weber, H. B. & Riel, H. Statistical Approach to Investigating Transport through Single Molecules. *Phys. Rev. Lett.* **98,** 176807 (2007).

61. Tian, J.-H. *et al.* Study of Molecular Junctions with a Combined Surface-Enhanced Raman and Mechanically Controllable Break Junction Method. *J. Am. Chem. Soc.* **128,** 14748–14749 (2006).

62. Kano, S., Tada, T. & Majima, Y. Nanoparticle characterization based on STM and STS. *Chem. Soc. Rev.* **44,** 970–987 (2015).

63. Xu, Zhang, Li & Tao. Direct Conductance Measurement of Single DNA Molecules in Aqueous Solution. *Nano Lett.* **4,** 1105–1108 (2004).

64. Grüter, L., González, M. T., Huber, R., Calame, M. & Schönenberger, C. Electrical Conductance of Atomic Contacts in Liquid Environments. *Small* **1,** 1067–1070 (2005).

65. Kamenetska, M. *et al.* Formation and Evolution of Single-Molecule Junctions. *Phys. Rev. Lett.* **102,** 126803 (2009).
66. Tsutsui, M., Shoji, K., Taniguchi, M. & Kawai, T. Formation and Self-Breaking Mechanism of Stable Atom-Sized Junctions. *Nano Lett.* **8,** 345–349 (2008).
67. Crommie, M. F., Lutz, C. P. & Eigler, D. M. Imaging standing waves in a two-dimensional electron gas. *Nature* **363,** 524–527 (1993).
68. Jang, S.-Y., Reddy, P., Majumdar, A. & Segalman, R. A. Interpretation of Stochastic Events in Single Molecule Conductance Measurements. *Nano Lett.* **6,** 2362–2367 (2006).
69. Measurement of Single-Molecule Resistance by Repeated Formation of Molecular Junctions | Science. Available at: http://science.sciencemag.org/content/301/5637/1221. (Accessed: 6th May 2016)
70. Repp, J., Meyer, G., Stojković, S. M., Gourdon, A. & Joachim, C. Molecules on Insulating Films: Scanning-Tunneling Microscopy Imaging of Individual Molecular Orbitals. *Phys. Rev. Lett.* **94,** 26803 (2005).
71. Huisman, E. H. *et al.* Stabilizing Single Atom Contacts by Molecular Bridge Formation. *Nano Lett.* **8,** 3381–3385 (2008).
72. Song, H., Reed, M. A. & Lee, T. Single Molecule Electronic Devices. *Adv. Mater.* **23,** 1583–1608 (2011).
73. Park, H., Lim, A. K. L., Alivisatos, A. P., Park, J. & McEuen, P. L. Fabrication of metallic electrodes with nanometer separation by electromigration. *Applied Physics Letters* **75,** 301–303 (1999).

74. Galperin, M. & Nitzan, A. Molecular optoelectronics: the interaction of molecular conduction junctions with light. *Phys. Chem. Chem. Phys.* **14,** 9421–9438 (2012).
75. Aradhya, S. V. & Venkataraman, L. Single-molecule junctions beyond electronic transport. *Nat Nano* **8,** 399–410 (2013).
76. Park, H. *et al.* Nanomechanical oscillations in a single-C60 transistor. *Nature* **407,** 57–60 (2000).
77. Wiley: Charge and Energy Transfer Dynamics in Molecular Systems, 3rd, Revised and Enlarged Edition - Volkhard May, Oliver Kuhn. Available at: http://www.wiley.com/WileyCDA/WileyTitle/productCd-3527407324.html. (Accessed: 27th May 2016)
78. Natelson, D. Towards the ultimate transistor. *Phys. World* **22,** 27 (2009).
79. Ratner, M. A. Bridge-assisted electron transfer: effective electronic coupling. *J. Phys. Chem.* **94,** 4877–4883 (1990).
80. Lörtscher, E., Ciszek, J. W., Tour, J. & Riel, H. Reversible and Controllable Switching of a Single-Molecule Junction. *Small* **2,** 973–977 (2006).
81. Li, X. *et al.* Conductance of Single Alkanedithiols: Conduction Mechanism and Effect of Molecule−Electrode Contacts. *J. Am. Chem. Soc.* **128,** 2135–2141 (2006).
82. Wold, D. J. & Frisbie, C. D. Formation of Metal−Molecule−Metal Tunnel Junctions: Microcontacts to Alkanethiol Monolayers with a Conducting AFM Tip. *J. Am. Chem. Soc.* **122,** 2970–2971 (2000).
83. Reed, M. A. Inelastic electron tunneling spectroscopy. *Materials Today* **11,** 46–50 (2008).

84. Galperin, M., Ratner, M. A. & Nitzan, A. Inelastic electron tunneling spectroscopy in molecular junctions: Peaks and dips. *The Journal of Chemical Physics* **121,** 11965–11979 (2004).
85. Galperin, M., Nitzan, A., Ratner, M. A. & Stewart, D. R. Molecular Transport Junctions: Asymmetry in Inelastic Tunneling Processes†. *J. Phys. Chem. B* **109,** 8519–8522 (2005).
86. Park, J. *et al.* Coulomb blockade and the Kondo effect in single-atom transistors. *Nature* **417,** 722–725 (2002).
87. Liang, W., Shores, M. P., Bockrath, M., Long, J. R. & Park, H. Kondo resonance in a single-molecule transistor. *Nature* **417,** 725–729 (2002).
88. Yu, L. H. *et al.* Kondo Resonances and Anomalous Gate Dependence in the Electrical Conductivity of Single-Molecule Transistors. *Phys. Rev. Lett.* **95,** 256803 (2005).
89. Kubatkin, S. *et al.* Single-electron transistor of a single organic molecule with access to several redox states. *Nature* **425,** 698–701 (2003).
90. Venkataraman, L. *et al.* Single-Molecule Circuits with Well-Defined Molecular Conductance. *Nano Lett.* **6,** 458–462 (2006).
91. Natelson, D., Yu, L. H., Ciszek, J. W., Keane, Z. K. & Tour, J. M. Single-molecule transistors: Electron transfer in the solid state. *Chemical Physics* **324,** 267–275 (2006).
92. Yu, L. H. & Natelson, D. The Kondo Effect in C60 Single-Molecule Transistors. *Nano Lett.* **4,** 79–83 (2004).
93. Pasupathy, A. N. *et al.* The Kondo Effect in the Presence of Ferromagnetism. *Science* **306,** 86–89 (2004).

94. Fursina, A., Lee, S., Sofin, R. G. S., Shvets, I. V. & Natelson, D. Nanogaps with very large aspect ratios for electrical measurements. *Applied Physics Letters* **92,** 113102 (2008).

95. Liang, W., Shores, M. P., Bockrath, M., Long, J. R. & Park, H. Kondo resonance in a single-molecule transistor. *Nature* **417,** 725–729 (2002).

96. Yu, L. H. *et al.* Inelastic Electron Tunneling via Molecular Vibrations in Single-Molecule Transistors. *Phys. Rev. Lett.* **93,** 266802 (2004).

97. Pasupathy, A. N. *et al.* Vibration-Assisted Electron Tunneling in C140 Transistors. *Nano Lett.* **5,** 203–207 (2005).

98. Song, H. *et al.* Observation of molecular orbital gating. *Nature* **462,** 1039–1043 (2009).

99. Ward, D. R., Corley, D. A., Tour, J. M. & Natelson, D. Vibrational and electronic heating in nanoscale junctions. *Nat Nano* **6,** 33–38 (2011).

100. Tian, J.-H. *et al.* Study of Molecular Junctions with a Combined Surface-Enhanced Raman and Mechanically Controllable Break Junction Method. *J. Am. Chem. Soc.* **128,** 14748–14749 (2006).

101. Yoo, W. S., Harima, H. & Yoshimoto, M. Polarized Raman Signals from Si Wafers: Dependence of In-Plane Incident Orientation of Probing Light. *ECS J. Solid State Sci. Technol.* **4,** P356–P363 (2015).

102. Herzog, J. B. *et al.* Dark Plasmons in Hot Spot Generation and Polarization in Interelectrode Nanoscale Junctions. *Nano Lett.* **13,** 1359–1364 (2013).

103. Abel, H.-B. & Fischer, F. The Continuous Background of SERS from Ag Colloids in Alkali Halide Crystals. *phys. stat. sol. (b)* **167,** 741–751 (1991).

104. Mahajan, S. *et al.* Understanding the Surface-Enhanced Raman Spectroscopy ‘Background’. *J. Phys. Chem. C* **114,** 7242–7250 (2010).
105. Otto, A., Akemann, W. & Pucci, A. Normal Bands in Surface-Enhanced Raman Scattering (SERS) and Their Relation to the Electron-Hole Pair Excitation Background in SERS. *Isr. J. Chem.* **46,** 307–315 (2006).
106. Peng, J. *et al.* Asymmetric least squares for multiple spectra baseline correction. *Analytica Chimica Acta* **683,** 63–68 (2010).
107. Natelson, D., Li, Y. & Herzog, J. B. Nanogap structures: combining enhanced Raman spectroscopy and electronic transport. *Phys. Chem. Chem. Phys.* **15,** 5262–5275 (2013).
108. Nitzan, A. *Chemical Dynamics in Condensed Phases: Relaxation, Transfer and Reactions in Condensed Molecular Systems*. (OUP Oxford, 2006).
109. Visualizing and controlling vibrational wave packets of single molecules : Nature : Nature Publishing Group. Available at: http://www.nature.com/nature/journal/v465/n7300/full/nature09110.html. (Accessed: 16th May 2016)
110. Evans, C. L. & Xie, X. S. Coherent Anti-Stokes Raman Scattering Microscopy: Chemical Imaging for Biology and Medicine. *Annual Review of Analytical Chemistry* **1,** 883–909 (2008).
111. Hochstrasser, R. M. Two-dimensional spectroscopy at infrared and optical frequencies. *PNAS* **104,** 14190–14196 (2007).
112. Zheng, J. *et al.* Ultrafast Dynamics of Solute-Solvent Complexation Observed at Thermal Equilibrium in Real Time. *Science* **309,** 1338–1343 (2005).

113. Aradhya, S. V. & Venkataraman, L. Single-molecule junctions beyond electronic transport. *Nat Nano* **8,** 399–410 (2013).
114. Song, H., Reed, M. A. & Lee, T. Single Molecule Electronic Devices. *Adv. Mater.* **23,** 1583–1608 (2011).
115. Djukic, D. *et al.* Stretching dependence of the vibration modes of a single-molecule $\mathrm{Pt}-{\mathrm{H}}_{2}-\mathrm{Pt}$ bridge. *Phys. Rev. B* **71,** 161402 (2005).
116. Arroyo, C. R. *et al.* Characterization of single-molecule pentanedithiol junctions by inelastic electron tunneling spectroscopy and first-principles calculations. *Phys. Rev. B* **81,** 75405 (2010).
117. Kiguchi, M. *et al.* Highly Conductive Molecular Junctions Based on Direct Binding of Benzene to Platinum Electrodes. *Phys. Rev. Lett.* **101,** 46801 (2008).
118. Boxer, S. G. Stark Realities. *J. Phys. Chem. B* **113,** 2972–2983 (2009).
119. Lambert, D. K. Vibrational Stark effect of CO on Ni(100), and CO in the aqueous double layer: Experiment, theory, and models. *The Journal of Chemical Physics* **89,** 3847–3860 (1988).
120. Oklejas, V., Sjostrom, C. & Harris, J. M. Surface-Enhanced Raman Scattering Based Vibrational Stark Effect as a Spatial Probe of Interfacial Electric Fields in the Diffuse Double Layer. *J. Phys. Chem. B* **107,** 7788–7794 (2003).
121. Suydam, I. T., Snow, C. D., Pande, V. S. & Boxer, S. G. Electric Fields at the Active Site of an Enzyme: Direct Comparison of Experiment with Theory. *Science* **313,** 200–204 (2006).

122. Hu, W. & Webb, L. J. Direct Measurement of the Membrane Dipole Field in Bicelles Using Vibrational Stark Effect Spectroscopy. *J. Phys. Chem. Lett.* **2,** 1925–1930 (2011).
123. Schkolnik, G. *et al.* Mapping local electric fields in proteins at biomimetic interfaces. *Chem. Commun.* **48,** 70–72 (2011).
124. Kneipp, K. *et al.* Single Molecule Detection Using Surface-Enhanced Raman Scattering (SERS). *Phys. Rev. Lett.* **78,** 1667–1670 (1997).
125. Nie, S. & Emory, S. R. Probing Single Molecules and Single Nanoparticles by Surface-Enhanced Raman Scattering. *Science* **275,** 1102–1106 (1997).
126. Ioffe, Z. *et al.* Detection of heating in current-carrying molecular junctions by Raman scattering. *Nat Nano* **3,** 727–732 (2008).
127. Konishi, T. *et al.* Single Molecule Dynamics at a Mechanically Controllable Break Junction in Solution at Room Temperature. *J. Am. Chem. Soc.* **135,** 1009–1014 (2013).
128. Liu, Z. *et al.* Revealing the molecular structure of single-molecule junctions in different conductance states by fishing-mode tip-enhanced Raman spectroscopy. *Nat Commun* **2,** 305 (2011).
129. Natelson, D., Li, Y. & Herzog, J. B. Nanogap structures: combining enhanced Raman spectroscopy and electronic transport. *Phys. Chem. Chem. Phys.* **15,** 5262–5275 (2013).
130. Ward, D. R., Corley, D. A., Tour, J. M. & Natelson, D. Vibrational and electronic heating in nanoscale junctions. *Nat Nano* **6,** 33–38 (2011).
131. Ward, D. R. *et al.* Electromigrated Nanoscale Gaps for Surface-Enhanced Raman Spectroscopy. *Nano Lett.* **7,** 1396–1400 (2007).

132. Ward, D. R. *et al.* Simultaneous Measurements of Electronic Conduction and Raman Response in Molecular Junctions. *Nano Lett.* **8,** 919–924 (2008).

133. Emory, S. R., Jensen, R. A., Wenda, T., Han, M. & Nie, S. Re-examining the origins of spectral blinking in single-molecule and single-nanoparticle SERS. *Faraday Discuss.* **132,** 249–259 (2006).

134. Darancet, P., Widawsky, J. R., Choi, H. J., Venkataraman, L. & Neaton, J. B. Quantitative Current–Voltage Characteristics in Molecular Junctions from First Principles. *Nano Lett.* **12,** 6250–6254 (2012).

135. Park, H., Lim, A. K. L., Alivisatos, A. P., Park, J. & McEuen, P. L. Fabrication of metallic electrodes with nanometer separation by electromigration. *Applied Physics Letters* **75,** 301–303 (1999).

136. Lu, X., Grobis, M., Khoo, K. H., Louie, S. G. & Crommie, M. F. Spatially Mapping the Spectral Density of a Single ${\mathrm{C}}_{\mathrm{60}}$ Molecule. *Phys. Rev. Lett.* **90,** 96802 (2003).

137. Yee, S. K., Malen, J. A., Majumdar, A. & Segalman, R. A. Thermoelectricity in Fullerene–Metal Heterojunctions. *Nano Lett.* **11,** 4089–4094 (2011).

138. Lörtscher, E. *et al.* Bonding and Electronic Transport Properties of Fullerene and Fullerene Derivatives in Break-Junction Geometries. *Small* **9,** 209–214 (2013).

139. Lund, P. A., Smardzewski, R. R. & Tevault, D. E. Surface-enhanced Raman spectra of benzene and benzene-d6 on vapor-deposited sodium. *Chemical Physics Letters* **89,** 508–510 (1982).

140. Sonntag, M. D., Chulhai, D., Seideman, T., Jensen, L. & Van Duyne, R. P. The Origin of Relative Intensity Fluctuations in Single-Molecule Tip-Enhanced Raman Spectroscopy. *J. Am. Chem. Soc.* **135,** 17187–17192 (2013).

141. Ward, D. R., Halas, N. J. & Natelson, D. Localized heating in nanoscale Pt constrictions measured using blackbody radiation emission. *Applied Physics Letters* **93,** 213108 (2008).

142. Mirjani, F., Thijssen, J. M. & Ratner, M. A. Probing Charge States in Molecular Junctions Using Raman Spectroscopy. *J. Phys. Chem. C* **116,** 23120–23129 (2012).

143. Perdew, J. P., Parr, R. G., Levy, M. & Balduz, J. L. Density-Functional Theory for Fractional Particle Number: Derivative Discontinuities of the Energy. *Phys. Rev. Lett.* **49,** 1691–1694 (1982).

144. Sau, J. D., Neaton, J. B., Choi, H. J., Louie, S. G. & Cohen, M. L. Electronic Energy Levels of Weakly Coupled Nanostructures: ${\mathrm{C}}_{60}$-Metal Interfaces. *Phys. Rev. Lett.* **101,** 26804 (2008).

145. Bilan, S., Zotti, L. A., Pauly, F. & Cuevas, J. C. Theoretical study of the charge transport through C${}_{60}$-based single-molecule junctions. *Phys. Rev. B* **85,** 205403 (2012).

146. Ramanantoanina, H., Gruden-Pavlovic, M., Zlatar, M. & Daul, C. Density functional theory study of the multimode Jahn-Teller problem in the fullerene anion. *Int. J. Quantum Chem.* **113,** 802–807 (2013).

147. Alqannas, H. S., Lakin, A. J., Farrow, J. A. & Dunn, J. L. Interplay between Coulomb and Jahn-Teller effects in icosahedral systems with triplet electronic states coupled to h-type vibrations. *Phys. Rev. B* **88,** 165430 (2013).

148. Laflamme Janssen, J., Côté, M., Louie, S. G. & Cohen, M. L. Electron-phonon coupling in ${\text{C}}_{60}$ using hybrid functionals. *Phys. Rev. B* **81,** 73106 (2010).
149. Varma, C. M., Zaanen, J. & Raghavachari, K. Superconductivity in the Fullerenes. *Science* **254,** 989–992 (1991).
150. Haddon, R. C., Brus, L. E. & Raghavachari, K. Electronic structure and bonding in icosahedral C60. *Chemical Physics Letters* **125,** 459–464 (1986).
151. Lu, X., Grobis, M., Khoo, K. H., Louie, S. G. & Crommie, M. F. Charge transfer and screening in individual ${\mathrm{C}}_{60}$ molecules on metal substrates: A scanning tunneling spectroscopy and theoretical study. *Phys. Rev. B* **70,** 115418 (2004).
152. Available at: http://www.langtoninfo.co.uk/web_content/9780521896344_frontmatter.pdf. (Accessed: 16th May 2016)
153. Kaasbjerg, K., Novotný, T. & Nitzan, A. Charge-carrier-induced frequency renormalization, damping, and heating of vibrational modes in nanoscale junctions. *Phys. Rev. B* **88,** 201405 (2013).
154. Park, E. S., Andrews, S. S., Hu, R. B. & Boxer, S. G. Vibrational Stark Spectroscopy in Proteins: A Probe and Calibration for Electrostatic Fields. *J. Phys. Chem. B* **103,** 9813–9817 (1999).
155. Suydam, I. T., Snow, C. D., Pande, V. S. & Boxer, S. G. Electric Fields at the Active Site of an Enzyme: Direct Comparison of Experiment with Theory. *Science* **313,** 200–204 (2006).

156. Hu, W. & Webb, L. J. Direct Measurement of the Membrane Dipole Field in Bicelles Using Vibrational Stark Effect Spectroscopy. *J. Phys. Chem. Lett.* **2,** 1925–1930 (2011).
157. Schkolnik, G. *et al.* Mapping local electric fields in proteins at biomimetic interfaces. *Chem. Commun.* **48,** 70–72 (2011).
158. Lambert, D. K. Vibrational Stark effect of CO on Ni(100), and CO in the aqueous double layer: Experiment, theory, and models. *The Journal of Chemical Physics* **89,** 3847–3860 (1988).
159. Oklejas, V., Sjostrom, C. & Harris, J. M. SERS Detection of the Vibrational Stark Effect from Nitrile-Terminated SAMs to Probe Electric Fields in the Diffuse Double-Layer. *J. Am. Chem. Soc.* **124,** 2408–2409 (2002).
160. Bublitz, G. U. & Boxer, S. G. STARK SPECTROSCOPY: Applications in Chemistry, Biology, and Materials Science. *Annual Review of Physical Chemistry* **48,** 213–242 (1997).
161. Chattopadhyay, A. & Boxer, S. G. Vibrational Stark Effect Spectroscopy. *J. Am. Chem. Soc.* **117,** 1449–1450 (1995).
162. Kneipp, K. *et al.* Single Molecule Detection Using Surface-Enhanced Raman Scattering (SERS). *Phys. Rev. Lett.* **78,** 1667–1670 (1997).
163. Ward, D. R. *et al.* Simultaneous Measurements of Electronic Conduction and Raman Response in Molecular Junctions. *Nano Lett.* **8,** 919–924 (2008).
164. Emory, S. R., Jensen, R. A., Wenda, T., Han, M. & Nie, S. Re-examining the origins of spectral blinking in single-molecule and single-nanoparticle SERS. *Faraday Discuss.* **132,** 249-259-319 (2006).

165. Zou, S. & Weaver, M. J. Potential-Dependent Metal–Adsorbate Stretching Frequencies for Carbon Monoxide on Transition-Metal Electrodes: Chemical Bonding versus Electrostatic Field Effects. *J. Phys. Chem.* **100,** 4237–4242 (1996).

166. Kwasnieski, D. T., Wang, H. & Schultz, Z. D. Alkyl-nitrile adlayers as probes of plasmonically induced electric fields. *Chem. Sci.* **6,** 4484–4494 (2015).

167. McEntee, M., Stevanovic, A., Tang, W., Neurock, M. & Yates, J. T. Electric Field Changes on Au Nanoparticles on Semiconductor Supports – The Molecular Voltmeter and Other Methods to Observe Adsorbate-Induced Charge-Transfer Effects in Au/TiO2 Nanocatalysts. *J. Am. Chem. Soc.* **137,** 1972–1982 (2015).

168. Marr, J. M. & Schultz, Z. D. Imaging Electric Fields in SERS and TERS Using the Vibrational Stark Effect. *J. Phys. Chem. Lett.* **4,** 3268–3272 (2013).

169. Banik, M. *et al.* Surface-Enhanced Raman Trajectories on a Nano-Dumbbell: Transition from Field to Charge Transfer Plasmons as the Spheres Fuse. *ACS Nano* **6,** 10343–10354 (2012).

170. Ward, D. R., Scott, G. D., Keane, Z. K., Halas, N. J. & Natelson, D. Electronic and optical properties of electromigrated molecular junctions. *J. Phys.: Condens. Matter* **20,** 374118 (2008).

171. Yoo, S. H., Kum, J. M. & Cho, S. O. Tuning the electronic band structure of PCBM by electron irradiation. *Nanoscale Research Letters* **6,** 545 (2011).

172. Stavytska-Barba, M., Salvador, M., Kulkarni, A., Ginger, D. S. & Kelley, A. M. Plasmonic Enhancement of Raman Scattering from the Organic Solar Cell Material P3HT/PCBM by Triangular Silver Nanoprisms. *J. Phys. Chem. C* **115,** 20788–20794 (2011).

173. Park, H. *et al.* Nanomechanical oscillations in a single-C60 transistor. *Nature* **407,** 57–60 (2000).
174. Ward, D. R. *et al.* Simultaneous Measurements of Electronic Conduction and Raman Response in Molecular Junctions. *Nano Lett.* **8,** 919–924 (2008).
175. Ward, D. R., Hüser, F., Pauly, F., Cuevas, J. C. & Natelson, D. Optical rectification and field enhancement in a plasmonic nanogap. *Nat Nano* **5,** 732–736 (2010).
176. Bilan, S., Zotti, L. A., Pauly, F. & Cuevas, J. C. Theoretical study of the charge transport through C${}_{60}$-based single-molecule junctions. *Phys. Rev. B* **85,** 205403 (2012).
177. Lu, X., Grobis, M., Khoo, K. H., Louie, S. G. & Crommie, M. F. Charge transfer and screening in individual C60 molecules on metal substrates: A scanning tunneling spectroscopy and theoretical study. *Phys. Rev. B* **70,** 115418 (2004).
178. Larson, B. W. *et al.* Electron Affinity of Phenyl–C61–Butyric Acid Methyl Ester (PCBM). *J. Phys. Chem. C* **117,** 14958–14964 (2013).
179. Tlahuice-Flores, A. & Mejía-Rosales, S. Structural and Vibrational Study of PCBM. *J. Chem. Chem. Eng.* **5,** 1034–1040 (2011).
180. Janssen, R. A. J., Hummelen, J. C. & Wudl, F. Photochemical Fulleroid to Methanofullerene Conversion via the Di-.pi.-methane (Zimmerman) Rearrangement. *J. Am. Chem. Soc.* **117,** 544–545 (1995).
181. Barbour, L. W., Hegadorn, M. & Asbury, J. B. Microscopic Inhomogeneity and Ultrafast Orientational Motion in an Organic Photovoltaic Bulk Heterojunction Thin Film Studied with 2D IR Vibrational Spectroscopy. *J. Phys. Chem. B* **110,** 24281–24286 (2006).

182. Bishop, D. M. The vibrational Stark effect. *The Journal of Chemical Physics* **98,** 3179–3184 (1993).

183. Zayak, A. T. *et al.* Chemical Raman Enhancement of Organic Adsorbates on Metal Surfaces. *Phys. Rev. Lett.* **106,** 83003 (2011).

184. Zhang, R. *et al.* Chemical mapping of a single molecule by plasmon-enhanced Raman scattering. *Nature* **498,** 82–86 (2013).

185. Liu, Z. *et al.* Revealing the molecular structure of single-molecule junctions in different conductance states by fishing-mode tip-enhanced Raman spectroscopy. *Nat Commun* **2,** 305 (2011).

186. Seelenbinder, J. A., Brown, C. W. & Urish, D. W. Self-Assembled Monolayers of Thiophenol on Gold as a Novel Substrate for Surface-Enhanced Infrared Absorption. *Appl. Spectrosc., AS* **54,** 366–370 (2000).

187. Roseler, A. & Korte, E.-H. Infrared-Optical Characterization of Metallic Island Films rapid communications. *Appl. Spectrosc., AS* **51,** 902–904 (1997).

188. Adato, R. *et al.* Ultra-sensitive vibrational spectroscopy of protein monolayers with plasmonic nanoantenna arrays. *PNAS* **106,** 19227–19232 (2009).

189. Aizpurua, J. *et al.* Optical properties of coupled metallic nanorods for field-enhanced spectroscopy. *Phys. Rev. B* **71,** 235420 (2005).

190. Jain, P. K., Eustis, S. & El-Sayed, M. A. Plasmon Coupling in Nanorod Assemblies: Optical Absorption, Discrete Dipole Approximation Simulation, and Exciton-Coupling Model. *J. Phys. Chem. B* **110,** 18243–18253 (2006).

191. Brown, L. V. *et al.* Surface-Enhanced Infrared Absorption Using Individual Cross Antennas Tailored to Chemical Moieties. *J. Am. Chem. Soc.* **135,** 3688–3695 (2013).

192. Cubukcu, E., Zhang, S., Park, Y.-S., Bartal, G. & Zhang, X. Split ring resonator sensors for infrared detection of single molecular monolayers. *Applied Physics Letters* **95,** 43113 (2009).

193. Chen, X., Ciracì, C., Smith, D. R. & Oh, S.-H. Nanogap-Enhanced Infrared Spectroscopy with Template-Stripped Wafer-Scale Arrays of Buried Plasmonic Cavities. *Nano Lett.* **15,** 107–113 (2015).

194. Huck, C. *et al.* Plasmonic Enhancement of Infrared Vibrational Signals: Nanoslits versus Nanorods. *ACS Photonics* **2,** 1489–1497 (2015).

195. Han, G. *et al.* Infrared spectroscopic and electron microscopic characterization of gold nanogap structure fabricated by focused ion beam. *Nanotechnology* **22,** 275202 (2011).

196. Huck, C. *et al.* Surface-Enhanced Infrared Spectroscopy Using Nanometer-Sized Gaps. *ACS Nano* **8,** 4908–4914 (2014).

197. Giannini, V., Francescato, Y., Amrania, H., Phillips, C. C. & Maier, S. A. Fano Resonances in Nanoscale Plasmonic Systems: A Parameter-Free Modeling Approach. *Nano Lett.* **11,** 2835–2840 (2011).

198. Wu, C. *et al.* Fano-resonant asymmetric metamaterials for ultrasensitive spectroscopy and identification of molecular monolayers. *Nat Mater* **11,** 69–75 (2012).

199. Neubrech, F. *et al.* Resonances of individual metal nanowires in the infrared. *Applied Physics Letters* **89,** 253104 (2006).

200. Neubrech, F. *et al.* Resonant Plasmonic and Vibrational Coupling in a Tailored Nanoantenna for Infrared Detection. *Phys. Rev. Lett.* **101,** 157403 (2008).
201. Luk'yanchuk, B. *et al.* The Fano resonance in plasmonic nanostructures and metamaterials. *Nat Mater* **9,** 707–715 (2010).
202. Coker, D. F., Reimers, J. R. & Watts, R. O. The infrared absorption spectrum of water. *Australian Journal of Physics* **35,** 623–638 (1982).
203. Galperin, M. & Nitzan, A. Raman Scattering and Electronic Heating in Molecular Conduction Junctions. *J. Phys. Chem. Lett.* **2,** 2110–2113 (2011).